QUANTIFICATION, SPATIAL PROFILING, AND MATHEMATICAL MODELING OF PATHOLOGY DISTRIBUTIONS IN THE HUMAN RETINA

by

James Frederick Tucker

A dissertation submitted to the faculty of
The University of Utah
in partial fulfillment of the requirements for the degree of

Doctor of Philosophy

Interdepartmental Program in Neuroscience

The University of Utah

August 2012

The University of Utah Graduate School

STATEMENT OF DISSERTATION APPROVAL

The dissertation of **James Frederick Tucker**

has been approved by the following supervisory committee members:

Robert E. Marc	, Chair	**5/29/2012** Date Approved
Wolfgang Baehr	, Member	**5/29/2012** Date Approved
Mary T. Lucero	, Member	**6/11/2012** Date Approved
Bryan W. Jones	, Member	**5/29/2012** Date Approved
M. E. Hartnett	, Member	**5/29/2012** Date Approved

and by **Kristen Keefe**, Chair of the Department of **Interdepartmental Program in Neuroscience**

and by Charles A. Wight, Dean of The Graduate School.

ABSTRACT

Many retinal pathologies, including age-related macular degeneration (AMD), display characteristic spatial patterns. AMD predominately affects the macula, the central cone-dominated region of the human retina responsible for high-acuity daytime vision. An understanding of why the macula is specifically susceptible to age-related changes would likely prove invaluable to understanding the pathology of AMD and the development of preventative therapies. Unfortunately, such an understanding has thus far proven elusive. A large number of physiological and anatomical parameters vary significantly between the central and peripheral human retina, and many of these parameters are altered during retinal degenerative disorders. This produces a large number of spatial associations between various parameters, obscuring causal relationships and making identification of timing and initiating factors very challenging. To address this challenge we developed RetSpace, an analytic software package designed to generate and analyze quantitative maps of anatomic and pathologic parameters within individual human retinas. The RetSpace system was specifically designed to analyze image sets generated with computational molecular phenotyping (CMP), a technique pioneered by our laboratory to characterize the immense cellular diversity of the neural and sensory retina. By combining the sensitivity and diversity of CMP with the analytic power of RetSpace, we have produced a novel mechanism to study the spatial distributions and regional variability of various measures of retinal anatomy and pathology, as well as the extent to which different pathologies show regional correlations potentially indicative of shared pathological origins. To demonstrate the utility of our approach we have analyzed the severity and spatial distributions of an extensive set of anatomic and pathologic parameters in a series of aging human donor retinas. In doing so we have identified novel metabolic changes in the RPE and photoreceptors that are spatially and quantitatively correlated with known pathological characteristics of AMD and may serve as sensitive markers of early stress in AMD and other retinal diseases. Mathematical models of the heterocellular diversity of these metabolic changes provide further insight into the mechanisms behind these changes and hint at the origins and spatial specificity of the disease.

CONTENTS

LIST OF FIGURES

CHAPTER 1

INTRODUCTION

Age-related macular degeneration (AMD) is one of the leading causes of blindness worldwide and the number one cause of blindness in elderly populations in developed countries. However, while much is known about the genetics, risk factors, and pathological consequences of AMD, the initiation and progression of the disease are still not well understood, and there remains no effective prevention or treatment for the vast majority of patients. In particular, the macular specificity of the disease remains somewhat of a mystery (Zarbin, 2004; de Jong, 2006).

A great deal has been learned recently about the genetic and environmental risk factors associated with AMD, many of which appear to act through the gradual accumulation of oxidative and immune-mediated damage to the retinal pigmented epithelium (RPE), a highly specialized cellular layer upon which photoreceptor function and survival are critically dependent (Anderson et al., 2010; Hageman et al., 2005; Klein et al., 2005; Edwards et al., 2005). While experimental models of some of these risk factors have generated pathologies similar to limited aspects of AMD, others have not, and at this time there remains no model that recapitulates the initial pathogenesis or explains the macular specificity of the disease. The difficulty in developing such a model is likely due in large part to the fact that AMD is a disease that only occurs after several decades of progressive, poorly-understood, multifactorial aging changes and environmental exposures (Zarbin, 2004; de Jong, 2006). Modeling AMD in an animal is further complicated by the fact that it is a disease of the macula, an anatomical structure fairly unique to the retinas of higher primates (Provis et al., 2005). The absence of a model of the pathogenesis and regional specificity of the disease underscores the importance of developing methods to extract such information from human tissue.

Many retinal pathologies, including AMD, display characteristic spatial patterns. AMD predominately affects the macula, the central cone-dominated region of the human retina responsible for high-acuity daytime vision. An understanding of why the macula is specifi-

cally susceptible to age-related changes would likely prove invaluable to understanding the pathology of AMD and the development of preventative therapies. Unfortunately, such an understanding has thus far proven elusive. A large number of physiological and anatomical parameters vary significantly between the central and peripheral human retina, and many of these parameters are altered during retinal degenerative disorders (Provis et al., 2005). This produces a large number of spatial associations between various parameters, obscuring causal relationships and making identification of timing and initiating factors very challenging.

To address this challenge we developed RetSpace, an analytic software package designed to generate and analyze quantitative, spatially-congruent maps of multiple anatomic and pathologic parameters within individual human retinas. The RetSpace system was specifically designed to analyze image sets generated with computational molecular phenotyping (CMP), a technique pioneered by our laboratory to characterize the immense cellular diversity of the neural and sensory retina. By combining the sensitivity and diversity of CMP with the analytic power of RetSpace, we have produced a novel mechanism to study the spatial distributions and regional variability of various measures of retinal anatomy and pathology, as well as the extent to which different pathologies show regional correlations potentially indicative of shared pathological origins. Furthermore, because the measured parameters are quantified in serial ultrathin sections traversing the same individual cells, the data sets generated allow analysis of not only regional patterns but also of interparametric correlations at the single-cell level. The data sets generated are thus rich with information about the diversity of individual cellular characteristics and responses to disease that can be extracted through statistical analysis and mathematical modeling.

To demonstrate the utility of our approach we have characterized and analyzed the severity and spatial distributions of an extensive set of anatomic and pathologic parameters in a series of aging human donor retinas. In doing so we have identified novel metabolic changes in the RPE and photoreceptors that are spatially and quantitatively correlated with known pathological characteristics of AMD and may serve as sensitive markers of early stress in AMD and other retinal diseases. Mathematical models of the heterocellular diversity of these metabolic changes provide further insight into the mechanisms behind these changes and hint at the origins and spatial specificity of the disease. Similarities between our findings in human tissue and findings in animal models have also provided

important confirmation of the relevance of these models in the study of AMD. By providing the details of our histological techniques and all analytical software free to the research community, we hope to facilitate the development and adoption of a common method for the characterization and analysis of retinal diseases, animal models, and therapeutic interventions.

CHAPTER 2

THE RETSPACE SOFTWARE SYSTEM

2.1 Introduction

2.1.1 Retinal Geography

The retina in higher primates is characterized by significant central-to-peripheral differences in anatomy and physiology. These differences are most pronounced in the central region known as the macula, where retinal anatomy varies substantially from that of the surrounding retina in terms of both the type and connectivity of retinal neurons, as well as the structure and function of the associated supporting tissues (Wässle and Boycott, 1991; Provis et al., 2005). While this regional specialization confers to primates a high degree of spatial resolution and visual acuity, these anatomic differences also render the central retina susceptible to different types of degenerative disorders than the periphery. As a result, human retinal diseases often differentially affect central and peripheral vision, with the spatial distributions of pathology depending upon the mechanism of disease and its relationship to specific anatomic and physiologic characteristics of the retina. The ability to examine and describe regional patterns of retinal anatomy and pathology has thus proven very important in the study of retinal diseases. Likewise, discoveries of disease mechanisms can in turn inform understanding of underlying patterns of retinal anatomy and physiology. For example, dysfunction in the capacity of the retinal pigmented epithelium (RPE) to enzymatically recycle bleached retinoids from photoreceptor cells is more damaging to cones than to rods, indicating that the preservation of vision in the cone-dominated central retina is more dependent on the retinoid cycle than in the rod-dominated periphery (Zhang et al., 2008).

For retinal degenerations in which an etiology has yet to be identified, regional differences in the type and severity of pathology may hold important information to guide the discovery of disease mechanisms. Age-related macular degeneration (AMD) is the leading cause of new-onset blindness in the elderly in the developed world and is one of the best genetically characterized of human diseases, but the mechanism and characteristic spatial

distribution of AMD remain poorly understood (Anderson et al., 2010; Zarbin, 2004). While the regional distributions of a variety of age-related retinal pathologies have been characterized, the techniques available for such characterizations have thus far suffered from limitations that prevent detailed analysis of the complex spatial and combinatorial characteristics of age-related retinal disease.

Here we present a histopathological method and accompanying software system designed to allow the quantification and mathematical modeling of the spatial distributions of multiple overlapping anatomic and pathologic parameters within single retinas. We demonstrate the utility of this method by quantifying and modeling the spatial distributions of a variety of anatomic and pathological parameters in a series of aging human retinas.

2.1.2 Molecular Depth

The first major challenge in mapping multiple overlapping histological parameters is combining a sufficient number of histological signals into one data set. Most histological techniques are limited to examining small numbers of signals in any given tissue sample, limiting the number of parameters that can be examined and the depth of the combinatorial analysis that can be performed on the final data set. This is a major limitation when studying a highly multifactorial disease like AMD. In order to overcome this limitation, an investigator must either perform all desired characterizations on single sections or perform separate characterizations on serial sections and then register the resulting data sets. Single-section techniques are very limited in molecular diversity because traditional secondary amplifications irreversibly conflate the signals of any more than three to four probes at best. While not susceptible to signal conflation limitations, serial section techniques are instead limited by the investigators ability to accurately coregister the data sets produced from individual sections. Even under optimum theoretical conditions, serial-section techniques can only provide coregistration with a spatial resolution equivalent to the sectioning thickness, so in order to examine signal combinatorics at cellular and subcellular levels, it is necessary to section at submicron levels. Ultrathin sectioning carries limitations of its own, specifically the requirement to embed tissues in a hard medium like plastic and the inability to depth-integrate weak signals from sparse molecular targets such as those limited to membranes.

Computational molecular phenotyping (CMP) is a serial-section technique that overcomes many of these limitations and produces datasets with sufficient dimensionality to

observe the vast cellular diversity of the neural retina. By examining single molecular targets on individual serial sections, CMP overcomes the signal conflation limitations of fluorescent amplification methods and gains significant increases in dynamic range through the use of highly nonlinear silver amplification. By embedding tissues in Epon plastic, sectioning at 200nm, and using software to coregister image mosaics from serial sections, CMP is able to produce data sets that combine 12 or more individual molecular channels with spatial coregistration that is more than sufficient to perform combinatorial analysis at the single-cell level. By labeling concentrated cytosolic metabolites instead of sparse or membrane-bound targets, CMP is able to generate consistent, reliable signals without requiring an embedding medium through which probes can penetrate or sections thick enough to allow spatial signal integration. While CMP is very limited in the number of compatible molecular probes, it makes up for this lack of molecular diversity by providing far more complete anatomic and pathologic characterization than other histological techniques (Marc et al., 1995; Kalloniatis et al., 1996; Marc and Jones, 2002).

2.1.3 Scalability

The next major challenge in mapping multiple signals over large areas is scalability. Most histopathological methods are difficult to scale up to tissue areas large enough to capture a canonical regional sampling of an organ as large and regionally diverse as a human retina. We overcome this limitation by using light microscopes with automated stages, highly-refined computational mosaicing and image coregistration techniques, and customized data storage and annotation systems optimized for our unique image sets (Anderson et al., 2009).

The human eye has a horizontal circumference of $\sim 80mm$, with the retina covering $\sim 75\%$ of this length. To capture a broad sampling of retinal eccentricities traversing from the center (fovea) to the edge (ora serrata), a tissue sample must therefore contain at least $20mm$ of retina (Figure 2.1a). The human retina varies in thickness up to $\sim 0.5mm$ in the macula, so tissue sections must have dimensions on the order of $\sim 1mm\,x\,20mm$. Using a 40x oil lens and a $1388x1036$ pixel digital image sensor produces images with a spatial calibration factor of 5435 pixels/mm, leading to data channels on the order of $\sim 600 * 10^6\,pixels^2$. Using 8-bit signal encoding, this amounts to $4.8Gb$ or $0.6GB$ per channel, uncompressed. To examine 10 different histological signals in such a manner thus produces datasets on the order of $6GB$ per tissue donor before any correction channels or

annotation masks are created. With annotations and compression, average dataset sizes are $\sim 6GB$ in practice. This is far in excess of the allowable file sizes for most image formats, so data sets must be broken up and automatically mosaicked at the time of analysis.

The large size of the histological data sets required for a method of this type are thus dependent upon several layers of computational assistance in the capture and management of digital datasets. In addition to using computerized autotiling microscopes, the RetSpace software system includes features to assist in the storage, organization, and retrieval of image data through a simplified, customizable programmatic interface. Annotations are created and stored in Adobe Photoshop files and exported to a RetSpace-compatible file structure using a customized Javascript plugin. RetSpace then uses an automated import system to scan data directories and build an object structure that allows individual data channels to be easily accessed from within analysis scripts.

2.1.4 Quantification and Modeling

The final major challenge in creating a histological system capable of mapping signals over large areas and comparing signal profiles between individuals is generating reliable quantitative measures of complex histological properties. Quantifications of cellular and histological characteristics must be performed in as objective a manner as possible and must be very consistent and reproducible in order to allow comparison between areas or individuals. To ensure that histological signals are comparable between individuals, all histological processing is done in large batches with several levels of controls. Signals are carefully scrutinized and either corrected or replaced if signal inconsistencies are detected. The RetSpace system also contains image signal correction methods to allow analysis and correction for background noise which can vary between tissue samples and would otherwise introduce a significant inconsistency between datasets. Corrected image sets are then analyzed to produce quantitative profiles of histological properties using a core set of RetSpace modules operating on user-supplied annotation masks. To ensure that quantifications are as consistent and objective as possible, quantitation routines are designed to require only very simple user annotations of obvious structures such as nuclei, blood vessels, and major histological boundaries. User annotations can be easily audited for accuracy and updated if errors are detected.

2.2 Methods

2.2.1 Computational Molecular Phenotyping

The data sets used to develop the system described in this report were generated using computational molecular phenotyping (CMP). CMP is an established imaging technology using clustering analysis on quantitative immunohistochemical image sets to classify cells and other tissue features in situ. The fundamental techniques of CMP have been well described (Marc et al., 1995, Marc and Jones, 2002), but a summary of each step will be presented here, including specializations of the process added to facilitate large-scale spatial analysis.

2.2.2 Tissue Harvest and Fixation

All human eyes were obtained through the Utah Lions Eye Bank within $\sim$ 3 hours of death. The Lions Eye Bank donor procurement and distribution procedure complies with the Declaration of Helsinki, and all patient information gathered was deidentified in accordance with HIPPA privacy rules. Eyes were enucleated and flushed with fixative using two hypodermic needles placed into opposite sides of the posterior chamber. The eyes were then opened to expose the posterior chamber and immersion fixed at 4°C before tissue processing. Fixative used was 2.5% glutaraldehyde and 1% formaldehyde in 0.1 M phosphate buffer (pH 7.4) with 3% sucrose and 1mM MgSO4 to preserve ultrastructure (Figure 2.1a).

2.2.3 Bloc Preparation

Prior to dissection, fundus photographs were taken using a Canon EOS 1D Mark III mounted to an Olympus SZ61 stereo microscope. Eyes were then opened with 4 relief cuts and a $\sim 5mm$-wide full-thickness strip was dissected out, starting at the optic nerve head and traversing horizontally through the macula and out to the temporal ora serrata. Dissected strips were then dehydrated in a series of graded methanols and acetones, then infiltrated with Eponate resin and cured retina side-down onto glass slides. The thick connective tissue of the sclera was shaved off using razor blades, leaving behind the retina and the underlying vascular choroid. The tissue strips were then measured, marked, and cut into 8 segments, each approximately 3mm wide. The segments were then assembled into two stacks of four segments each using cyanoacrylate, then the stacks were embedded into Eponate blocs for sectioning (Figure 2.1b).

2.2.4 Sectioning and Immunohistochemistry

Blocs were sectioned at 200nm on a Leica Ultracut UCT ultramicrotome and serial sections were placed onto 12-spot slides. Detailed sectioning records were kept regarding section quality, thickness variations, knife changes, and other sectioning disruptions to allow selection of uninterrupted sets of high-quality serial sections for further processing. Selected slides were then deplasticized in sodium ethoxide as previously described (Marc et al., 1978). Sections were then probed with primary IgGs targeting 4-aminobutyrate (GABA, γ), L-arginine (R), L-aspartate (D), L-glutamate (E), L-glutamine (Q), glutathione (J), glycine (G), and taurine (τ). All small molecule IgGs (except anti-R) were obtained from Signature Immunologics, Inc. (Salt Lake City, UT). Anti-R was developed by the Marc laboratory (Marc et al., 1995). Rod opsin was probed with Rho 1D4 (a gift of Dr. Robert Molday of the University of British Columbia) and cone opsin was probed with anti-LWS1 opsin (red/green opsin) from Millipore Corp. (product number AB-5405; Temecula, CA). The use and dilutions of most of these IgGs have been previously described (Marc et al., 2007) and our protocols are detailed at the MarcLab website. Anti-CRALBP was a gift from Dr. Jack Saari of the University of Washington and was used at 1:1000 from serum. Primary IgGs were visualized either via silver-intensification of 1.4 nm gold granules conjugated to goat antirabbit or goat antimouse secondary IgGs, or with Cy-3-conjugated secondaries (Jackson ImmunoResearch, West Grove, PA). All sections were also stained with 4',6-diamidino-2-phenylindole (DAPI, Molecular Probes, Eugene, OR). Following immunolabeling, slides were hermetically sealed under glass coverslips using LR White resin (Ted Pella, Redding, CA) (Figure 2.1c).

2.2.5 Scanning and Image Registration

Images were captured as 8-bit, 1388x1036 pixel frames under voltage-regulated tungsten halogen flux with a Peltier-cooled camera (Fast 1394 Qicam; QImaging, Burnaby, BC, Canada) and autotiled with a montaging system (Syncroscan; Synoptics Inc., Frederick, MD) and an automated stage (Märzhäuser Wetzlar GmbH, Wetzlar, Germany) (Marc et al., 2007). Images were acquired at nominal resolutions of 5435 pixels/mm and 2717 pixels/mm with 40x oil and 20x air objectives, respectively. Tiling and registration were performed with IR-tweak, a multiplatform registration application based on a Thin Plate Spline transform. More information about IR-tweak and other related image processing applications can be found at the Koshevoy lab, University of Utah (Figure 2.1d).

2.2.6 Programming Languages and Libraries

All software was written in Python 2.7 on Apple and Windows workstations. Image import, manipulation, and output was handled using the Python Imaging Library v.1.1.7. Various mathematical and scientific tools were utilized from Numeric Python (NumPy) and Scientific Python (SciPy). Figures were generated using the Matplotlib graphing library for Python and LaTeX for mathematics and text rendering. Videos were compiled from computed images using the mEncoder and ffMpeg rendering engines.

2.2.7 Image Signal Correction

Image pixel levels are exposure-corrected to remove background signal and remap useful signal information to occupy the full 8-bit grayscale range. Black points are calculated as median pixel values within user-supplied masks of nontissue background areas. White points are calculated by analyzing image histograms and determining cutoff pixel values that correspond to user-specified clipping tolerances (i.e. 0.01% total pixel area). A linear transformation is then applied to the image that maps the black and white points to grayscale values of 0 and 255, respectively. This transformation preserves all but the very small amount of signal information discarded by the user-specified clipping tolerance, and also maintains the shape of the function relating pixel values to probe target concentrations. A report is saved showing the histogram changes and the transformation applied.

2.2.8 Horizontal Spatial Calibration

In order to compare parametric profiles between individuals with slightly different globe sizes, horizontal image space must be calibrated to a common canonical model eye. The temporal ora serrata corresponds to the edge of the nasal visual field, which is associated with a visual arc length of $\sim 60^\circ$ from the fovea at 0°. To facilitate this conversion, RetSpace contains a module that allows users to create a transformation object for each dataset based upon recorded pixel coordinates of the fovea and the ora serrata. Horizontal pixel coordinate are then converted into degrees in visual space by the following transformation:

$$Visual^\circ(x) = (x - x_f) * \frac{60^\circ}{x_{os} - x_f} \tag{2.1}$$

where x is an arbitrary horizontal pixel coordinate, x_f is the approximate horizontal pixel coordinate of the fovea, and x_{os} is the approximate horizontal pixel coordinate of the

ora serrata. All calculations are kept in image coordinate space until results are being visualized, at which point the transformation to visual space is applied.

2.2.9 Image Segmentation

Several types of analysis used in the RetSpace system rely on the Segmentation module to identify the pixels associated with individual objects within user-supplied masks. Masks of structures of interest can be generated manually or extracted from theme maps produced during image clustering. For example, manual masking of the choriocapillaris vessels allows investigators to learn about the sizes and distributions of capillaries within different retinal areas. Similarly, masks of individual classes from clustering analysis can be used to examine regional changes in the molecular makeup, size, shape, and vertical positions of the corresponding cell types. So-called dot masks can be quickly generated by hand to take a small sampling of any histological object the user desires to analyze rapidly.

The RetSpace Segmentation module implements a simple flood-filling routine that is designed to identify nonblack objects on a black background. The segmentation object contains a list of segment objects, each of which denotes a contiguous set of nonzero pixels found in the mask. Flood-filling is performed using a 4-direction continuity requirement, meaning that diagonally-connected pixels are not considered continuous. A user-specified minimum segment size allows users to prevent unwanted spatial noise from registering as small segments. Upon generation, segmentation objects are cached in association with the mask image for future use, along with an image in which each segment is assigned a random RGB color to allow users to audit the segmentation process and verify object identification and separation. The segmentation object contains methods to allow users to retrieve and plot complete horizontal profiles of any of the calculated geometric or positional characteristics of its segments, including their areas, widths, heights, and x and y positions.

Segmentation evaluation objects are created by applying a segmentation object to a data image. For each segment, data image values corresponding to segment pixels are statistically analyzed, and the segmentation evaluation object stores the mean, median, max, min, and standard deviation of the data pixel values. The segmentation evaluation object also contains methods to allow users to retrieve and plot complete horizontal profiles of the signal strength of any measured immunological probe in any segmented object type.

2.2.10 Vertical Spatial Stratification

Retinal physiology depends on vertical stratification at both the cellular and subcellular levels, and retinal pathologies often manifest with architectural disruptions at one or both levels. The primary information channel of the retina is a vertical glutamatergic cascade that is dependent upon stratification of cell types into sublamina that are disrupted in many forms of retinal degeneration (Jones and Marc, 2005). Several retinal cell types also require vertical polarizations in protein distributions that can be disrupted in retinal disease (Zhang et al., 2008). In order to quantify retinal pathologies, it is thus of great interest to be able to express the vertical location of a histological element with respect to a particular physiological sublamina. At a computational level, this requires a mapping between vertical image coordinate space and a relative vertical position within a given sublamina. As the retina and its sublamina vary in thickness with retinal eccentricity, this mapping must be performed independently at each horizontal image location.

The RetSpace Stratification module allows users to define the positions of histological lamina, analyze the spatial locations of histological objects and signals relative to those lamina, and visualize the results. The module consists of two main object types: the Stratification object and the Stratification evaluation object. A Stratification object defines the laminar areas and their names, and is created by analyzing a user-supplied mask denoting the boundaries between individual lamina. Each masked boundary is pinched from the top and bottom until the median vertical location is identified for each horizontal pixel value. Each boundary is then stored as an array of vertical position values associated with a user-supplied name for future recall. The Stratification object provides a display method to allow users to visualize the results of the mask analysis for proof reading purposes. Stratification Evaluation objects are created by applying a Stratification object to a data image. The user supplies a Stratification object, the names of the boundaries to be used, and a set of objects or pixels in image space to be stratified. For each horizontal coordinate, a linear transformation is calculated mapping vertical pixel coordinates to a retinal laminar space in which 0 corresponds to the lower specified boundary, 1 corresponds to the upper specified boundary, and intermediate values correspond to fractional positions between the two. Using these transformations, the user can then stratify any positional data set desired. The positions of separable objects like cells can be stratified to examine horizontal trends in the laminar localization of a particular cell class. Alternatively, a nonseparable histological data set can be thresholded, stratified, and displayed using a

user-specified laminar color encoding (Figure 2.2a). Stratifications of nonseparable data sets are further visualized by laminar histograms, which can be plotted simultaneously (Figure 2.2b) or stacked to provide the viewer with simultaneous perception of both the position of the lamina and the number of data points localized to it (Figure 2.2d). Finally, laminar histograms can be normalized for regional variations in the total number of data points, making the heights of each curve indicative only of the degree of laminar localization at that horizontal position, independent of confounding changes in the density of the original signal (Figure 2.2 c,e).

2.2.11 Object Density and Coverage Calculations

The RetSpace Coverage and Density modules are used to map one-dimensional (1-D) population densities and coverage factors of spatially separable objects, such as cells or blood vessels. A 1-D horizontal coverage factor at position x is calculated by counting the number of horizontal pixel values occupied by objects within a summation region of specified size centered around position x, then dividing by the horizontal width of the summation region. A 1-D numerical density factor at position x is calculated by counting the number of objects within a summation region of specified size centered around position x, then dividing by the horizontal width of the summation region. A 1-D area density factor at position x is calculated by counting the cumulative area of objects within a summation region of specified size centered around position x, then dividing by the horizontal width of the summation region. A horizontal trend of coverage factors, numerical densities, or area densities is assembled by sliding the summation region along the horizontal extent of the image, adjusting the leading and trailing edges as needed to accommodate the boundaries of the image. This process must, however, be informed of the positions and sizes of any gaps in the relevant tissue structures, or else gaps in the tissue would be treated the same as intact regions of tissue that were merely devoid of the class of objects being counted. The Retspace Density and Coverage modules accommodate this adjustment by accepting user-supplied masks of gap regions and adjusting the size of the summation regions to ignore regions defined as gaps (Figure 2.3).

One of the principle purposes of the Coverage and Density modules is to quantify important characteristics in the choriocapillaris. The density and coverage calculations described here are comparable with established metrics used in previous studies to quantify age-related changes in the choriocapillaris, allowing direct comparison of our data to the

results of these larger, more focused cross-sectional studies. For the purposes of this report, the term 'choriocapillaris coverage' will refer to the density factors calculated by the Density module from user-supplied masks of terminal choriocapillaries. This measurement can be thought of as the relative fraction of retinal area occupied by vessels within the choriocapillaris layer. A region devoid of capillaries has a coverage factor of zero, while a region with continuous horizontal coverage of capillaries has a coverage factor of one. This measurement does not take into account the depth or cross-sectional area of the capillaries, only their horizontal width in vertical sections, and is thus comparable to measurements made in flat-mounted retinas in previous studies (McLeod et al., 2002; McLeod et al., 2009).

The term choriocapillaris density will refer to the area density factors calculated by the Density module from user-supplied masks of terminal choriocapillaries. This measurement can be thought of as the total cross-sectional area of vessels present in a given linear distance of retina. In regions devoid of capillaries, the choriocapillaris density factor is again zero. In regions containing capillaries, the choriocapillaris density factor is a positive number that reflects either the number or the size of the capillaries. The choriocapillaris density factor thus provides a more sensitive measure of perfusion capacity than the choriocapillaris coverage factor and is comparable to measurements made in vertical sections in previous studies (Ramrattan et al., 1994). It should be noted, however, that this measurement does not account for potential differences in upstream choroidal vessels, so it should not be considered a measure of perfusion but merely of the capacity of the choriocapillaris to support perfusion. An atrophy of the capillary bed at this level would most certainly imply impaired perfusion, but the absence of atrophy at the capillary level does not imply intact perfusion, as obstructions could still exist upstream in the larger choroidal feeder vessels.

(a) Tissue Harvest & Fixation

1. Inject fixative and enucleate
2. Open anterior chamber, store in fixative @4°C

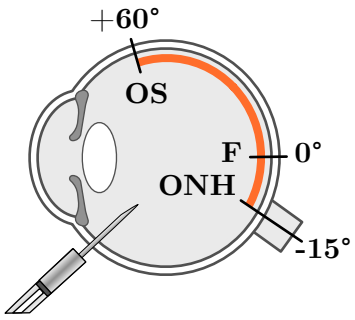

3. Dissect strip from optic nerve head (ONH) through fovea (F) to temporal ora serrata (OS)

(b) Bloc Preparation

1. Dehydrate, infiltrate, and flat mount retinal strip
2. Cut into segments

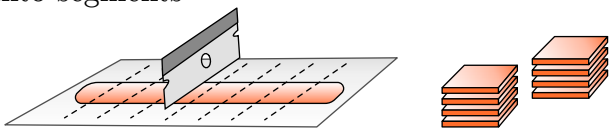

4. Assemble stacks
5. Embed stacks in plastic blocs

(c) Sectioning & Immunohistochemistry

1. Serial section blocs @ 200nm
2. Perform immunohistochemistry

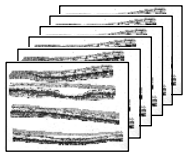

5. Scan sections and refine mosaics
6. Coregister images and reassemble strips

Figure 2.1: Graphical flowchart of tissue processing and data preparation workflow.

Figure 2.2: Example of image stratification analysis. (a) Sample image to be analyzed. White dotted lines indicate the stratum boundaries. Colored pixels indicate the signal to be analyzed. Color indicates the fractional vertical distance of the object between the two boundaries at that horizontal location. (b) Raw pixel counts for each stratification layer. (c) Pixel counts for each stratification layer normalized to the total number of pixels analyzed at that horizontal location. At the far left, the red and orange layers each contain $\sim 30\%$ of the pixels, while the other seven layers each contain $< 10\%$ At the far right, pixels become evenly distributed with each of the 10 layers containing $\sim 10\%$ of the pixels. The sum of all curves is equal to 1 at all horizontal locations. (d) Normalized curve values in a stacked plot. The height of each layer indicates the normalized fraction of pixels contained in that layer at that horizontal location.

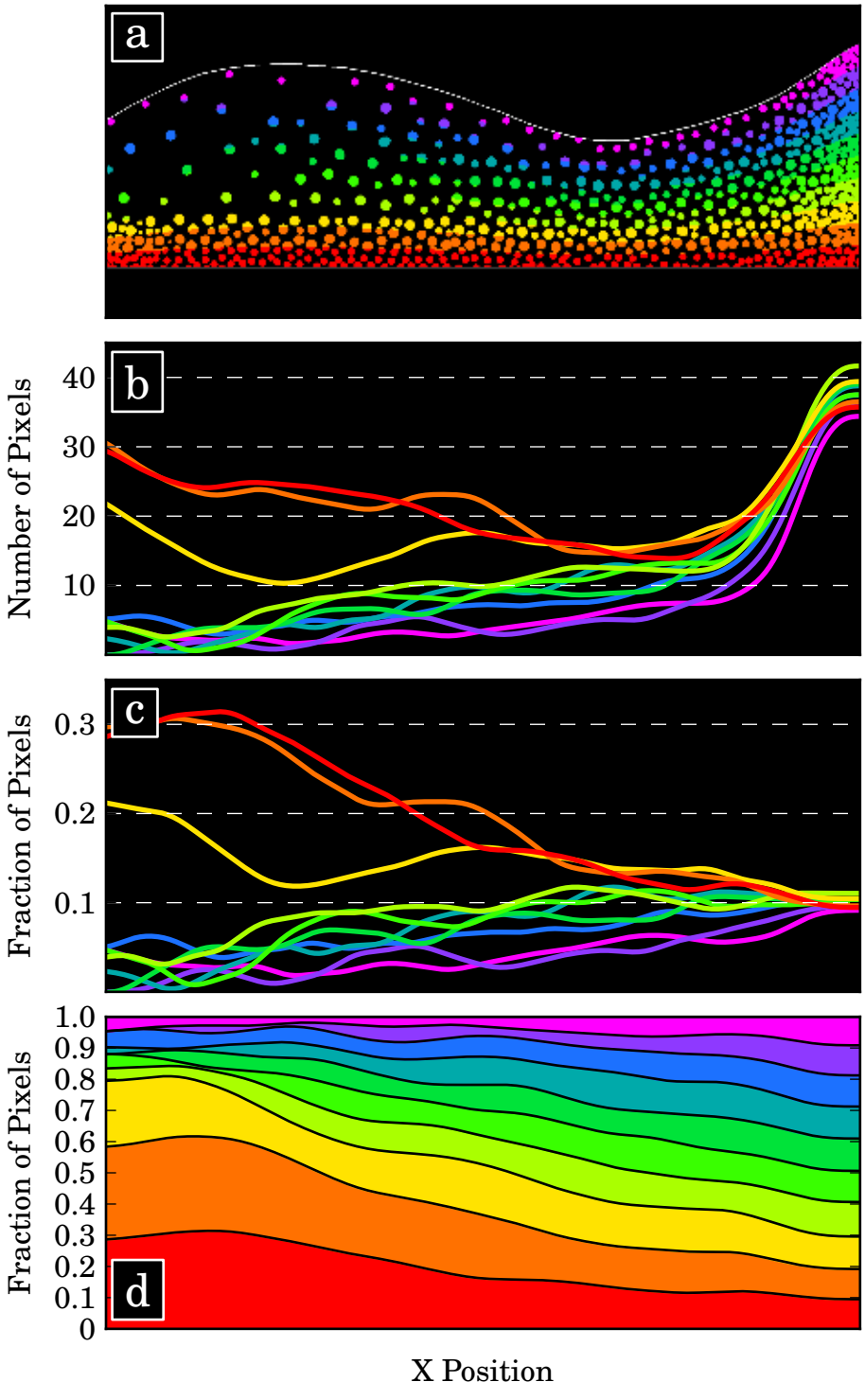
a
b
Number of Pixels
40
30
20
10
c
Fraction of Pixels
0.3
0.2
0.1
d
Fraction of Pixels
1.0
0.9
0.8
0.7
0.6
0.5
0.4
0.3
0.2
0.1
0
X Position

Figure 2.3: Example of spatial coverage and density calculations. (a) Sample image to be analyzed. Red, green, and blue objects are analyzed separately in subsequent calculations. (b) Coverage factor calculations. Red and green objects have the same width and thus cover the same fraction of horizontal space. Blue objects are narrower and thus cover a smaller fraction of horizontal space. (c) Numerical density calculations. The same number of each type of object are present at each position, so numerical density values are equivalent for the three objects. (d) Green objects have greater area than red and blue objects.

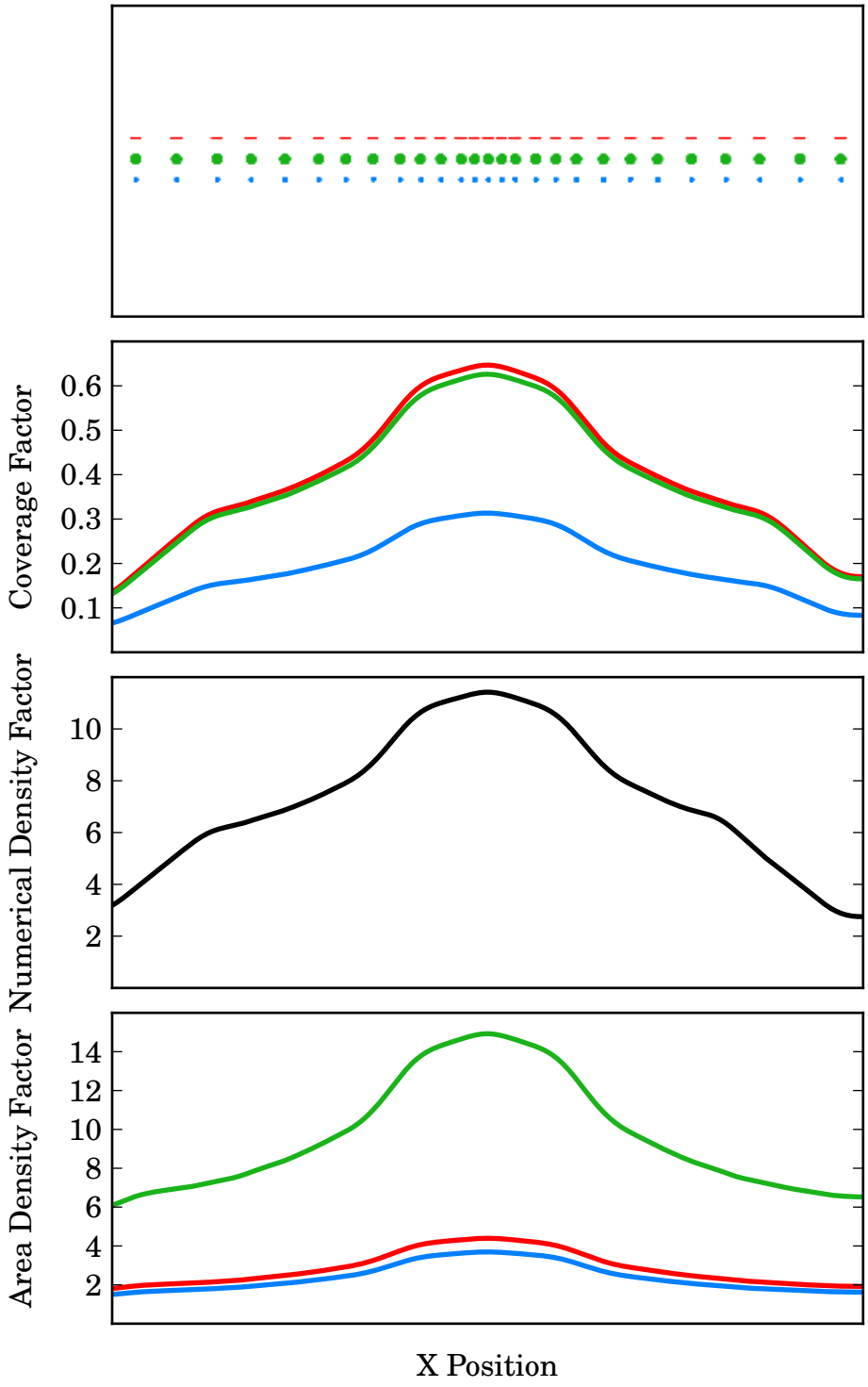
Coverage Factor
0.6
0.5
0.4
0.3
0.2
0.1
Numerical Density Factor
10
8
6
4
2
Area Density Factor
14
12
10
8
6
4
2
X Position

CHAPTER 3

MATHEMATICAL MODELING OF CELL POPULATIONS

3.1 Introduction

The mathematical model described here allows a collection of cells to be modeled as a weighted combination of overlapping subpopulations by analyzing the concentrations of specific molecules within each cell. The need for such a model arose in attempting to identify and characterize cells in histological sections of human retina based upon intracellular concentrations of various small molecules. In the course of this work we discovered populations of cells with molecular concentration distributions too continuous to be meaningfully separated by clustering but insufficiently uniform to be described as single populations. To analyze these populations we developed a method of fitting distributions of measurements to weighted combinations of probability distribution functions while constraining functional parameters to biologically relevant ranges.

Probability distribution functions are frequently combined using convolution, but this method generates a combined probability distribution function in which each of the original probability distribution functions is equally weighted, making this method unsuitable for modeling populations made up of uneven combinations of subpopulations. Instead, we required a system in which the individual subpopulations could make differential contributions to the total population, requiring the combined probability distribution function to be constructed using a weighted linear combination of individual probability distribution functions. We also required the ability to constrain the parameters of each individual subpopulation to biologically realistic values and the ability to implement interparametric constraints on characteristics, such as the spacing between distinct subpopulations. Finally, we required the ability to access the fitting routine within the programming language in which data sets would be generated. Commercially available fitting routines satisfied some but not all of our requirements, so we implemented our modeling routine in the Python programming language using the NumPy and SciPy libraries, allowing us to take advantage

of established constrained optimization routines (Kraft, 1997).

Using our system, data distributions can be fit to weighted combinations of overlapping Gaussian probability distribution functions. The parameters of each individual subpopulation can be constrained to biologically relevant ranges, and the spacing between subpopulation means can be limited to a minimum distance. Of particular importance is the ability to constrain the variance of subpopulations based upon experimentally verified systems, allowing the known intrinsic variability of a cellular parameter to inform the construction of a biologically appropriate model. Models containing varying numbers of subpopulations can be compared to allow users to select an appropriate degree of subclassification for each combined population. The potential accuracy of models can be examined for theoretical populations, allowing users to predict the size and nature of the data sets required to reliably resolve given subpopulations. The stability of the modeling system in the face of measurement error can be examined by superimposing artificial noise of a specified magnitude on real or theoretical data and analyzing model outcome variability. All code is documented and available for free public download.

3.2 Methods

3.2.1 Model

Let $p(x)$ denote a Gaussian probability distribution function for a measured variable x, where m is the mean expected value of x and v is the variance of x:

$$p(x) = \frac{1}{v\sqrt{2\pi}}\, e^{\frac{-(x-m)^2}{2v^2}} \tag{3.1}$$

This function describes the probability of each possible outcome value of x for a single measurement. The expected cumulative distribution $P(x)$ for a series of such measurements is simply $p(x)$ scaled for the number of measurements h:

$$P(x) = h * p(x) = \frac{h}{v\sqrt{2\pi}}\, e^{\frac{-(x-m)^2}{2v^2}} \tag{3.2}$$

Now consider a diverse population of entities $\{a\}$ consisting of a series of component sets $\{a_i\}$ each with cardinality h_i:

$$\{a\} = \bigcup_{i=0}^{n} \{a_i\} \quad ; \quad |a_i| = h_i \tag{3.3}$$

where each component set $\{a_i\}$ is a subset of a unique parent population $\{A_i\}$ with a characteristic probability distribution function $p_i(x)$ for the measured variable x:

$$\{a_i\} \subset \{Ai\} \quad ; \quad p_i(x) = \frac{1}{v\sqrt{2\pi}}\, e^{\frac{-(x-m_i)^2}{2v_i^2}} \tag{3.4}$$

The expected cumulative distribution $P(x)$ for measurements of x on the entire set {a} is a combination of the probability distribution functions of the original component populations $\{A_i\}$ scaled by the cardinality h_i of their individual contributions to {a}:

$$P(x) = \sum_{i=1}^{n} h_i\, p_i(x) \tag{3.5}$$

Normalizing $P(x)$ yields a probability distribution function $\bar{P}(x)$ that describes the outcome probabilities for a single measurement of x for a single entity in $\{a\}$ (Figure 3.1):

$$\bar{P}(x) = \frac{1}{h_{tot}} \sum_{i=1}^{n} h_i\, p_i(x) \quad ; \quad h_{tot} = \sum_{i=1}^{n} h_n \tag{3.6}$$

3.2.2 Optimization

Now consider the reverse problem in which an investigator starts with a distribution of measurements $D(x)$ and a known number of measurements h_{tot}. In order to approximate the component sets that make up the diverse population $\{a\}$ and the probability distribution functions $p_i(x)$ of the unique parent populations $\{A_i\}$, the parameters of a model probability distribution function $\bar{P}(x)$ can be optimized to fit a normalized version of the data distribution $\bar{D}(x)$. The least squares method used to perform this optimization is based upon minimization of a residual function R representing the sum of the squares of the difference between the normalized data set $\bar{D}(x)$ and the probability distribution function $\bar{P}(x)$ being used to model it:

$$R = \sum_{i=1}^{n} (\bar{D}(x_i) - \bar{P}(x_i, t))^2 \tag{3.7}$$

where t represents an arbitrary modifiable parameter of $\bar{P}(x)$. Minimization of R is achieved by starting with an initial guess for the parameters of $\bar{P}(x)$ and sequentially manipulating these parameters until a local minimum value of R is achieved. The method generally used to calculate the sequential parametric modifications is called the method of

steepest descent, in which a parameter t is sequentially shifted Δt in a direction opposite to the gradient of R with respect to t:

$$\Delta t \quad \propto \quad -\frac{\partial R}{\partial t} \tag{3.8}$$

This requires that the partial derivatives of R be known with respect to each modifiable parameter t. These partial derivatives can be expressed in terms of the partial derivative of $\bar{P}(x)$ with respect to the parameter t:

$$\frac{\partial R}{\partial t} = 2 * \sum_{i=1}^{n} (\bar{D}(x_i) - \bar{P}(x_i, t)) * \frac{\partial \bar{P}}{\partial t} \tag{3.9}$$

The partial derivative of the model probability distribution function $\bar{P}$ with respect to each scaling coefficient h_i is simply the characteristic probability distribution function p_i by which the scaling coefficient is multiplied:

$$\begin{aligned} \bar{P} &= \frac{1}{h_{tot}} \sum_{i=1}^{n} h_i * p_i \\ \frac{\partial \bar{P}}{\partial h_i} &= \frac{p_i}{h_{tot}} \end{aligned} \tag{3.10}$$

The partial derivatives of $\bar{P}$ with respect to the individual gaussian parameters m_i and v_i can be expressed in terms of the partial derivatives of the individual characteristic probability distribution functions:

$$\frac{\partial \bar{P}}{\partial m_i} = \frac{h_i}{h_{tot}} * \frac{\partial (p_i)}{\partial m_i} = \frac{h_i (x - m_i)}{h_{tot}\, v_i^2} * p_i \tag{3.11}$$

$$\frac{\partial \bar{P}}{\partial v_i} = \frac{h_i}{h_{tot}} * \frac{\partial (p_i)}{\partial v_i} = \frac{h_i (x - m_i)^2}{h_{tot}\, v_i^3} * p_i \tag{3.12}$$

The complete set of final equations for fitting a normalized data distribution $\bar{D}(x)$ to a probability distribution function $\bar{P}(x)$ is as follows:

$$p_i(x) = \frac{1}{v_i\sqrt{2\pi}}\, e^{\frac{-(x-m_i)^2}{2v_i^2}}$$

$$\bar{P} = \frac{1}{h_{tot}} \sum_{i=1}^{n} h_i * p_i(x, m_i, v_i) \quad ; \quad h_{tot} = \sum_{i=1}^{n} h_n$$

$$R = \sum_{i=1}^{n} (\bar{D}(x_i) - \bar{P}(x_i, t))^2$$

$$\frac{\partial R}{\partial h_i} = 2 * \sum_{i=1}^{n} (\bar{D}(x_i) - \bar{P}(x_i, t)) * \frac{1}{h_{tot}} * p_i(x, m_i, v_i)$$

$$\frac{\partial R}{\partial m_i} = 2 * \sum_{i=1}^{n} (\bar{D}(x_i) - \bar{P}(x_i, t)) * \frac{h_i(x - m_i)}{h_{tot}\, v_i^2} * p_i(x, m_i, v_i)$$

$$\frac{\partial R}{\partial v_i} = 2 * \sum_{i=1}^{n} (\bar{D}(x_i) - \bar{P}(x_i, t)) * \frac{h_i(x - m_i)^2}{h_{tot}\, v_i^3} * p_i(x, m_i, v_i)$$

3.2.3 Parametric Constraint

It is of great importance to place limits on subpopulation amplitudes and variances to prevent the addition of subpopulations that merely adjust the residual instead of adding distinct, biologically-realistic subpopulations to the model. Without such constraints, residuals can be continually decreased through the endless addition of small, narrow subpopulations, leading to limitless model complexity and a complete lack of biological realism or relevance. By preventing the addition of such subpopulations, parametric constraints provide a much-needed functional limit to model complexity.

Variance constraints can be applied based upon measurable population distributions for a known parameter of a specific cell type (Marc and Jones, 2002). Spacing constraints, on the other hand, are not based upon biological reality but rather on practicality. Without spacing constraints, regions of a distribution curve that are well modeled as a single subpopulation can easily be split into two subpopulations with half the amplitude and a slight shift in means to make minor adjustments to the shape of the curve. Such a model may be entirely reasonable from a biological perspective; there is no reason two subpopulations might not have similar characteristics. The addition of such superimposed subpopulations is, however, useless from a classification perspective, as the two subpopulations in question would be indistinguishable from one another. By preventing the addition of such subpopulations, spacing constraints allow the user to produce models that are not only based in biological reality but also practically useful for classification purposes.

Parametric constraints are implemented by providing the fitting routine with a set of

constraint functions which are to be minimized alongside the residual. As with the residual function, the fitting routine requires not only the value of the constraint function for a given set of parameters but also the partial derivatives of the constraint function with regards to each parameter to assist in determining parametric modifications. For example, if the user wishes a variance v to be greater than some biologically realistic threshold value v_0, the constraint function $C(t)$ and partial derivative are as follows:

$$C(t) = v - v_0 \quad ; \quad \frac{\partial C}{\partial v} = 1 \tag{3.13}$$

Similarly, if the user wishes to require the distance between two peak means m_1 and m_2 to be limited to values greater than some arbitrary distance d, the constraint function $C(t)$ and partial derivatives (assuming $m_2 > m_1$) are as follows:

$$C(m_1, m_2) = |(m_2 - m_1)| - d \quad ; \quad \frac{\partial C}{\partial m_2} = 1 \quad ; \quad \frac{\partial C}{\partial m_1} = -1 \tag{3.14}$$

3.2.4 Initial Parametric Approximation

Steepest descent optimization requires an initial parameter guess in order to start the optimization process, then uses parametric gradients of the residual and constraint functions to lead to parametric combinations that minimize these functions. This process is dependent upon the parametric gradients pointing the optimization process towards global minima of the residual and constraint functions, and can thus be disrupted when the initial guess and the optimal solution are separated by an intervening local minimum in the residual or constraint functions. The optimization process also depends upon the parametric gradients of the residual and constraint functions pointing in the same direction so that the directions of parametric modifications are not ambiguous. These limitations become more problematic the more complex and constrained the optimization conditions are, and random initial guesses frequently fail to lead to successful optimizations. It is thus of great importance to start with an initial parameter combination that is reasonably similar to the optimized solution. Our solution to this problem is quite simple: the routine attempts multiple optimizations from a diverse series of initial guesses and settles on the solution that achieves the best minimization of the residual and constraint functions. While this approach is not very computationally efficient, it tends to produce reliable, repeatable results over a wide range of diverse data distributions.

To generate initial parameter guesses our modeling system first analyzes the nonzero regions of the data distribution to determine a center point x_c and a total spread x_s. Initial

peak means are evenly distributed within a region centered around x_c and of total width $x_s * \alpha_s$, where α_s is an arbitrary spacing factor. Initial peak widths are set to $x_s * \alpha_w$ where α_w is an arbitrary width factor. Initial peak heights are set to weight each peak evenly. A diverse collection of initial parameter guesses is assembled by cycling though lists of default spacing and width factors and creating initial parameter guesses based upon each combination. We find this approach to reliably produce at least one initial parameter guess that leads to a successful optimization regardless of the shape of the data distribution (Figure 3.2).

3.2.5 Selection of Model Complexity

Parametric constraints help limit model complexity, but the number of subpopulations to be included in a model of this nature is a somewhat ultimately a somewhat arbitrary decision that must be made by the user. To assist users in selecting a degree of model complexity that produces practical classification and separability, our system provides the means to compare fits of various complexity in terms of both their final residual values and the degrees of overlap between their subpopulations. To quantify overlap between two individual probability distribution functions $p_i(x)$ and $p_j(x)$, we calculate the Bhattacharyya distance $B_{i,j}$ as follows:

$$B_{i,j} = \int_{-\infty}^{\infty} \sqrt{p_i(x) * p_j(x)}\, dx \tag{3.15}$$

For a model composed of of n individual subpopulations, there will be

$$\binom{n}{2} = \frac{n!}{2(n-2)!} \tag{3.16}$$

different combinations of subpopulations for which to calculate Bhattacharyya distances. By comparing models of increasing complexity in terms of both residual values and degree of subpopulation overlap, users can select a model that provides an adequate match to the data set without adding unnecessary complexity (Figure 3.3).

3.2.6 Accuracy and Noise Stability Testing

Our modeling system gives users the ability to examine the expected accuracy and reliability of generated models for specific hypothetical probability distribution functions. Starting from a user-defined probability distribution function $\bar{P}(x)$, the system generates an artificial data set, performs a fit, and compares the resulting model to the probability distribution function specified by the user. Users can also examine the reliability of a

generated model in the face of experimental noise. Starting with a real data set and a specified noise level, the modeling system generates a series of noisy data sets by adding random noise to the real data set, then performs a fit on each noisy data set. The system then either generates a video of the fitting results or superimposes the results onto a single plot to allow visualization of the extent to which the generated model is sensitive to experimental noise (Fig. 3.4).

3.3 Conclusions

Using the modeling system described here, one-dimensional population diversity can be described and compared quantitatively. Models are generated and returned inside the highly-flexible Python programming language, allowing this modeling system to be used for a variety of data analysis applications. All figures in this manuscript were generated natively by our software using customized visualization functions based upon the Matplotlib plotting library for Python for automated vector-based plot generation and the LaTeX typesetting language for text rendering.

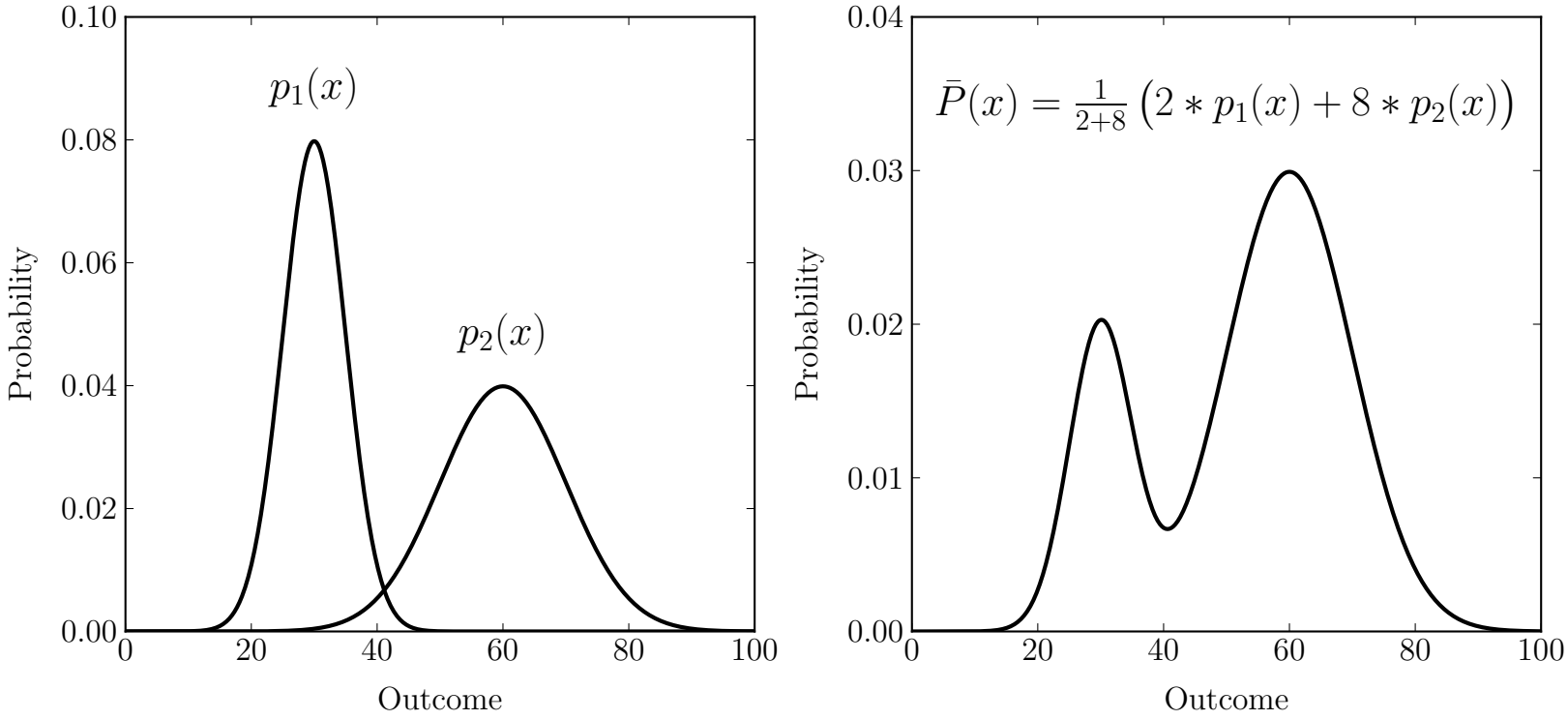

(a) Individual Probability Distribution Functions

(b) Cumulative Probability Distribution Function

Figure 3.1: *Sample model assembly.* **(a)** The distributions $p_1(x)$ and $p_2(x)$ represent the characteristic probability distribution functions for individual measurements of x within two distinct subpopulations $\{A_1\}$ and $\{A_2\}$, respectively. **(b)** Calculation of a cumulative probability distribution curve $\bar{P}(x)$ for a set of 10 measurements made from a combined population containing $(h_1 = 2)$ items from $\{A_1\}$ and $(h_2 = 8)$ items from $\{A_2\}$.

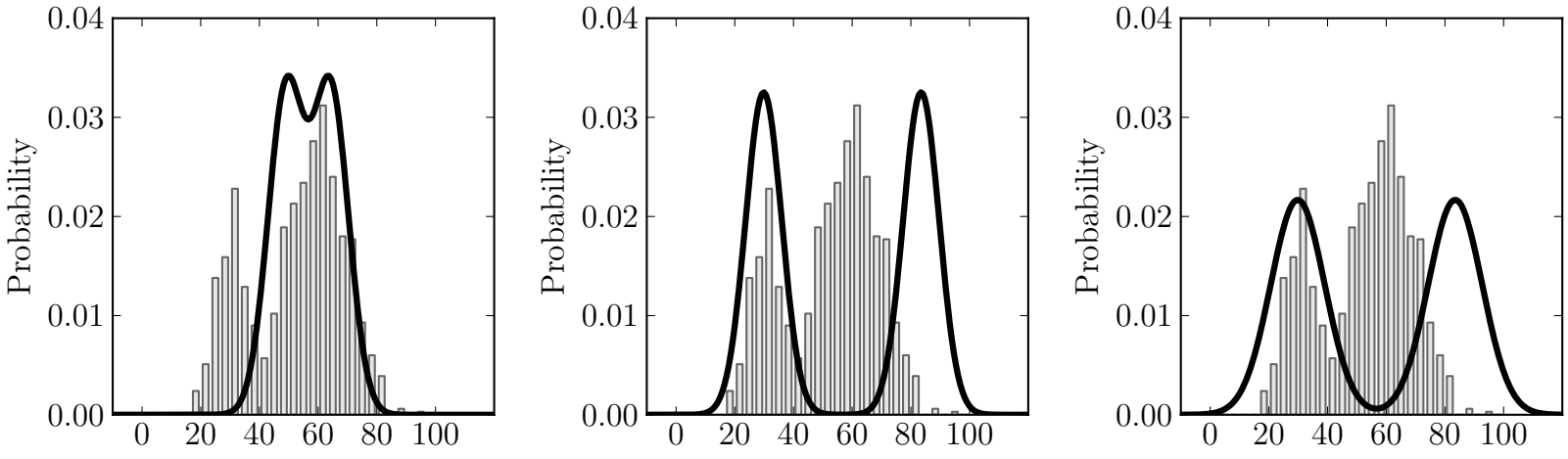

(a) $\alpha_s = 0.2, \quad \alpha_w = 0.08$ (b) $\alpha_s = 0.7, \quad \alpha_w = 0.08$ (c) $\alpha_s = 0.7, \quad \alpha_w = 0.12$

Figure 3.2: *Initial parametric approximation.* All examples are based upon a sample data set using the population described in Figure 1. By default, the system tries initial parameter sets using default spacing factors $\alpha_s = \{0.1, 0.5, 1.0\}$ and width factors $\alpha_w = \{0.05, 0.1, 0.5\}$.

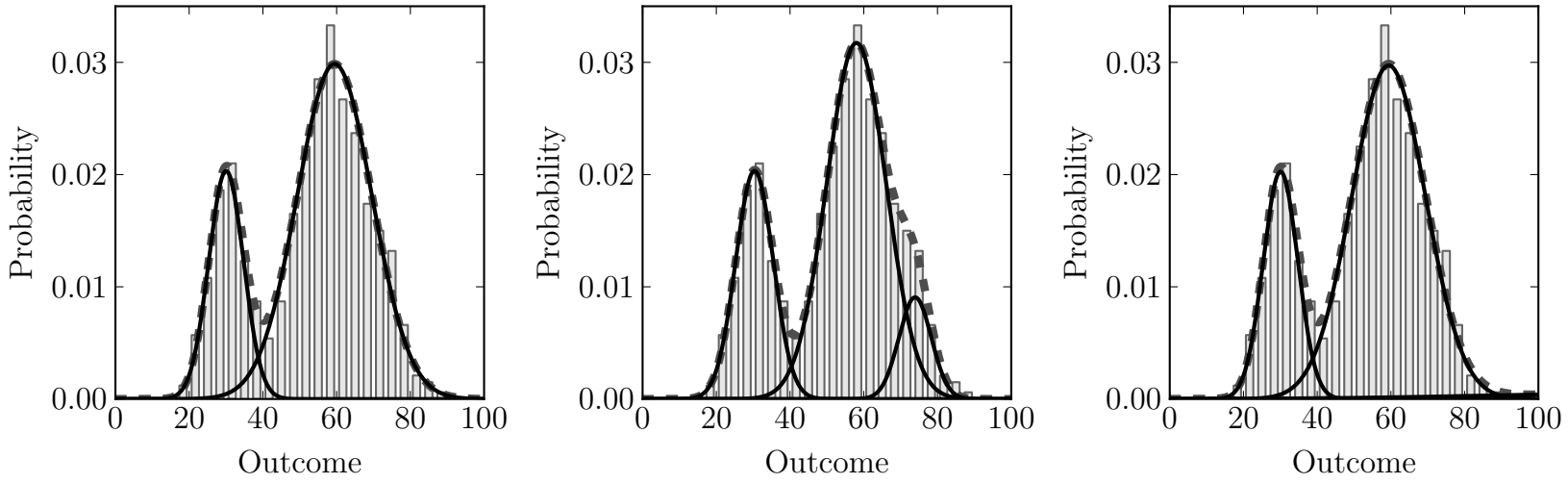

(a) n=2, unconstrained

$R^2 : 6.79e-05$

$B_{0,1} : 1.01e-02$

(b) n=3, unconstrained

$R^2 : 2.08e-05$

$B_{0,1} : 7.53e-03$

$B_{0,2} : 5.19e-07$

$B_{1,2} : 4.52e-02$

(c) n=3, constrained

$R^2 : 6.73e-05$

$B_{0,1} : 9.79e-03$

$B_{0,2} : 9.85e-03$

$B_{1,2} : 1.22e-03$

Figure 3.3: *Model complexity comparison.* Solid black lines represent individual subpopulations, dashed lines represent combined distribution functions. (a) A 2-peak fit with a minimum peak spacing of 1. (b) A 3-peak fit with a minimum peak spacing of 1. The addition of the third peak modestly lowered the overall residual, but at the cost of a dramatic increase in overlap between subpopulations (c) A 3-peak fit with a minimum peak spacing of 120. The optimizing routine set the third peak to a height of 0 in order to minimize the residual without violating the minimum peak-spacing constraint.

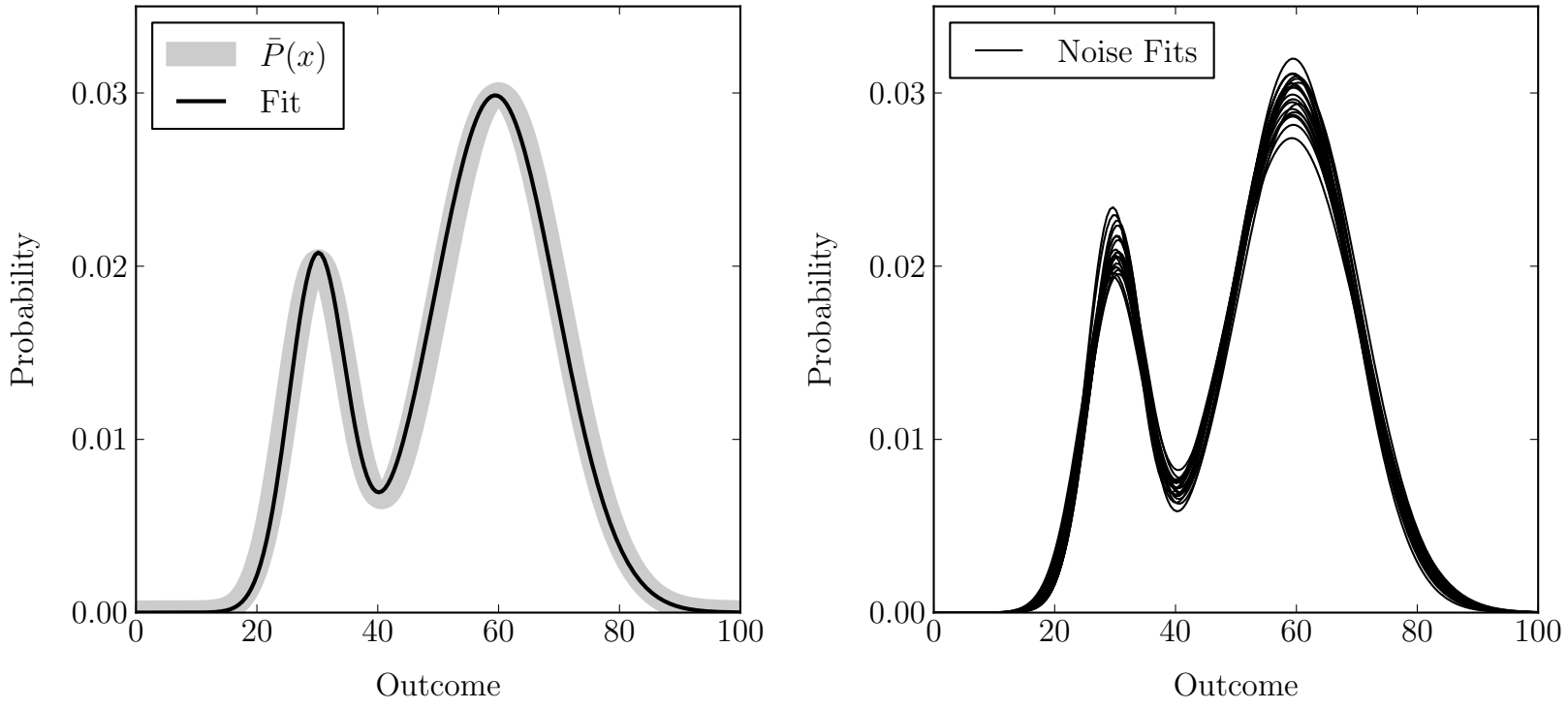

(a) Accuracy Testing

(b) Stability Testing

Figure 3.4: *Accuracy and noise stability testing.* (a) Comparison of a probability distribution function and the optimized model generated from a sample data set. (b) A series of models generated from unique noisy data sets showing a consistent qualitative behavior in the face of theoretical experimental noise.

CHAPTER 4

PATHOLOGY DISTRIBUTIONS IN AMD

4.1 Background

4.1.1 Morphological Changes in the Aging RPE

The human RPE undergoes significant changes with age, and many of these changes show characteristic spatial patterns in the retina. Macular RPE cells are taller and narrower than those in periphery (Streeten, 1969; Provis et al., 2005). This allows RPE cells to pack more tightly into the macula than the periphery, which is necessary to maintain RPE:photoreceptor ratios given the large increase in photoreceptor density seen in the central human retina. With increasing age the RPE cell layer undergoes thinning and loss of cells, but there is some disagreement as to the regional distributions of these changes. One study found that while RPE cells were lost in large numbers in the periphery of the human retina, macular regions failed to show any significant change in the number of RPE cells (Gao and Hollyfield, 1992). Another study, however, found that the overall RPE:photoreceptor ratio dropped with increasing age and did so throughout the retina (Dorey et al., 1989). These differences could be methodological or an artifact of the incredible diversity observed in various pathologies in human AMD patients. This diversity is not limited to interindividual observations though. Cell-to-cell heterogeneity is observed in nearly every measured signal or parameter in the aging human RPE, and the degree of heterogeneity appears to increase with age (Boulton, 2008; Burke and Hjelmeland, 2005).

4.1.2 Age-Dependent Accumulation of RPE Lipofuscin

In addition to morphological changes, the RPE becomes paler and increasingly autofluorescent with advancing age, and this is largely attributable to the loss of melanin and the accumulation of lipofuscin. RPE melanin granule content varies within the retina, with high levels in the periphery that decrease towards the posterior pole and then increase again in the macula. The lifetime loss of RPE melanin granules is mirrored by a geographically concurrent accumulation of RPE lipofuscin, and this is thought to result, at least in part, from the degradation of melanin granules and replacement with lipofuscin

(Feeney-Burns et al., 1984). This conversion from a melanin-dominant RPE in youth to a lipofuscin-dominant RPE in old age is of significant consequence to the oxidative health of the epithelium, as melanin is a powerful antioxidant, while lipofuscin contains powerful photo-oxidizing compounds (Sparrow et al., 2002).

One of the principal fluorophores in lipofuscin is N-retinylidene-N-retinylethanolamine (A2E), a molecule generated by the conjugation of all-trans retinaldehyde (ATR) with phosphatidyl ethanolamine (PE) (Eldred and Lasky, 1993). Much of our understanding of A2E and the damaging effects it has on the RPE come from the study of Stargardt macular dystrophy (SMD), an inherited childhood macular degeneration characterized by rapid accumulation of RPE lipofuscin (Stargardt, 1909). Autosomal recessive SMD, the most common form of the disease, is caused by mutations in the ABCA4 gene, which encodes a protein that assists in the movement of ATR-PE conjugates out of photoreceptors and into the RPE (Allikmets et al., 1997; Weng et al., 1999). Retinas of affected individuals demonstrate delayed recycling of retinoids, a buildup of ATR-PE conjugates within photoreceptors, and accelerated deposition of A2E in the underlying RPE. A2E is a photo-inducible oxidizer, and the excessive deposition of lipofuscin in SMD retinas causes light-induced oxidative damage to the RPE. Light deprivation offers some protection to mice carrying ABCA4 mutations, likely due to decreases in both the production of ATR and the photo-oxidation of A2E (Weng et al., 1999; Sparrow et al., 2002). Disease progression can also be slowed by other mechanisms, including enzymatic inhibition of retinoid recycling by the RPE (Radu et al., 2003). Taken together, these results indicate that lipofuscin accumulation is a normal byproduct of the visual cycle, and that SMD is simply an acceleration of an otherwise gradual aging process.

When aging human retinas are examined by photometric quantification of autofluorescent intensity, lipofuscin shows a spatial distribution very similar to that of rod density: low levels in the periphery that increase towards the posterior pole and then drop again in the fovea. This observation has led to suggestions that rods, rather than cones, are the principal source of lipofuscin in the aging human retina (Wing et al., 1978). It also suggests a mechanism through which the central retina would be more susceptible to the age-related accumulation of oxidative damage than the periphery. However, when examined by EM in vertical histological sections, lipofuscin fails to show an increased accumulated volume in the macula relative to the surrounding retina (Feeney-Burns et al., 1984). This is consistent with results from our laboratory that failed to identify significant regional variations in the

proportional volume of lipofuscin accumulation in vertical sections of aging human RPE (unpublished data, Marc Lab). This suggests that fluorophores reach higher concentrations in macular lipofuscin than in the periphery and that measuring the physical dimensions and location of lipofuscin deposition are insufficient to describe the distribution of oxidative burden on the RPE.

4.1.3 Aging Changes in Bruch's Membrane

The complex basement membrane underlying the RPE also shows significant changes with increasing age. Bruch's memrane gets thicker with increasing age, and it does so more in the macula than in the periphery (Guymer et al., 1999; Bird, 1991). Aging Bruch's membrane also becomes more brittle due to elastin loss and begins to show decreased overall structural integrity and the appearance of gaps, especially in neovascular AMD patients (Chong et al., 2005). Bruch's membrane shows an age-dependent accumulation of pentosidine, an advanced glycation endproduct (AGE) that has the capacity to elicit damaging immune reactions (Handa et al., 1999). Furthermore, mutations in the complement pathway have been robustly associated with an increased risk of developing AMD, and Bruch's membrane is one of the principle sites of deposition of complement proteins in the aging human retina (Anderson et al., 2010; citealpHageman:2005; Klein et al., 2005; Edwards et al., 2005; Haines et al., 2005).

4.1.4 Aging Changes in the Choriocapillaris

Paralleling the age-related development of changes in the RPE are a variety of age-related changes in the underlying choriocapillaris. While the appearance of these two sets of changes are closely associated, both spatially and temporally, the highly interrelated nature of these two tissues makes it difficult to establish which if any of the observed changes represent the initiation of the process. One the one hand, atrophy of the RPE could cause the choriocapillaris to decline from an absence of growth factors. On the other hand, decline of the choriocapillaris could starve the RPE of oxygen and nutrients, causing the RPE to atrophy. There are bodies of evidence and valid arguments for both cases, and it may turn out that both proposed mechanisms play a role.

Clinical imaging studies using indocyanine green (ICG) have observed a pattern of delayed choriodal filling in the maculas of patients with AMD (Pauleikhoff et al., 1999; Ciulla et al., 2002). These decreases in choroidal blood flow are associated with an increase

in scotopic threshold in the overlying retina and have been identified as a potential risk factor for progression to late-stage wet AMD (Chen et al., 1992; Boltz et al., 2010). Post-mortem examination of AMD eyes has revealed vascular differences in both the choroid and choriocapillaris that may explain these clinical findings. The density of the choriocapillaris has been observed to linearly decrease with advancing age, but this progression appears to be disrupted by AMD (Ramrattan et al., 1994). Earlier stages of AMD, in which the RPE layer is largely intact, appear to be associated with a panretinal increase in choriocapillaris density compared to age-matched controls (Spraul et al., 1996). However, macular regions with complete geographic atrophy of the RPE layer are consistently associated with a 50% decrease in the density of the underlying choriocapillaris and significant atrophy and narrowing of the surviving capillaries (McLeod et al., 2009; McLeod et al., 2002; Ramrattan et al., 1994). These apparently contradictory findings are actually quite consistent with the body of literature regarding the role of the RPE in maintaining the choriocapillaris. In-situ hybridization studies have identified the RPE as one of the primary sources of VEGF in the retina, and human RPE monolayers grown in primary culture have been shown to preferentially secrete VEGF to the side that normally faces the choriocapillaris. Furthermore, histological examination of human, primate, and rat retinas reveals that VEGF receptors in the choriocapillaris are asymmetrically distributed to the sides of capillaries facing the RPE (Blaauwgeers et al., 1999; Kim et al., 1999). A variety of experimental stressors have been shown to cause the RPE to increase VEGF expression and secretion both in vivo and in vitro, and this increase is also preferentially directed towards the choriocapillaris (Amano et al., 1998; Blaauwgeers et al., 1999; Ma et al., 2007; Howes et al., 2004). However, experimental insults that cause complete denudation of the RPE have been shown to cause rapid death of the underlying choriocapillaris, perhaps via VEGF depletion (Korte et al., 1984). Taken together, this body of evidence suggests a model in which stress to the RPE causes vascular hypertrophy, while complete death of the RPE causes vascular atrophy, potentially reconciling these two seemingly discordant clinical presentations of AMD. However, not all of the choroidal differences observed in AMD are as easily attributed to vascular maintenance by the RPE. Larger choroidal vessels, which are not known to be dependent upon the RPE, have been reported to decrease in number in the macula while increasing in size in the periphery of AMD eyes (Spraul et al., 1996). Furthermore, there is evidence of choriocapillaris atrophy in the vicinity of neovascular AMD lesions despite the presence of an intact RPE monolayer (McLeod et al.,

2009). Both of these findings call into question the role of RPE dysfunction in causing the altered choroidal perfusion observed in AMD eyes. It also remains possible that some of the vascular differences observed in AMD are actually predisposing factors rather than pathological consequences of the disease.

4.1.5 Glutathione in Retinal Disease

Glutathione (GSH) is a unique tripeptide (gamma-glutamyl cysteinyl glycine, γECG) that serves as a water-soluble antioxidant in essentially all cells. GSH can reduce peroxides either by direct reaction or through catalysis by glutathione peroxidase. Oxidation causes GSH to dimerize to glutathione disulfide (GSSG), which is then reduced back to GSH by glutathione reductase and other mechanisms. Decreased cellular GSH has been observed in stressed cells in some age-related neurodegenerative disorders but not in others. For example, GSH is reduced in substantia nigra pars compacta cells in Parkinson disease, and the degree of GSH reduction correlates to the degree of disease severity (Riederer et al., 1989). However, similar studies in Alzheimers disease and amyotrophic lateral sclerosis have thus far failed to demonstrate consistent alterations in cellular or plasma GSH levels, despite the fact that both diseases are thought to be closely related to age-related accumulation of oxidative damage (Schulz et al., 2000).

GSH is important in preventing lipid oxidation and can also detoxify reactive aldehydes, both of which are critical oxidative defenses in the RPE and photoreceptors. However, despite the prominence of oxidative damage in AMD research and the importance of GSH in cellular oxidative homeostasis, very little is known about the role of GSH in AMD (Winkler et al., 1999). While human plasma GSH is known to be progressively shifted towards its oxidized form with advanced age, studies in AMD patients have failed to consistently demonstrate an association with the development or severity of macular disease (Samiec et al., 1998; Cai et al., 2000; Nowak et al., 2003; Delcourt et al., 1999). Cultured RPE cells are protected from oxidative insults by exogenous GSH administration and by inducers of intracellular GSH synthesis, but it is not known whether GSH levels are changed in the RPE in AMD (Sternberg et al., 1993; Winkler et al., 1999). In addition to its role in detoxifying reactive oxygen species, GSH can also be used to detoxify other toxic compounds by conjugation via glutathione S-transferase (GST) enzymes, and mutations in GSTM-1 have recently been shown to be strongly associated with an increased risk of developing dry AMD (Güven et al., 2011). The body of evidence thus clearly suggests that

GSH is potentially an important factor in the development and progression of AMD, but it remains unknown how GSH levels and distributions change at the cellular level in the AMD retina.

4.1.6 Taurine in Retinal Disease

Taurine is the most abundant free amino acid in the body, exceeding the concentrations of all other amino acids by several times. However, while taurine is similar in structure and size to the amino acids used in metabolism and protein synthesis, taurine is itself very rarely incorporated into peptides, and the only known biochemical pathway that uses any significant quantity of taurine is the synthesis of bile salts. Taurine is zwitterionic at physiologic pH, making it highly hydrophilic while possessing no net charge, and its distribution in the body is almost entirely intracellular. These observations led to early speculation that the primary function of taurine was that of an osmolyte. Hypotonic swelling poses a significant risk to the sensitive ion gradients in excitable cells, so the nonionic nature of taurine makes it uniquely suited as an osmolyte for such tissues. Indeed, many cell types have been shown to temporarily expel taurine in response to acute hypoosmotic stress. Taurine is known to be especially critical for the maintenance of normal cellular volume in excitable cells such as neurons and myocytes, in which it is stored in very high concentration (Huxtable, 1992; Militante and Lombardini, 2004; Pasantes-Morales et al., 1999).

Taurine has also been demonstrated to assist in cellular defenses to oxidative stress in a variety of ways. While taurine itself is not a particularly strong reducing agent and does not react readily with reactive oxygen species (ROS), it provides an abundant amine pool that can react with hypochlorite, a highly toxic byproduct of cellular peroxide reactions. The resulting N-chlorotaurine is itself highly reactive and must be further reduced by glutathione to prevent lipid oxidation, which can otherwise result in damaging increases in hydraulic and electrical membrane conductivity. For this reason, increases in cellular taurine and glutathione are thought to help cells cope with increased oxidative stress and are considered markers for oxidative damage (see Huxtable, 1992 for review).

Photoreceptor taurine concentrations are among the highest in the body, and the delivery and maintenance of taurine in the retina appears to be prioritized over most other areas of the body. Animals deprived of dietary taurine deplete other tissues before retinal levels are allowed to drop, and the retina is the first tissue to be resupplied following

restoration of dietary availability. Furthermore, taurine deficiency causes rapid retinal degeneration, the severity of which is proportional to the degree of deficiency (Hayes et al., 1975; Schmidt et al., 1976; Sturman et al., 1978). However, it is not known precisely why photoreceptors are so uniquely dependent on taurine. While some studies have found evidence that osmotic stress contributes to neuronal death in various retinal degenerations, it remains to be conclusively demonstrated that the taurine dependency of photoreceptors can be attributed to a specific susceptibility to osmotic stress (Pasantes-Morales et al., 1999). Some studies have found that taurine supplementation protects photoreceptors from light damage and other insults thought to be oxidative in nature, so the oxidative protection roles of taurine may also be of great importance to photoreceptors (Keys and Zimmerman, 1999; Boldyrev et al., 1999). Taurine is also known to participate in regulation of RPE phagocytosis, a process critical for normal photoreceptor function (Ogino et al., 1983).

Taurine can be synthesized by cysteine sulfinate decarboxylase and cysteine dioxygenase, primarily by the liver (Junyent et al., 2009), and while endogenous synthesis appears to be sufficient for rodents, carnivores and omnivores (including humans) depend on dietary intake for the majority of their taurine requirement (Heller-Stilb et al., 2002). Once in circulation, taurine is delivered to the retina from both the retinal circulation and the choroid / RPE complex. Both RPE cells and retinal capillary endothelial cells have been shown to possess ATP-dependent taurine transporters (TauT) that capture taurine from the circulation, but it remains unclear how the taurine is then delivered in such high concentrations to specific retinal regions, nor is it understood how these distribution patterns change in response to retinal stress or what role they may play in promoting retinal function or survival (Pow and Crook, 1994; El-Sherbeny et al., 2004; Tomi et al., 2007).

4.2 Methods

4.2.1 Donor Retina Selection

The primary objective of this project was to quantify and map regional patterns in various parameters of retinal anatomy, pathology, and metabolism, and to examine the correlations between these factors and the severity of age-related retinal disease. The first step in this process was to develop a method to quantify each parameter and to generate complete quantitative profiles across the full range of retinal eccentricities in a diverse

selection of age-matched donor retinas with varying degrees of age-related eye disease. A group of four donor retinas was selected based upon apparent disease severity and quality of preserved tissue available for analysis. Donor retinas are summarized in Table **??**. Fundus photos are shown in Figures 4.2 - 4.5.

4.2.2 Photoreceptor Analysis

Photoreceptor density profiles were generated by mapping the locations and numerical densities of photoreceptor nuclei. Photoreceptor nuclei were identified by placing annotation marks on an alpha channel mask overlaid on a DAPI image of each retina, allowing the unique chromatin of photoreceptor nuclei to be easily visualized (Figure 4.1b). Complete retinal masks of photoreceptor nuclei were analyzed using the numerical density module in RetSpace to generate full profiles of photoreceptor nuclear density for each retina. Photoreceptor outer segments were not counted because the small size of rod outer segments would make identification and separation less reliable.

Cone photoreceptor density profiles were generated by mapping the locations and numerical densities of cone inner segments. Cone inner segments were identified by placing annotation marks on an alpha channel mask overlaid on a taurine image of each retina in which photoreceptor inner segments are prominently displayed on a dark background, allowing the unique conical shape to be easily identified (Figure 4.1a). The resulting masks were analyzed using the numerical density module in RetSpace to generate full profiles of cone inner segment densities for each retina.

4.2.3 RPE Analysis

RPE displacement profiles were generated by mapping the physical distance of separation between the basal aspect of the RPE and the underlying Bruchs membrane. These displacement masks represent a combination of drusen, basal laminar deposits, and exudative detachments secondary to choroidal neovascularization. Complete retinal masks of RPE displacement were analyzed using the profile module in RetSpace to generate full profiles of RPE displacement for each retina.

RPE thickness profiles were generated by analyzing masks of the full extent of the RPE layer. RPE masks were created as alpha channel masks overlaid on CRALBP or DAPI images in which the full extent of the RPE is easily visualized (Figure 4.1b). Complete retinal masks of the RPE were analyzed using the profile module in RetSpace to generate

full profiles of RPE thickness for each retina.

RPE nuclear density profiles were generated by mapping the locations and numerical densities of RPE nuclei. RPE nuclei were identified by placing annotation marks on an alpha channel mask overlaid on a taurine or DAPI image of each retina (Figure 4.1a). Complete retinal masks of RPE nuclei were analyzed using the numerical density module in RetSpace to generate full profiles of RPE nuclear density for each retina.

4.2.4 Bruchs Membrane and Choriocapillaris Analysis

Bruchs membrane thickness profiles were generated by analyzing individual annotations of the membrane as it separates choriocapillaries from the overlying RPE. Individual annotations were created by drawing lines onto an alpha channel mask overlaid on a DAPI channel in which the membrane is easily visible due to fixation-dependent autofluorescence (Figure 4.1b). Membrane thickness measurements were taken by analyzing the vertical height of individually segmented annotations using the segmentation module in RetSpace. The trend of measurements was smoothed using a simple mean filter with a boxcar size of 20 measurements.

Choriocapillaris coverage profiles were generated by analyzing complete masks of choriocapillaries. Individual capillaries were identified by masking the extent of the capillary on an alpha channel overlaid on a taurine image, in which viable endothelial cells are plainly visible against a dark background (Figure 4.1a). Complete retinal masks of choriocapillaries were analyzed using the coverage module in RetSpace to generate full profiles of choriocapillaris coverage factors for each retina.

4.2.5 Computational Molecular Phenotyping

Molecular profiles were generated for cone photoreceptors and RPE cells by analyzing taurine and glutathione images masked by user annotations of cone inner segments and RPE nuclei. Cone inner segments were identified by placing annotation marks on an alpha channel mask overlaid on a taurine image of each retina in which photoreceptor inner segments are prominently displayed on a dark background, allowing the unique conical shape to be easily identified. Inner segments were chosen for measurement over other areas because of the consistency of signals in the inner segment and the ease of accurate visual recognition. RPE nuclei were identified by placing annotation marks on an alpha channel mask overlaid on a DAPI image of each retina. The nucleus was chosen because

of the exclusion of melanin and lipofuscin granules, both of which disrupt histological signals in the cytoplasm. The small molecules examined in this study have been shown to be freely distributed between the cytoplasmic and nuclear compartments, so sampling of nuclear signal levels should be representative of cytoplasmic concentrations (Muller and Marc, 1990; Marc et al., 1995). Masks were processed with the segmentation module in RetSpace, then used to analyze median taurine and glutathione signals in each individual cell using the segmentation evaluation module in RetSpace. The resulting data sets were analyzed to examine the statistical distributions of signals within cell types, the spatial patterns of cell signal changes throughout the retina, and correlations between molecular signals and anatomic parameters. Statistical distributions of cell signals were analyzed using the population modeling module of RetSpace.

4.3 Results

4.3.1 Computational Molecular Phenotyping

The fovea of donor 2 is severely detached, presumably due to exudation from choroidal neovascularization (Figure 4.6). Though the offending vessels are not visible in the section, fixation-dependent autofluorescence reveals exudative debris filling parts of the detachment, visible on the DAPI channel. Several RPE cells are seen to have migrated away from the monolayer and lost their cuboidal shapes, assuming instead a globular appearance devoid of small molecular signatures. A small cluster of such cells can be seen in the center of the image having migrated into the outer nuclear layer where they appear to have become encapsulated by Müller cells. Other RPE cells still present in the monolayer also show disrupted small molecular signatures, and the entire monolayer appears thinner at the peak of the exudative lesion than in the surrounding macula. Photoreceptor densities also appear noticeably reduced in association with the lesion.

The macula of donor 3 contains several choroidal neovessels surrounded by regions of decimated retina, interspersed by regions of surviving photoreceptors (Figure 4.7). A large choroidal neovessel at the right edge of the field of view is located immediately under a surviving region of photoreceptors, indicating that the association between these gross lesions and the health of the overlying retina must be examined on larger scales. The external limiting membrane appears largely intact, as is the general structure of the overlying neural retina, indicating that retinal remodeling has not yet destroyed these gross anatomic features.

The RPE displays significant heterocellular variability in both taurine and GSH signals throughout many parts of the retinas of donors 0, 1, and 3 (Figure 4.8). Similar mosaicism of the RPE has been seen before in our lab in light-damaged mouse retina and hypoxia-damaged primate retina. The normal appearance of taurine and glutathione signatures in healthy primate RPE is completely homogenous such that individual cells cannot be distinguished (unpublished data, Marc lab).

4.3.2 Photoreceptor Anatomy

Numerical density profiles of photoreceptor nuclei per square millimeter as a function of retinal eccentricity were generated using a 1mm boxcar and low-pass Butterworth filtered ($n = 2, \lambda = 1mm$) (Figure 4.9). Lateral displacement of foveal cone somas causes a near-zero nuclear density within the fovea and an elevated nuclear density in the immediately adjacent region. The functional location of a photoreceptor in visual space corresponds to the physical location of the outer segment, not the soma, so the displacement of photoreceptor nuclei in the macular region must be taken into account when attempting to approximate regional variations in visual acuity by examining photoreceptor nuclear densities. The presence of a continuously high photoreceptor nuclear density in the center of the retina in donor 0 indicates that the section missed the fovea, though the slight depression indicates that the section is still in the macular region. The spatially-limited absence of photoreceptor nuclei in donors 1 and 2 indicate that the section passed through the fovea. Continuous absence of photoreceptor nuclei for a span of $\sim 20^{\circ}$ visual space in the central retina of donor 3 suggests significant loss of central photoreceptors and central vision. Donors 1, 2, and 3 all show decreased photoreceptor density in most retinal areas compared to donor 0.

Numerical density profiles of visible cone inner segments per square millimeter as a function of retinal eccentricity were generated using a 1mm boxcar and low-pass Butterworth filtered ($n = 2, \lambda = 1mm$) (Figure 4.10). Only cones whose distinct morphology could be readily identified were included in the masks, so the resulting density calculations should be considered a conservative underestimate. The degree of underestimation should be fairly consistent, so the shapes of the cone distribution curves should be accurate. Photoreceptor inner and outer segments are very closely associated, so regional variations in photopic (cone-dominant) vision can be more accurately inferred from cone inner segment densities than from photoreceptor nuclear densities. The profiles generated clearly show the foveal

spike in cone density, the absence of which in donor 0 again confirms that the section missed the fovea. A marked decrease in cone density in the macular regions of donors 2 and 3 relative to donor 1 suggests loss of cones and central photopic vision.

4.3.3 RPE Anatomy

Displacement profiles of the RPE as a function of retinal eccentricity were generated and low-pass Butterworth filtered ($n = 2, \lambda = 1mm$) (Figure 4.11). The locations of CNV lesions were included in the figure to demonstrate the close spatial association between CNV lesions and RPE displacement. Donors 0 and 1 show no CNV lesions and only minor RPE displacements in the macular region. Donor 2 shows a profound foveal RPE displacement up to $\sim 150\mu m$ in depth secondary to a large exudative lesion, presumably due to one of the CNV lesions clearly visible on fundoscopy though not visible in the histological section. Donor 3 shows several macular RPE displacements up to $\sim 30\mu m$ in depth that are closely associated with CNV lesions. Three of four donors show choriocapillaries penetrating through Bruchs membrane in the ora serrata.

Thickness profiles of the RPE as a function of retinal eccentricity were generated and low-pass Butterworth filtered ($n = 2, \lambda = 1mm$) (Figure 4.12). The locations of CNV lesions were included in the graphic to demonstrate the spatial association between CNV lesions and thinning and denudation of the RPE. All donors show a consistent trend of RPE thinning with increasing eccentricity, starting at $\sim 15\mu m$ in the macula and thinning to $< 10\mu m$ approaching the ora serrata. The RPE in donor 0 is consistently thicker than that of donors 1, 2, or 3. Donor 1 shows a slightly thinner RPE than donor 0 but lacks any significant disruptions in continuity. Donor 2 shows a similar pattern to that of donor 1 with the exception of a notably thinned area of RPE immediately over the fovea. Donor 3 shows significant thinning and even complete denudation of the RPE in several parts of the macula, with a close spatial association to the presence of CNV lesions. The margin of this large macular lesion is marked by a dramatic spike in RPE thickness to over $\sim 30\mu m$ immediately adjacent to a region of complete denudation.

Numerical density profiles of RPE nuclei per square millimeter as a function of retinal eccentricity were generated using a 1mm boxcar and low-pass Butterworth filtered ($n = 2, \lambda = 1mm$) (Figure 4.13). The group of donors show an overall trend of decreasing RPE nuclear density with increasing retinal eccentricity from $\sim 1000 nuclei/mm^2$ in the macula to $\sim 500 nuclei/mm^2$ at the ora serrata, though there exists significant variability between

individuals within this trend. Three of four donors show a dramatic 2 to 4-fold increase in RPE nuclear density for a small region at $\sim 30^{\circ}$ eccentricity, the origin of which is unknown. Donor 2 shows a noticeable decrease in RPE nuclear density immediately over the fovea. Donor 3 shows a near complete absence of identifiable RPE nuclei in much of the macula.

4.3.4 Bruch's Membrane and Choriocapillaris Anatomy

Profiles of the vertical thickness of Bruchs membrane as a function of retinal eccentricity show a consistent regional pattern with a maximum of $\sim 2.5\, to\, 3\mu m$ at $\sim 20^{\circ}$ eccentricity decreasing to $\sim 0.5\mu m$ at the ora serrata (Figure 4.14). Thickness profiles of the four donors are essentially indistinguishable in this region. All donors examined also showed a marked thinning of Bruchs membrane in the macular region, though neovascular retinas (donors 2 and 3) show noticeably more thinning in this region than their nonneovascular counterparts.

Choriocapillaris coverage factor profiles show a consistent increase from $\sim 60\%$ in the macula to $\sim 70\%$ at $\sim 20^{\circ}$ eccentricity, followed by a steady decline to $\sim 30\%$ at the ora serrata (Figure 4.15). The only deviation within the four donors profiled is the macula of donor 4, where the choriocapillaris coverage factor drops to around half that of the other donors profiled.

4.3.5 Cone Molecular Profiles

Cone inner segment glutathione profiles show a low glutathione concentration in cones throughout most retinal areas, with a consistent decreasing trend from intensity values of $\sim 32/255$ in the macula to near-zero in the periphery, followed by a precipitous increase at the ora serrata (Figure 4.16). Cone glutathione concentrations are also quite tightly grouped in most retinal areas, showing very little cell-to-cell heterogeneity. Donor 2 deviates from this overall pattern only in the fovea, where cone glutathione signals increase to over two-fold those of surrounding areas and become substantially more heterogenous. Donor 3 deviates from the overall pattern throughout the macula, where cone glutathione concentrations are both significantly elevated and substantially more heterogenous than in the maculas of the other donors. Signals in this donor return to the overall pattern past 20° eccentricity.

Focused analyses were performed to examine the relationship between cone glutathione concentrations and the displacement of the underlying RPE in donors 2 and 3. Donor 2

shows a close spatial correlation between RPE displacement and elevated cone glutathione in the fovea (Figure 4.17a). Bivariate plots comparing cone glutathione signals to the displacement of the underlying RPE show a noisy but consistent correlation between the two values (Figure 4.17b). A similar analyses of the central retina of donor 3 revealed a similar association between cone glutathione and RPE displacement but on a larger spatial scale (Figure 4.19).

Gaussian modeling of elevated cone inner segment glutathione signals from the foveal region of donor 2 ($-1^\circ to + 3^\circ$) (Figure 4.18) and the macular region of donor 3 ($-15^\circ to + 15^\circ$) (Figure 4.20) reveal single populations well-modeled by univariate distributions of a single random variable.

Cone inner segment taurine profiles show very high, tightly grouped signals with little variation across all retinal areas in all donors (Figure 4.21). A small number of cones with dramatically decreased taurine appear sporadically at all eccentricities in donors 0, 1, and 3, though this class of cones is absent from donor 2.

Bivariate plots comparing the taurine and glutathione concentrations of individual cone inner segments reveal a single, tightly grouped cluster in all donors (Figure 4.22). The sporadic low-taurine cones observed in donors 0, 1, and 3 show a similar variety of glutathione concentrations as the general population of high-taurine cones.

4.3.6 RPE Molecular Profiles

RPE nuclear glutathione signal distributions vary significantly between donors (Figure 4.23). Donor 2 shows a consistent decreasing RPE glutathione signal with increasing eccentricity, with tightly grouped signals that are very consistent cell-to-cell. Donor 1 shows a similar decreasing trend and tight grouping, but with a pronounced shelf at $\sim 20^\circ$ eccentricity where the glutathione signatures drop more suddenly than at other eccentricities. Donor 3 again shows a consistent, tightly-grouped decreasing trend with increasing eccentricity in all extramacular areas, but in the diseased macula this donor shows elevated RPE glutathione and marked heterogeneity between cells. Donor 0 shows substantially different RPE glutathione patterns than the other donors. The overall trend is towards slightly increased RPE glutathione signals with increasing eccentricity, and the signal shows significant bricking of glutathione signatures, where immediately adjacent cells have dramatically different signals (Figure 4.8).

Regions showing a high degree of cell-to-cell heterogeneity in RPE nuclear glutathione

signals were further analyzed to examine population distributions. Gaussian modeling of heterogenous RPE nuclear glutathione signals from the midperipheral retina of donor 0 (+20° to +50°) (Figure 4.24) and the full retina of donor 1 (−20° to +60°) (Figure 4.25) reveal a consistent pattern of population distributions. Both distributions feature a diverse group of higher-signal cells and a narrow, uniform group of low-signal cells.

Focused analyses were performed to examine the relationship between RPE nuclear glutathione concentrations and the displacement of the RPE in donors 2 and 3. Donor 2 shows a close, inverse spatial correlation between RPE displacement and RPE glutathione in the fovea (Figure 4.26a). A bivariate plot comparing RPE glutathione signals to RPE displacement in this region show a consistent inverse correlation between the two values (Figure 4.26b). A similar analysis of the central retina of donor 3 yielded a weak positive correlation between RPE glutathione and RPE displacement and an apparent association between RPE displacement and general heterogeneity in RPE glutathione (Figure 4.27).

RPE nuclear taurine signal distributions also vary significantly between donors (Figure 4.28). Donor 2 again shows a consistent, tightly-grouped signal trend that changes very little with increasing eccentricity. All other donors show substantial heterogeneity in RPE taurine signatures and constant "bricking" throughout retinal eccentricities (Figure 4.8). The only notable exception is donor 1, where the RPE taurine signatures are heterogenous in the central retina but very low and tightly-grouped in the peripheral retina.

Regions showing a high degree of cell-to-cell heterogeneity in RPE nuclear taurine signals were further analyzed to examine population distributions. Gaussian modeling of heterogenous RPE nuclear taurine signals from the midperipheral retina of donor 0 (+20° to +50°) (Figure 4.29), the full retina of donor 1 (−20° to +60°) (Figure 4.30), and the central retina of donor 3 (−15° to +20°) (Figure 4.31) reveal a consistent pattern of population distributions. Similar to glutathione distributions in the same cells, all three taurine distributions feature a diverse group of higher-signal cells and a narrow, uniform group of low-signal cells. The mid-periphery of donor 0 contained significantly more of the higher-taurine group, while the full retina of donor 1 and the central retina of donor 3 both contain more of the lower-taurine group.

Bivariate plots comparing the taurine and glutathione concentrations of individual RPE nuclei confirm the relationship between the two markers (Figure 4.32). Donors 0 and 1 show distinctly bimodal distributions, indicating that the low-taurine and low-glutathione subpopulations identified individually are in fact largely the same cells. Donor 3 shows

a similar pattern, though the bimodal distribution is less prominent. Donor 2 shows a very different pattern than the other donors, characterized by a tightly-grouped cluster of cells that appears to suggest a consistent linear relationship between RPE glutathione and taurine signals.

4.4 Discussion

4.4.1 Utility of the RetSpace Approach

The phenotypes of AMD retinas varies dramatically; likely a consequence of the long time periods required to develop the disease, the variability present in genetic susceptibility, and the dependence of the disease on a complex set of environmental risk factors. AMD research is further complicated by the need to address its distinctive regional pattern, knowledge of which is likely important for understanding its pathogenesis. Studies that oversimplify this regional and interindividual diversity are likely missing subtle relationships between anatomy and pathology that might help to explain its pathogenesis. The RetSpace system of histological analysis was developed to help fill in gaps in our knowledge regarding these complex spatial and multifactorial relationships. The simultaneous generation of full regional profiles of large numbers of relevant pathologies allows the nature and severity of disease to be more fully appreciated in each donor and provides a way to objectively compare the extent of pathologies between retinal areas and individuals. The analysis presented here demonstrates the utility of this method and identifies molecular targets that may serve as pathognomonic markers for early stress in the aging human sensory retina.

4.4.2 Morphological Analysis of AMD

Total photoreceptor density profiles were generated from user masks of photoreceptor nuclei (Figure 4.9). The creation of these masks is fairly straightforward and rarely requires users to make ambiguous classifications, so the counts and regional profiles generated should be very robust. While total photoreceptor density is in no way a complete assessment of visual acuity, it is an objective mile-marker in a one-way process from vision to blindness, and thus can serve as a reasonable measure with which to compare the severity of retinal disease between different areas and between individuals. This is especially useful given the high degree of regional and interindividual variation seen in the severity and type of other pathologies observed in aging human retinas.

In this study, total photoreceptor density profiles were used to grade the severity of retinal disease in our series of tissue donors. Donor numbers were assigned based upon total photoreceptor counts: donor 0 had the most robust photoreceptor layer, while donor 3 had the least. Donor colors in figures were also assigned in chromatic order from blue in the non-AMD donor to red in the most severely diseased retina. Total photoreceptor counts were found to reflect the severity of disease diagnosis found in patient records, as well as the severity of disease gathered from fundoscopy. One marked exception to this pattern is in donors 2 and 3. Fundoscopy in donor 2 looked far worse than that of donor 3 with more and darker macular neovessels, yet donor 3 showed consistently more advanced pathologies. This could be a sampling artifact of the specific piece of retina examined from each donor. Of some interest is the fact that photoreceptor counts in patients with worse AMD diagnoses were noticeably lower not just in the macula but throughout the entire retina (Figure 4.9).

Cone density profiles provide a similar metric to total photoreceptor counts but tell a story more specifically about central retinal function. It should be noted that our techniques miss many cones, but in a consistent manner. Thin sections provide only a small chance of seeing the profile of the cone outer segment, and only those with obvious outer segment morphology are included in annotation masks. These errors should, however, be systematic and consistent, meaning that while the cone density values are conservative underestimates, they are consistent underestimates. True cone densities in the human retina vary from $\sim 5000/mm^2$ in the periphery to $\sim 150,000/mm^2$ in the fovea, indicating that our measurement underestimates cone densities by a factor of approximately 2 (Provis et al., 2005). Cone densities were calculated by locating outer segments instead of cell somas, so this metric is not impacted by the lateral displacement of photoreceptor somas in the macula and thus provides a more direct indicator of visual function at a given retinal eccentricity. While the section taken in the non-AMD donor missed the cone-dense fovea, the remaining AMD donors show macular cone densities that are consistent with the severities of their diagnosed retinal disease, as well as their relative photoreceptor densities elsewhere in the retina. Donors 2 and 3 fail to achieve even half the cone densities present in donor 1, likely indicating significant central vision loss (Figure 4.10).

The RPE undergoes significant morphological changes with advancing age, so it was of great interest to quantify and map a variety of aspects of RPE morphology. The adult RPE is nondividing, and it is thought that cell death within the monolayer leads to a spreading

of the surrounding cells to fill in gaps. If such a process were to continue indefinitely it would be expected to reach a breaking point at which this gap-filling would fail, leading to breaks in the RPE such as those characteristic of more severe forms AMD. It is thus tempting to hypothesize that RPE cells die faster in the RPE, causing this breaking point to be reached sooner than in the periphery. While age-dependent RPE cell dropout has been identified in the periphery, no such process has been confirmed for the macula, though it should be emphasized that the existing data is far from complete. Furthermore, none of the data thus far gathered regarding the size, number, and position of RPE cells in aging human retinas can be tied to data regarding other retinal pathologies (Boulton, 2008). Data produced in this study indicate the presence of RPE cell thinning and dropout in the macula of aging human retinas and ties this loss to the presence of other retinal pathologies (Figures 4.11, 4.12, 4.13).

Initial impressions revealed that donors 2 and 3 both show noticeably lower RPE nuclear densities in the macular region than their less-affected counterparts (Figure 4.13). Closer examination revealed more telling patterns. RPE thickness profiles in donors 1 and 2 are nearly indistinguishable at all retinal eccentricities except the fovea, where donor 2 shows a profound region of RPE thinning immediately associated with a substantial sub-RPE exudative lesion (Figure 4.12). Donor 2 also shows a dip in RPE nuclear density at this location, indicating that the RPE may be dying, spreading, and thinning in association with this foveal lesion. Donor 3, who shows a significant amount of displacement of the macular RPE associated with several neovascular lesions, also shows a significant thinning and even complete denudation of the RPE in this region (Figure 4.11). Donor 3 also shows a substantial dropout of RPE nuclei relative to the periphery, where this is essentially indistinguishable from the other donors. Donor 3 also shows a substantial accumulation of RPE at the edge of the neovascular region, a characteristic we have observed adjacent to regions of RPE denudation in several other AMD patients and animal models of AMD (unpublished data, Marc Lab). While these findings are all isolated and need confirmation in more patients, they clearly demonstrate that the RetSpace analysis method is perfectly positioned to characterize and map the spatial dropout of RPE cells with increasing age and to validate these findings by correlating these morphological changes with retinal pathologies of known significance.

Thickness profiles in all four donors presented here are qualitatively consistent with previous observations that Bruch's membrane thickens disproportionately in the macula

with advanced age (Guymer et al., 1999; Bird, 1991). Our results show a macular thickness of $\sim 2-3\mu m$, which, compared to values generated by Ramrattan et al, is on the low-end of normal for donors in their 70s (Ramrattan et al., 1994; Figure 4.14). This could be an indicator of metholdological differences: we identified the membrane by virtue of it's autofluorescent signal when fixed with gluteraldehyde, while Ramrattan et al. visualized the membrane using the Mallory triple stain for connective tissues. It could also be a result of the fact that two of our donors had wet AMD, a condition that has been associated with a macular thinning of Bruch's membrane (Chong et al., 2005). Consistent with the findings of this study, we observed that wet AMD patients (donors 2 and 3) showed noticeably thinner Bruch's membranes relative to their age-matched controls. The peripheral retinas of all donors were essentially indistinguishable in terms of Bruch's membrane thickness profiles. In fact, the foveal region is the only place where the more severe AMD patients differed noticeably from their less-diseased counterparts.

Choriocapillaris coverage quantifications were generated in such a way as to make them compatible with previous large-scale studies. Ramrattan et al. showed a clear trend of decreasing choriocapillaris coverage (referred to as *capillary density* in their terminology) in the macula with increasing age (Ramrattan et al., 1994). Three of four donors in our study had macular coverage factors of ~ 0.6, which is precisely where Ramrattan et al. would predict based simply upon their ages (Figure 4.15). Donor 3, however, has a macular choriocapillaris density that drops to around half that of age-matched counterparts. Given the significant denudation of the overlying RPE, this finding is very consistent with previous reports that the choriocapillaris under regions of atrophic RPE drops to $\sim 50\%$ its original density (McLeod et al., 2009; McLeod et al., 2002; Ramrattan et al., 1994). These consistencies with established large-scale studies indicate that the measurement and profiling systems implemented in RetSpace are comparable to other techniques, allowing data sets generated in our system to benefit from a wealth of existing measurements validated on large numbers of donor retinas.

4.4.3 Metabolic Analysis of AMD

Cone GSH signals are very low and very tightly grouped in most retinal areas, with a subtle but consistent trend in all donors towards higher cone GSH in the central retina than in the periphery (Figure 4.16). The exceptions to this pattern are the central retinas of the more severely affected donors, where dramatic increases are observed in cone GSH

signals. When these regions are examined in detail, two interesting patterns emerge. First, cone glutathione levels are elevated specifically in regions in which the RPE is detached from Bruch's membrane secondary to neovascularization (Figures 4.17a, 4.19a). Second, the degree of the signal increase in cone GSH shows a loose, direct correlation to the degree of RPE detachment (Figures 4.17b, 4.19b). This suggests that for this type of lesion, increased cone GSH may be an important marker of photoreceptor stress. When cone GSH signals from these regions are modeled, they appear to be perfectly gaussian distributions of a random variable about a common mean, indicating a single loosely-controlled population (Figures 4.18, 4.20). Cone taurine concentrations in the same cells show very little variability (Figure 4.21), and no significant correlation to GSH levels in the same cells (Figure 4.22), indicating that the increase in GSH signals is not simply a nonspecific trapping of small molecules. Rather, the increase in GSH in these cells appears to be a specific though heterogenous increase in focal regions immediately associated with lesions. It should be noted that the human macula lacks the retinal vascular arcades present elsewhere in the neural retina, meaning that sub-RPE detachment in the human macula would separate the RPE and photoreceptors from their only blood supply (Provis et al., 2005). Hypoxic insult has been linked to oxidative stress in a variety of cell types, so it is possible that the increase in GSH in these cells is a response to the increased oxidative burden experienced during lesion-induced hypoxia (Sternberg et al., 1993; Schulz et al., 2000; Ha et al., 2006).

RPE GSH is much higher than in cones, but still shows a general decreasing trend with increasing eccentricity in most patients (Figure 4.23). This trend is most pronounced in donors 1 and 2, who both show a distinct "shelf" appearance where RPE GSH levels drop rather suddenly after $\sim 30^{\circ}$ eccentricity. This consistent spatial pattern of higher GSH levels in central cones and RPE cells is consistent with the widely-held view that the central retina is subject to greater levels of oxidative stress than the periphery (Provis et al., 2005).

RPE GSH levels also differ from cone signals in terms of the complexity of population distributions. In contrast to the tightly-grouped distributions seen in cone GSH signals, RPE GSH signals were observed to be highly heterogenous, with great variability between even immediately adjacent cells. When population distributions are examined, RPE GSH signals appear to separate into two distinct subpopulations in most retinas, but the spatial distributions of the two distinct subpopulations varies greatly between individuals (Figures

4.24, 4.25). While the high and low GSH populations are spatially mixed in donor 0, they are nearly completely separated in donor 1, with the central half of the retina showing higher RPE GSH concentrations, the peripheral RPE showing the lower GSH signal, and the transition shelf occurring sharply at $\sim 30^{\circ}$ eccentricity with very few cells at intermediate signal levels. Donor 3 is missing large areas of RPE in the macula, but surviving RPE cells show a substantial mean elevation and a significant increase in heterocellular variability in GSH content compared to the lower, very tightly regulated RPE GSH concentrations seen elsewhere in the same retina. This pattern is almost completely opposite to that seen in donor 0, where macular RPE cells have the lowest and most homogenous GSH signals but are surrounded by higher, more variable RPE GSH signals in all extramacular areas (Figure 4.23).

Detailed examination of RPE GSH levels in the fovea of donor 2 indicate that the RPE overlying the large sub-RPE exudative lesion has markedly decreased GSH (Figure 4.26). Given that the photoreceptors in this area showed a dramatic increase in GSH levels, this result suggests the possibility that GSH was transported from the RPE into the photoreceptors. Cultured RPE cells have been shown to possess the cellular machinery required for bidirectional GSH transport, including a Na+-dependent transport mechanism on the apical surface of nontransformed human RPE cultures, but it remains unknown what role this plays in the retina *in vivo* (Davidson et al., 1994; Lu et al., 1995; Kannan et al., 2001). Detailed examination of RPE GSH levels in the central retina of donor 3 tells a very different story than in donor 2 (Figure 4.26). Surviving RPE cells overlying the severely damaged macula show a wide variety of GSH levels, with some showing very high levels and others showing very low levels. The overall trend, however, is to higher GSH in these RPE cells, not lower as was seen in donor 2.

RPE taurine distributions show similar amounts of variability, both between individual cells and between individuals (Figure 4.28). Donors 0, 1, and 3 all show significant degrees of heterocellular variability in RPE taurine concentrations. As with RPE GSH population distributions, RPE taurine distributions in these retinas appear to separate into two distinct subpopulations (Figures 4.29, 4.30 and 4.31), though the spatial distribution of the two distinct subpopulations again varies between individuals. While the high and low taurine populations are spatially mixed in donors 0 and 3, they are again nearly completely separated in donor 1, with the central half of the retina showing higher and more variable RPE taurine signals, the peripheral RPE showing lower GSH signals, and the transition

shelf occurring in the mid-periphery. The shelf in taurine signals appears more centrally than it did for RPE GSH signals and is less stark, containing more cells of intermediate signal levels (Figure 4.28).

Bivariate analysis of RPE TT and GSH signals confirms that the bimodal distributions observed independently in both signals are in fact indicative of the same two subpopulations (Figure 4.32). The first and more numerous subpopulation contains moderate levels of both taurine and GSH and is fairly diverse in both signals. A second, smaller subpopulation contains low levels of both markers, though both signals are still significantly higher than background. The coincidence of dramatically lower levels of both signals in this smaller subpopulation suggests the possibility that the cells are dying, becoming permeable, and nonspecifically dialyzing small molecules from the cytoplasm. The possibility of a postmortem artifact must be considered here, though it seems unlikely. Our laboratory has studied postmoretm artifacts in these very signals in animal models and never observed these phenomena (unpublished data, Marc Lab). Furthermore, the postmortem times of these patients are all similar, and donor 2 shows absolutely none of the described phenomena despite having postmortem time similar to the other donors. However, the simple record of a time between death and fixation likely misses important information regarding tissue stress surrounding death. It is not known, for example, which donors were placed on respirators prior to death or for how long.

4.5 Conclusions

Using CMP and the RetSpace software system we have generated a robust profiling system to quantify and compare the severity of a host of different anatomic and pathologic features between different retinal areas and between individual tissue donors. By demonstrating conformity of our individual characterizations to the results of previous large-scale studies, we have shown that analyses using our system can benefit from the wealth of existing morphological data available from other laboratories. We have provided tentative confirmatory data regarding certain aspects of the combinatorial nature of AMD pathology, and have identified key molecular targets as candidates for early stress markers in the aging human retina. The RetSpace system has proven a useful tool in the study of the spatial and combinatorial variability of retinal disease.

Table **??**

Summary of Donor Retinas

Name	Age	Sex	Diagnosis	Drusen	Δ Pigment	CNV	Postmortem Time
Donor 0	71	M	Non-AMD (Glaucoma)	+	-	-	2:41
Donor 1	76	M	Early Dry AMD	-	+	-	$<$ 4:00
Donor 2	79	F	Early Wet AMD	-	-	+	$\sim$ 3:00
Donor 3	77	F	Late Wet AMD	+	+	+	$\sim$ 3:00

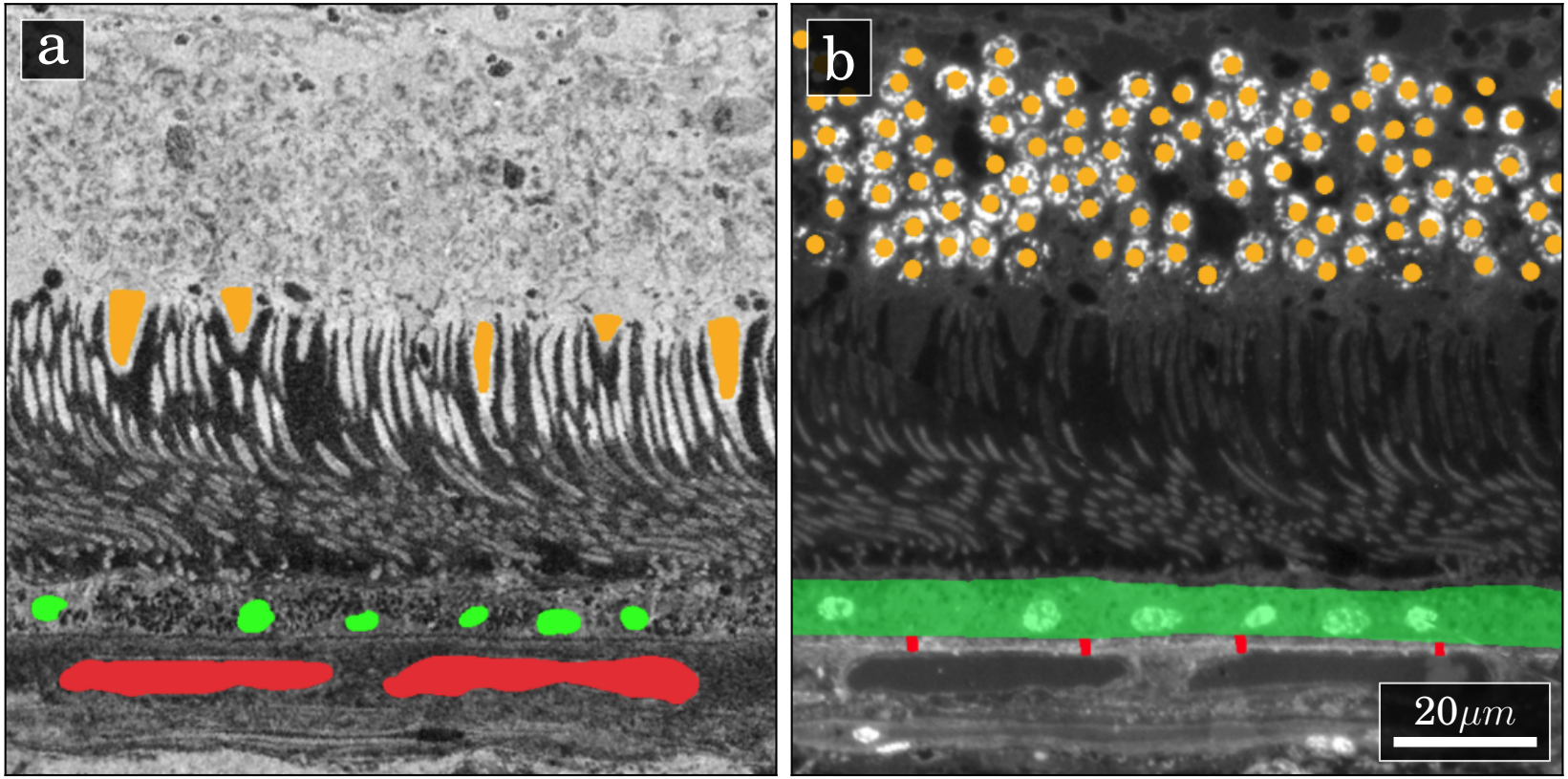

Figure 4.1: Examples of user-supplied image annotations. (a) Taurine immunohistochemistry with annotations displayed as colored alpha channel masks. Orange indicates cone inner segments, green indicates RPE nuclei, and red indicates choriocapillaris vessels. (b) DAPI image with annotations displayed as colored alpha channel masks. Orange indicates photoreceptor nuclei, green indicates the full vertical extent of the RPE, and red indicates samplings of Bruch's membrane adjacent to choriocapillaries.

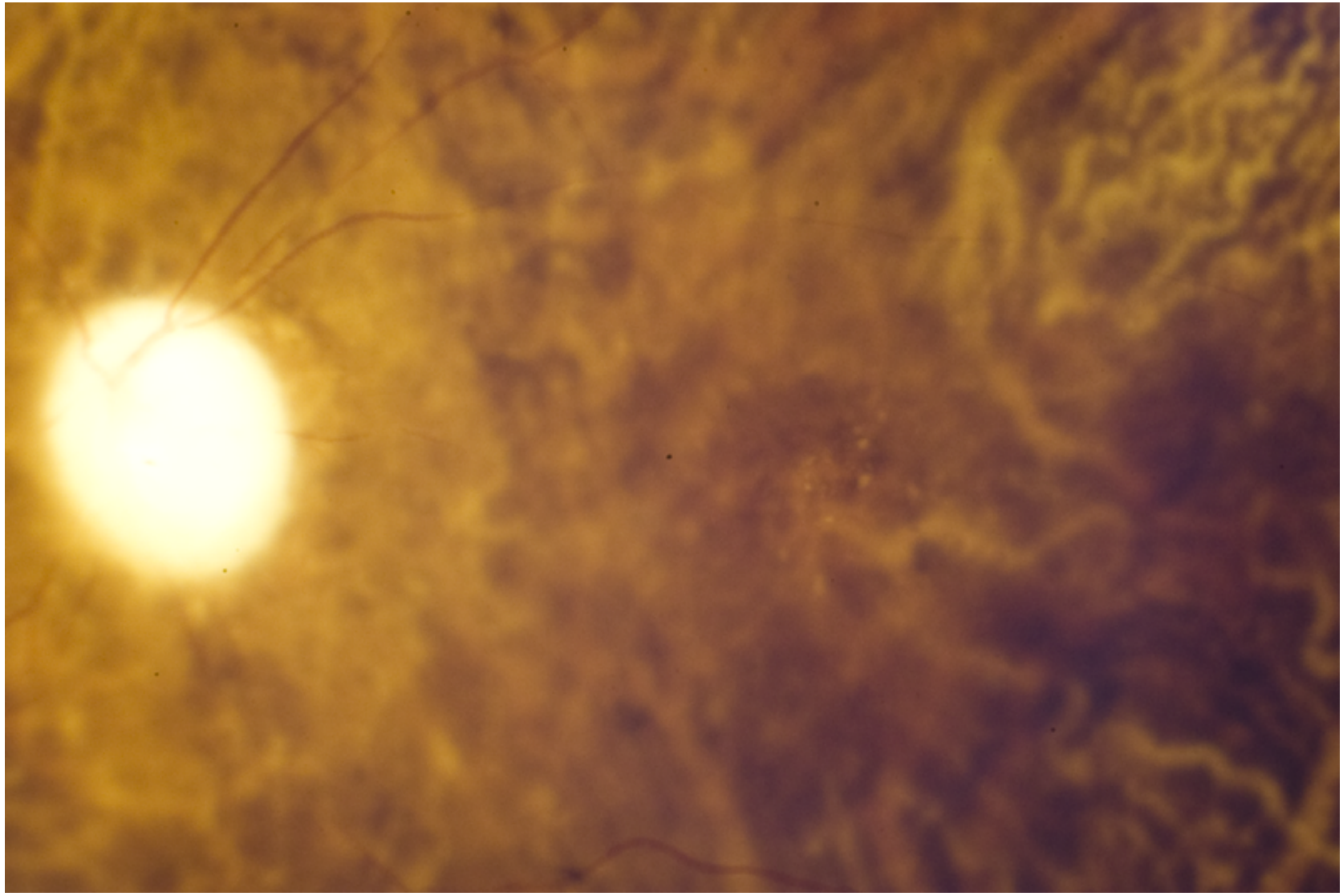

Figure 4.2: Postmortem fundoscopy of Donor 0.

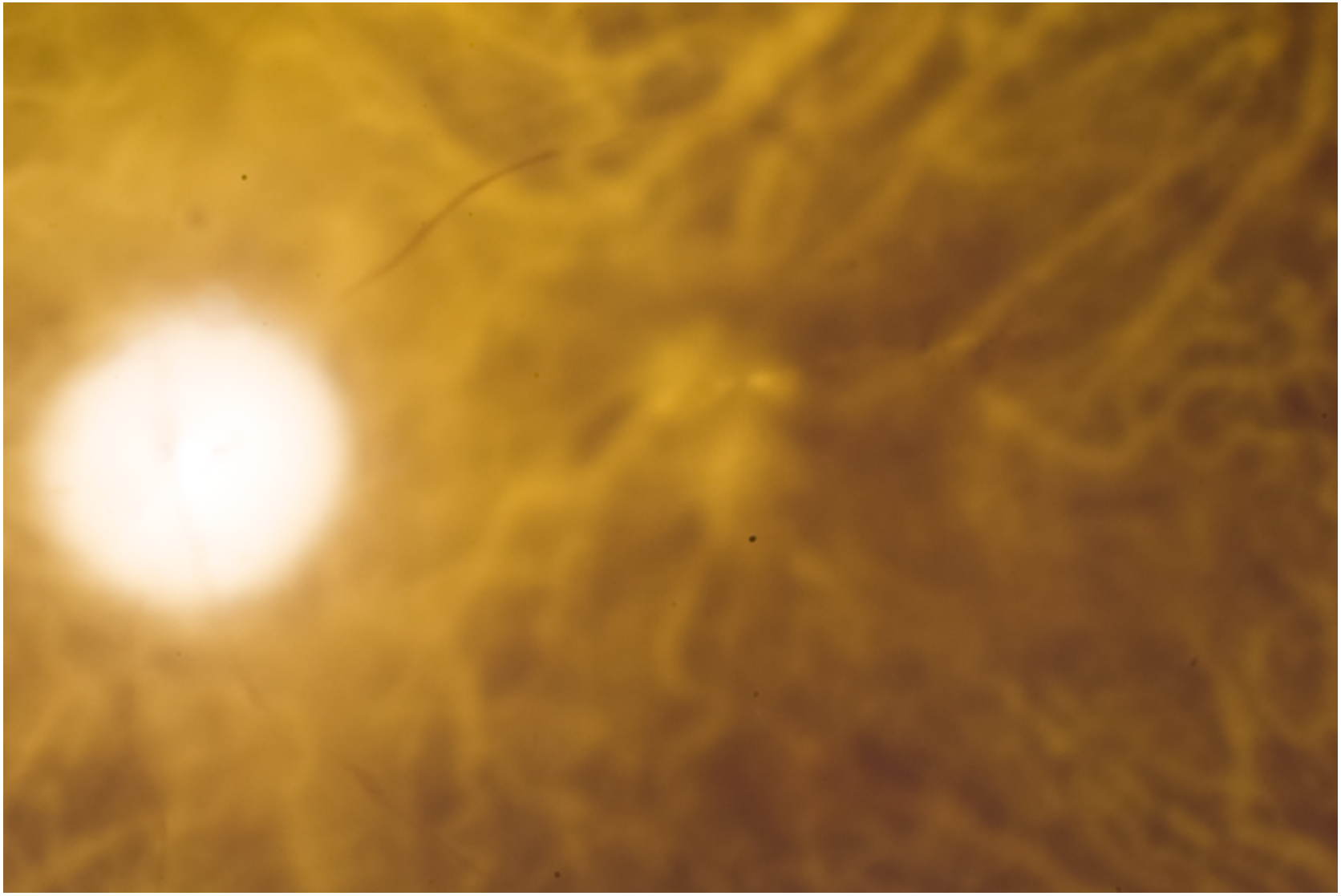

Figure 4.3: Postmortem fundoscopy of donor 1.

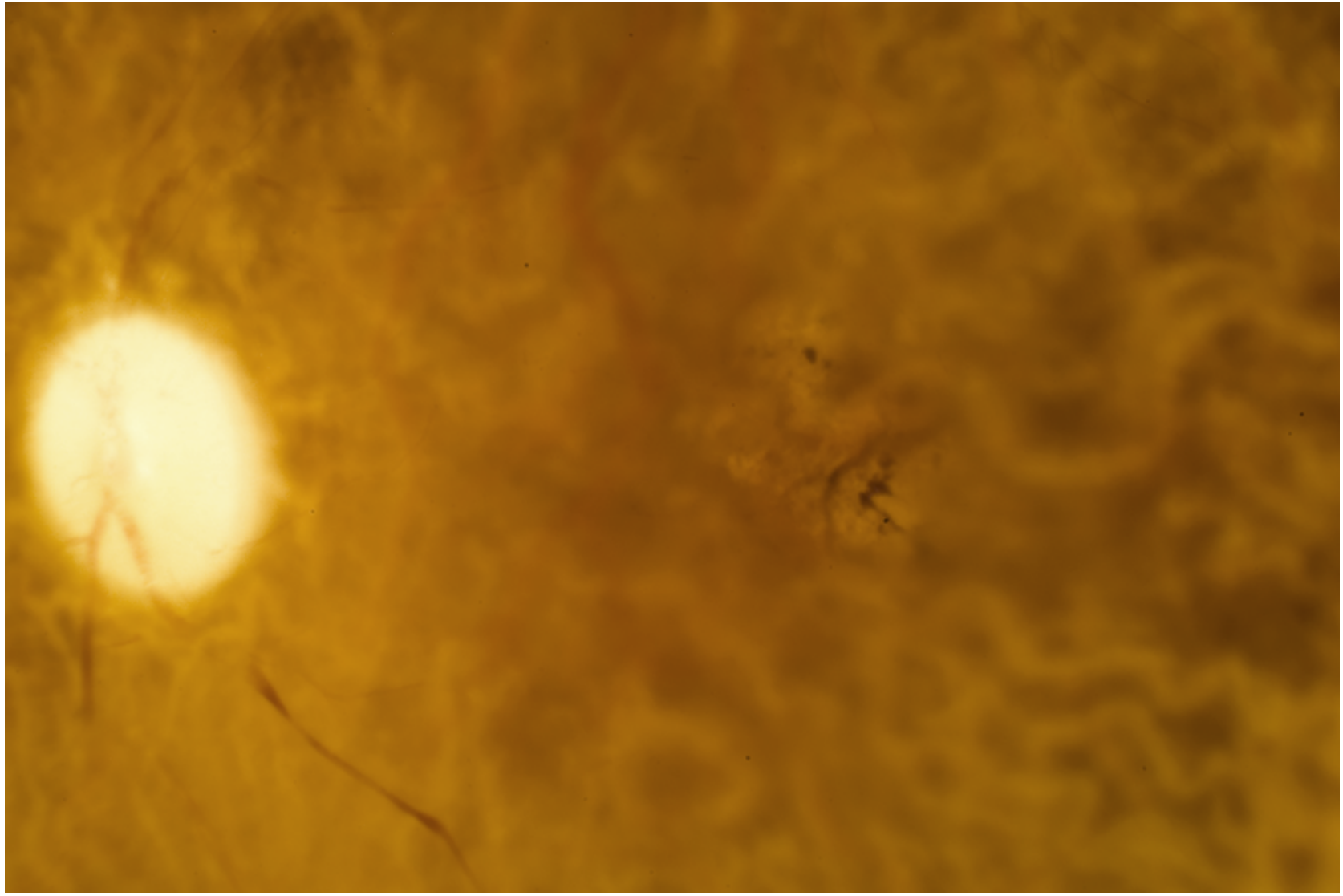

Figure 4.4: Postmortem fundoscopy of donor 2.

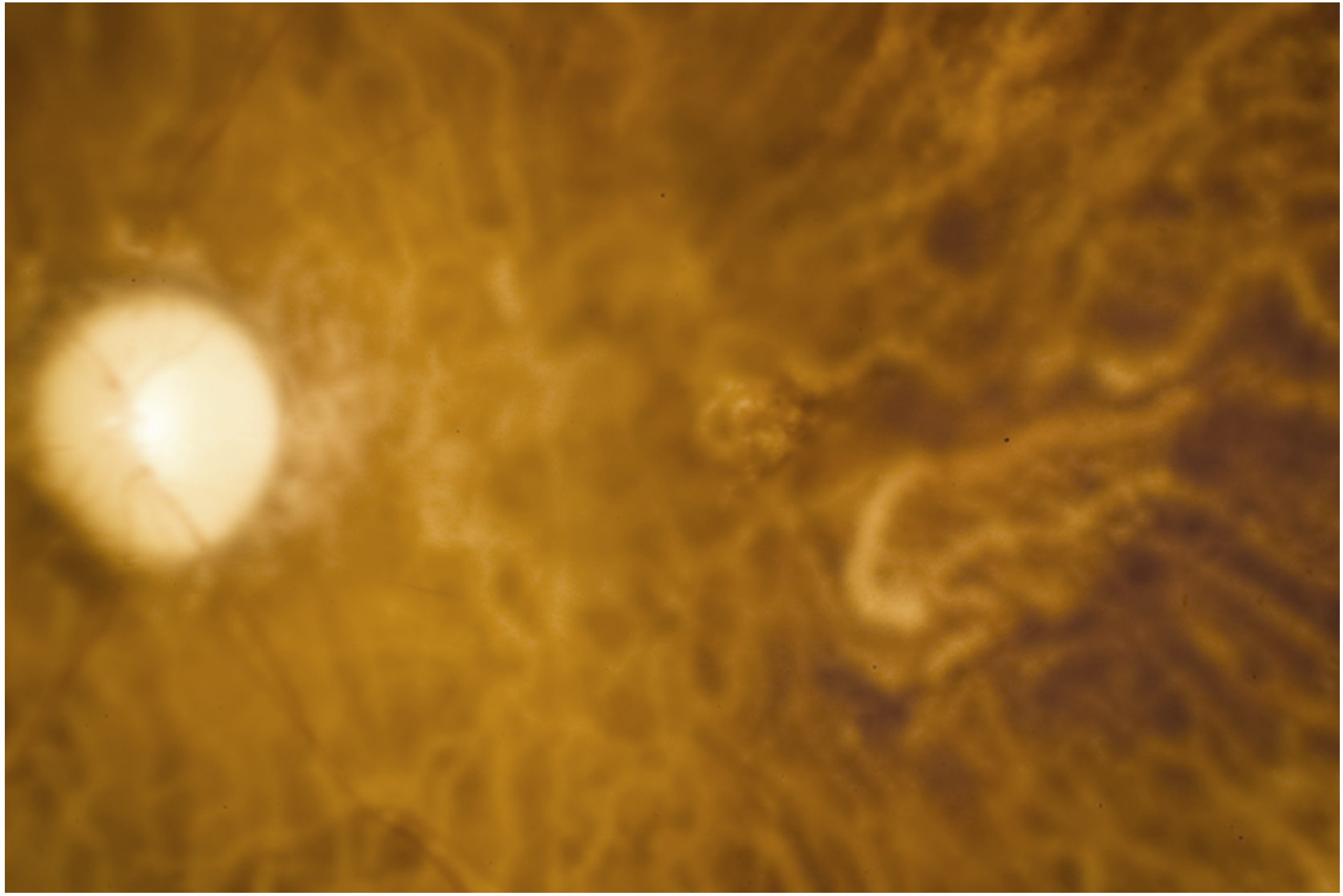

Figure 4.5: Postmortem fundoscopy of donor 3.

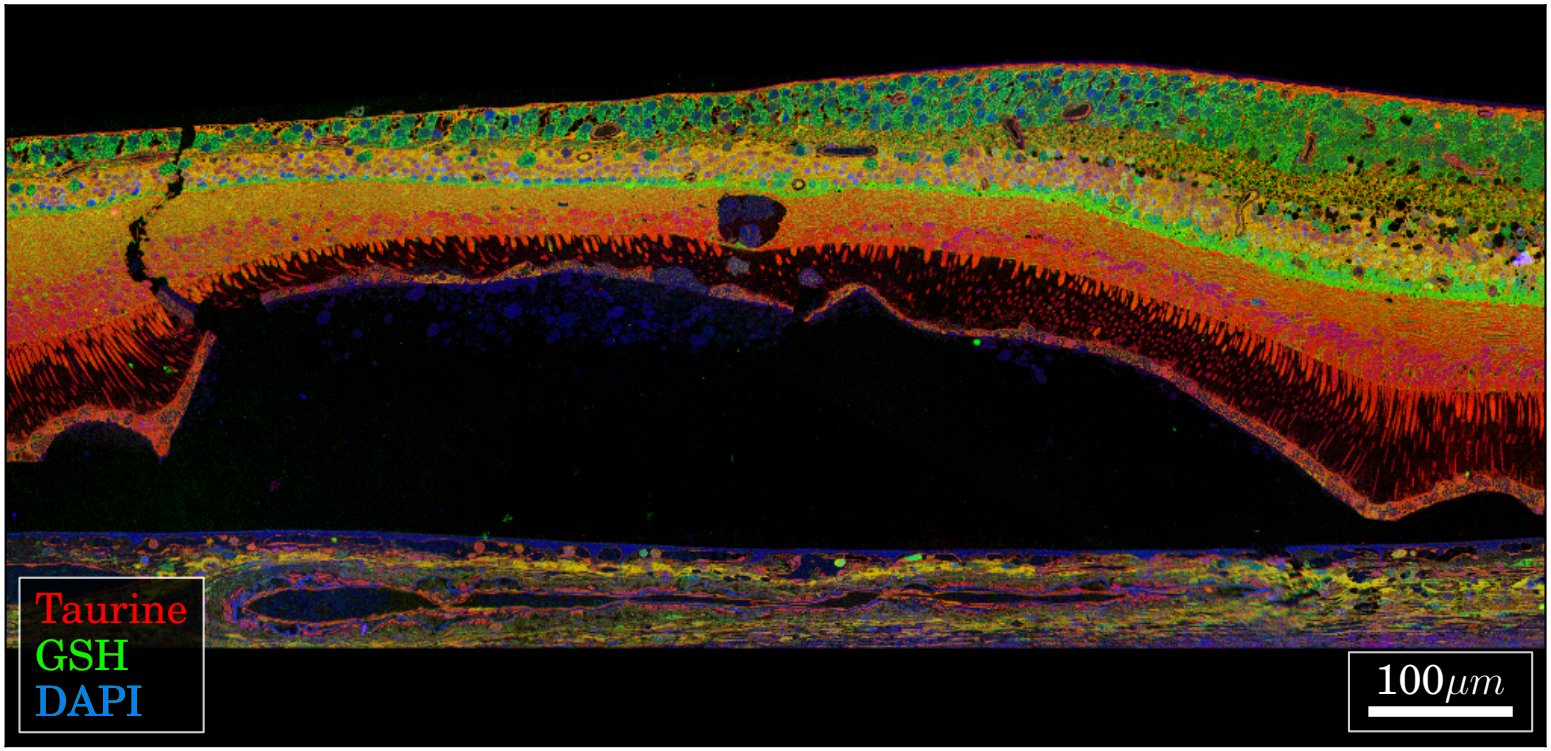

Figure 4.6: Detailed examination of the fovea of donor 2. RGB composite of Taurine, Glutathione, and DAPI, respectively. Center of image is located $\sim 1^{\circ}$ lateral to the fovea. All images are background corrected as described in Chapter 2.

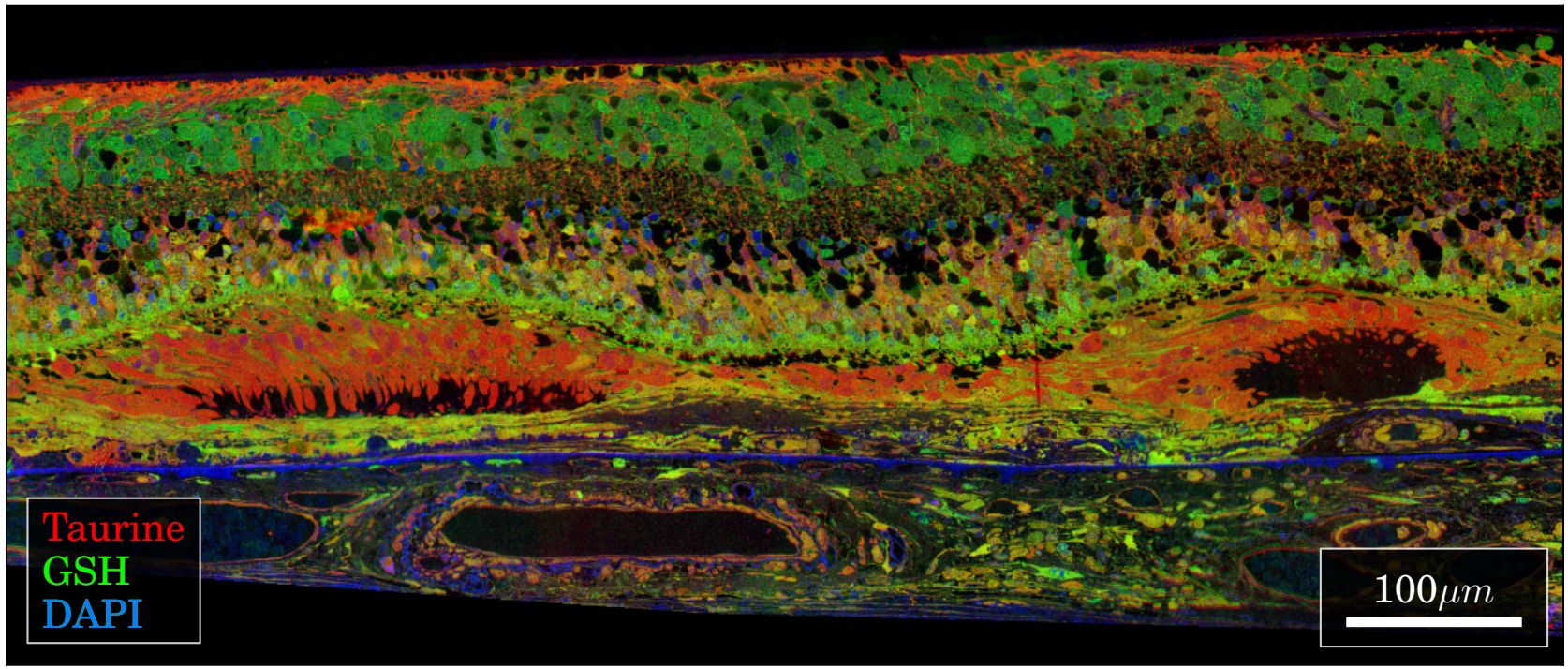

Figure 4.7: Detailed examination of a portion of the macula of donor 3. RGB composite of Taurine, Glutathione, and DAPI, respectively. Center of image is located $\sim 5^{\circ}$ medial to the fovea. All images are background corrected as described in Chapter 2.

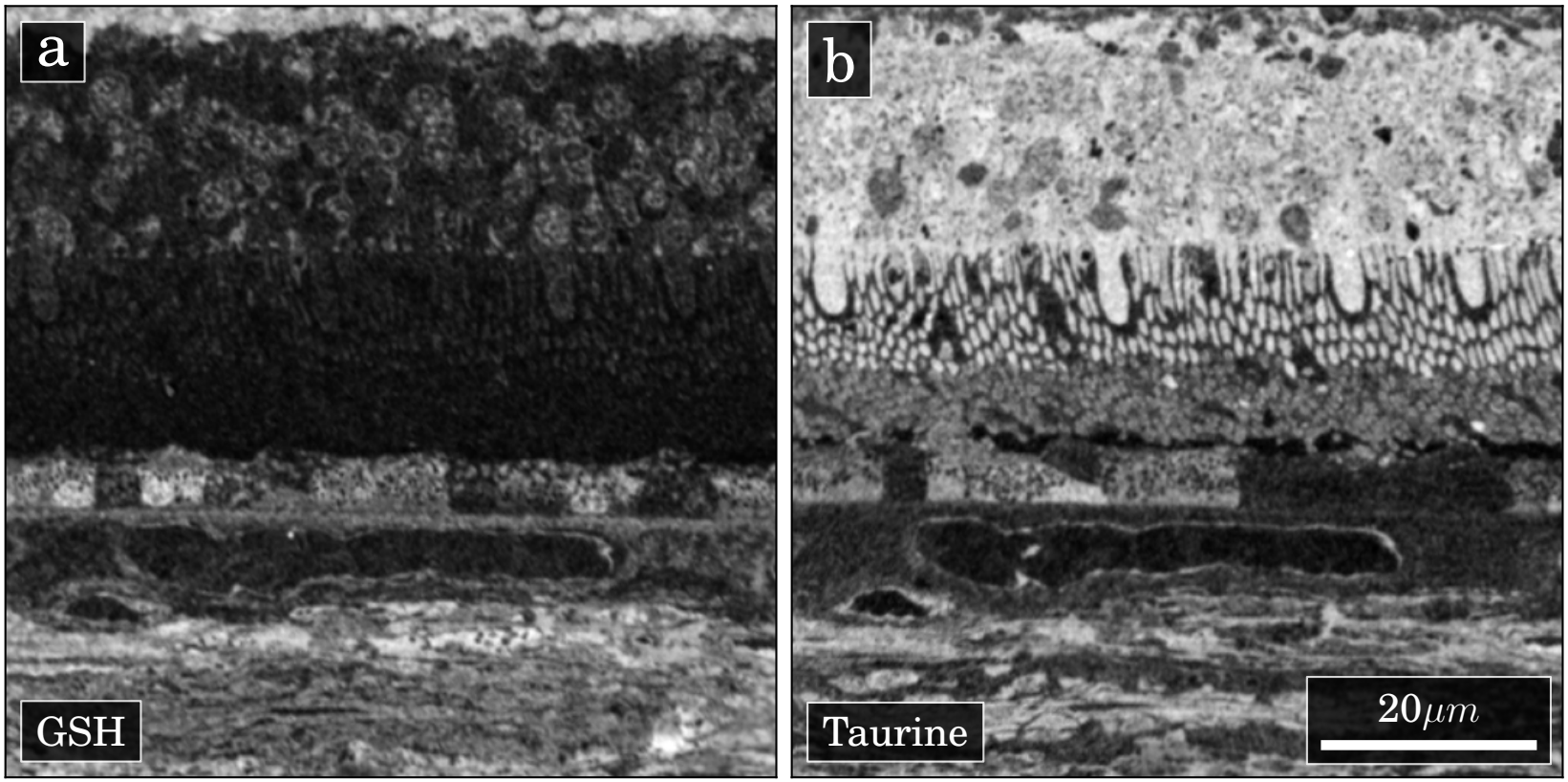

Figure 4.8: Sample images from $\sim 30^{\circ}$ eccentricity in donor 0 showing dramatic mosaicism of the RPE in both glutathione (a) and taurine (b) signals. All images are background corrected as described in Chapter 2.

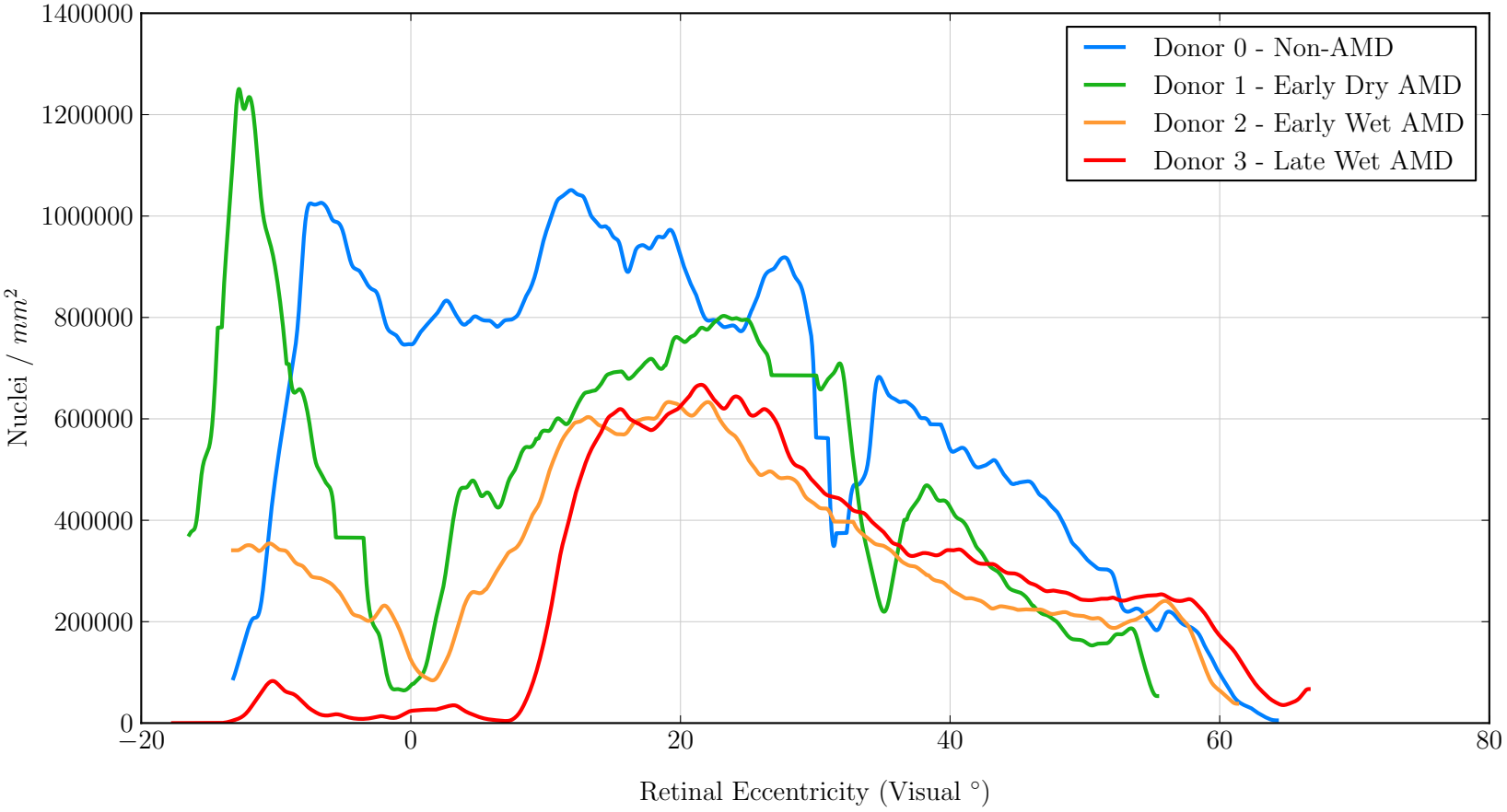

Figure 4.9: Profiles of the numerical density of photoreceptor nuclei per square millimeter as a function of retinal eccentricity. Profiles were generated using a 1mm boxcar and low-pass Butterworth filtered ($n = 2, \lambda = 1mm$).

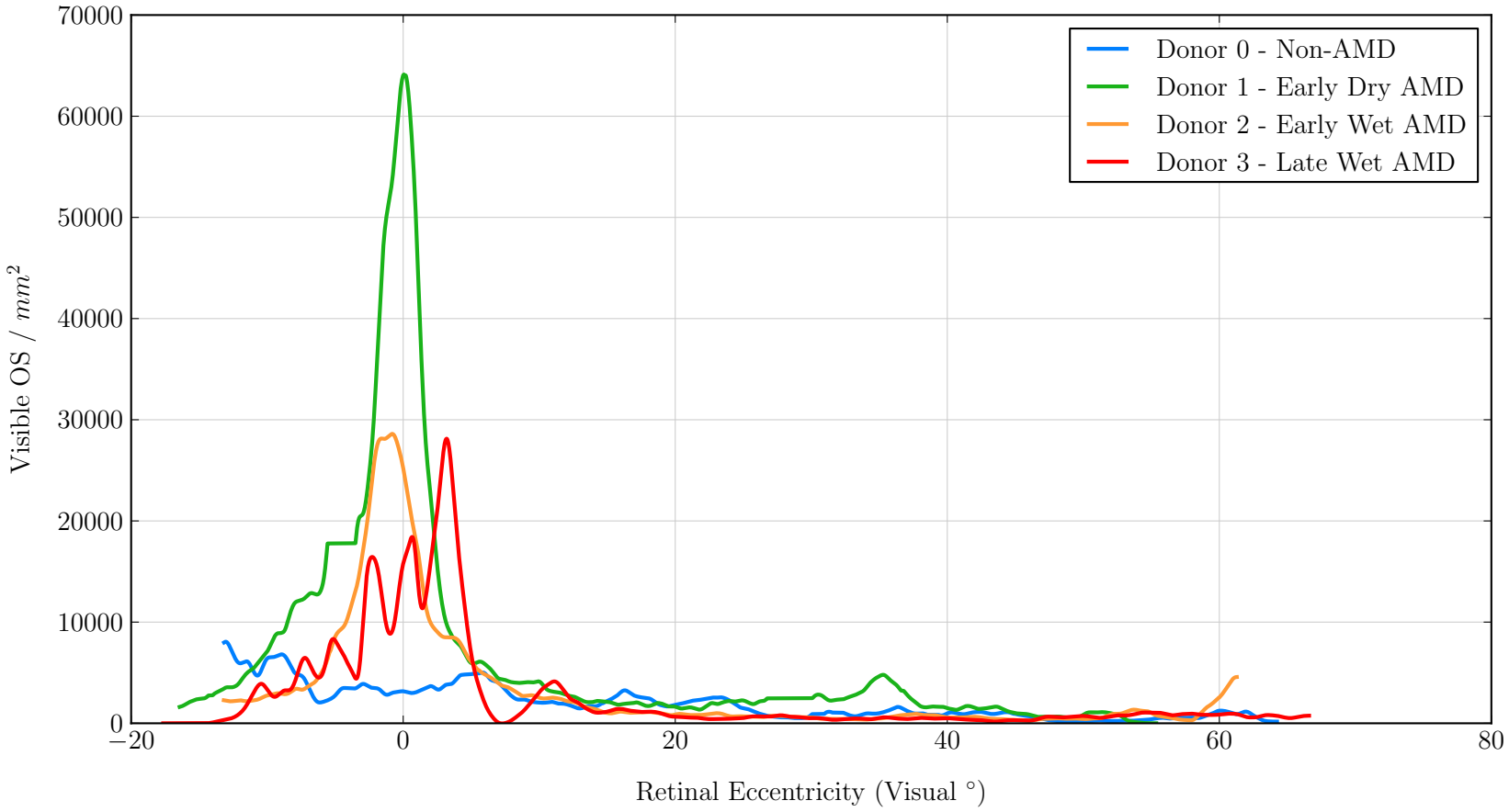

Figure 4.10: Numerical density profiles of visible cone inner segments per square millimeter as a function of retinal eccentricity. Profiles were generated using a 1mm boxcar and low-pass Butterworth filtered ($n = 2, \lambda = 1mm$).

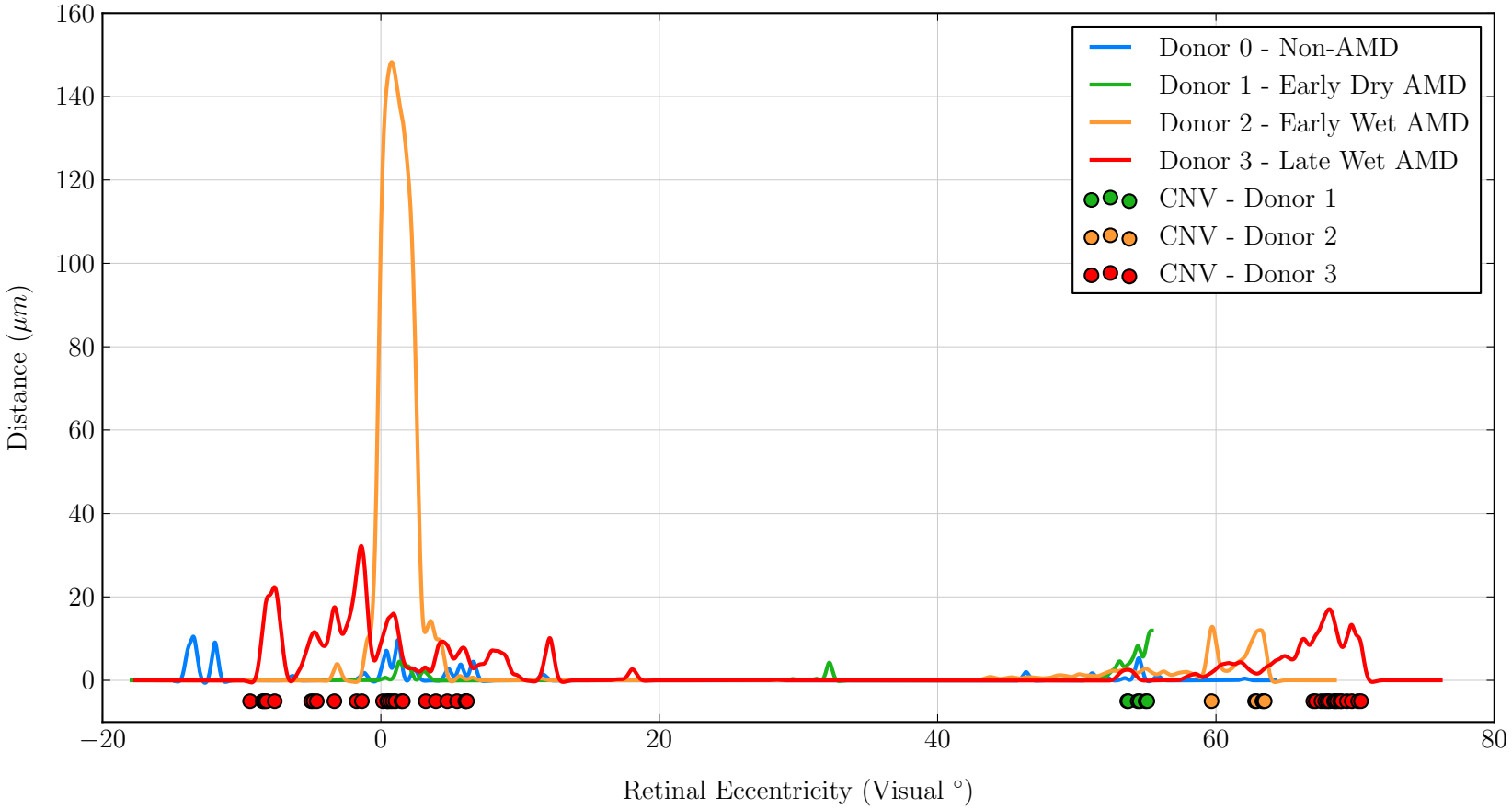

Figure 4.11: Profiles of the distance of separation between the basal surface of the RPE and the retinal side of Bruchs membrane as a function of retinal eccentricity. CNV lesions for each patient are plotted as circles below the curves. Profiles were generated using a 1mm boxcar and low-pass Butterworth filtered ($n = 2, \lambda = 1mm$).

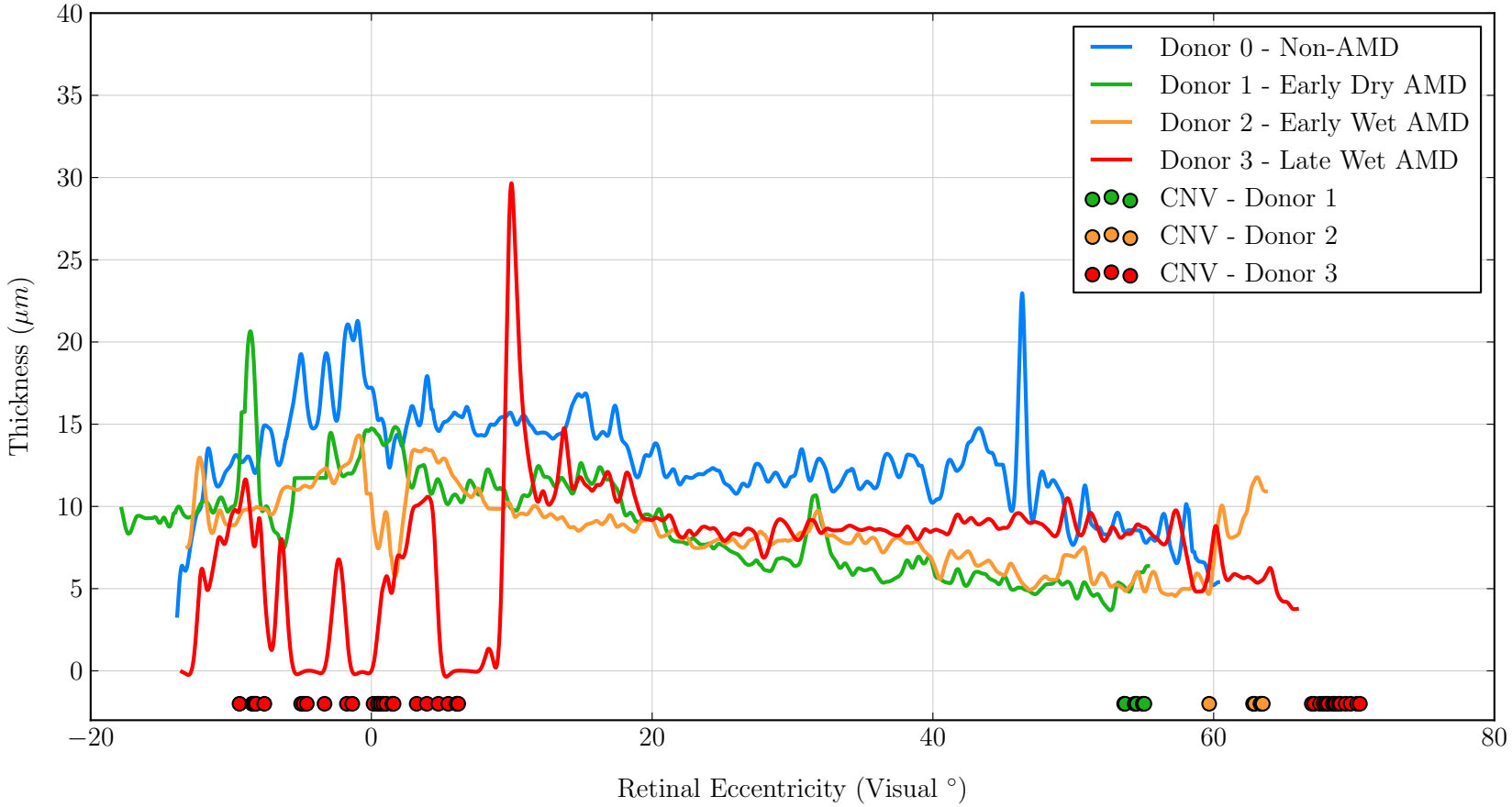

Figure 4.12: Profiles of the vertical thickness of the RPE cell layer as a function of retinal eccentricity. CNV lesions for each patient are plotted as circles below the curves. Profiles were generated using a 1mm boxcar and low-pass Butterworth filtered ($n = 2, \lambda = 1mm$).

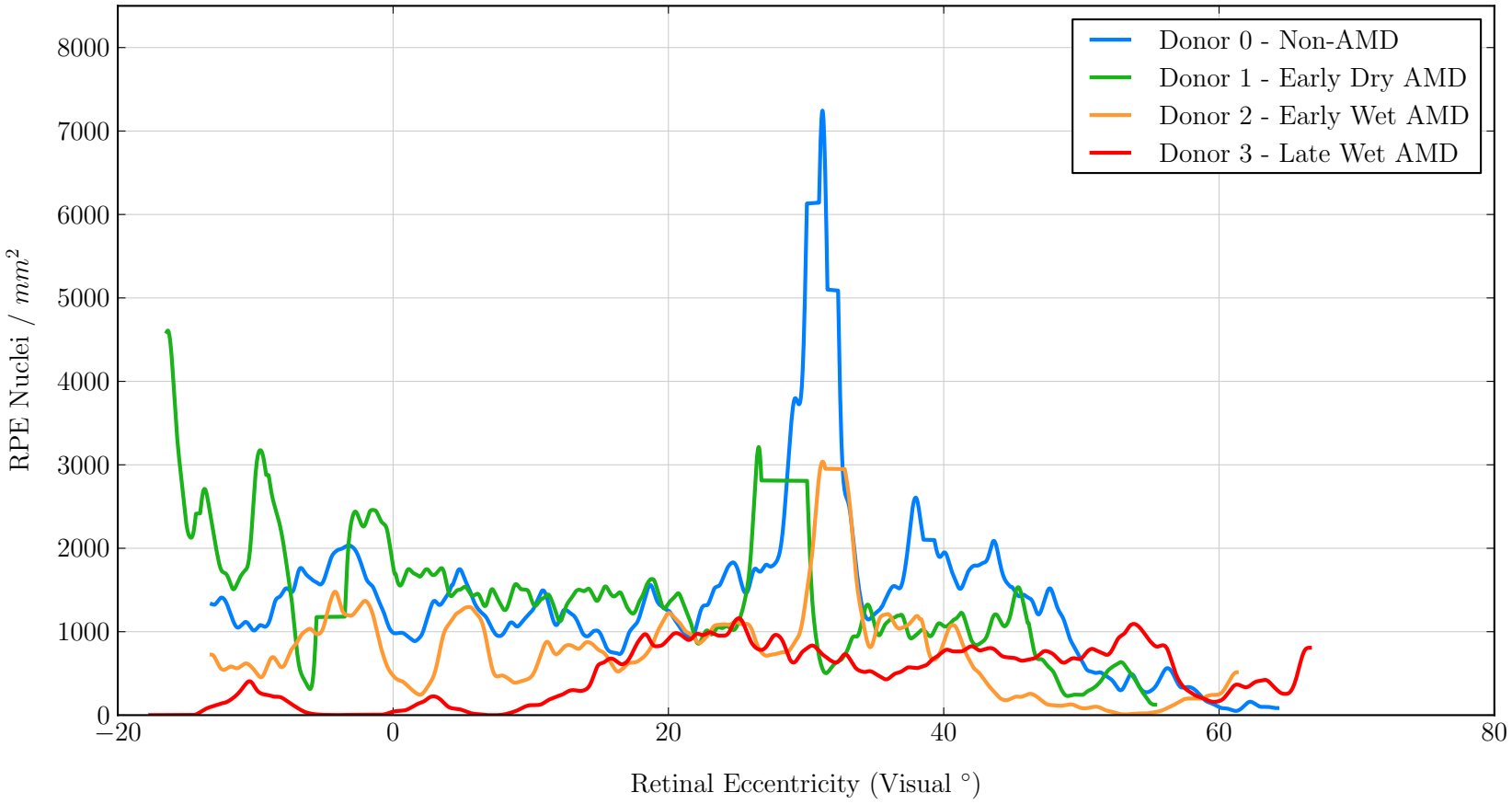

Figure 4.13: Profiles of the numerical density of RPE nuclei as a function of retinal eccentricity. Profiles were generated using a 1mm boxcar and low-pass Butterworth filtered ($n = 2, \lambda = 1mm$).

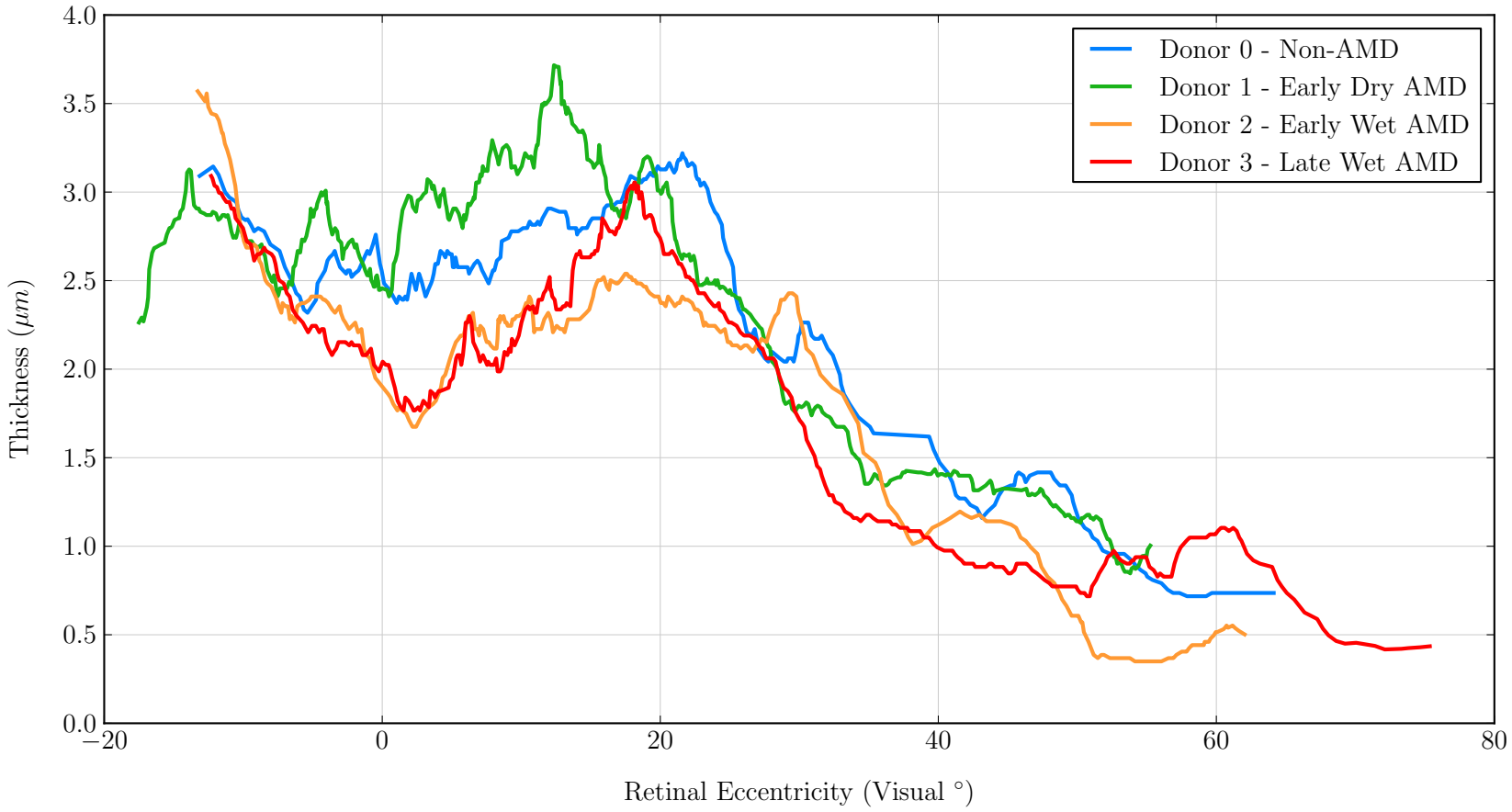

Figure 4.14: Profiles of the vertical thickness of Bruchs membrane as a function of retinal eccentricity. Profile signals have been processed with a mean filter using a boxcar of 20 measurements.

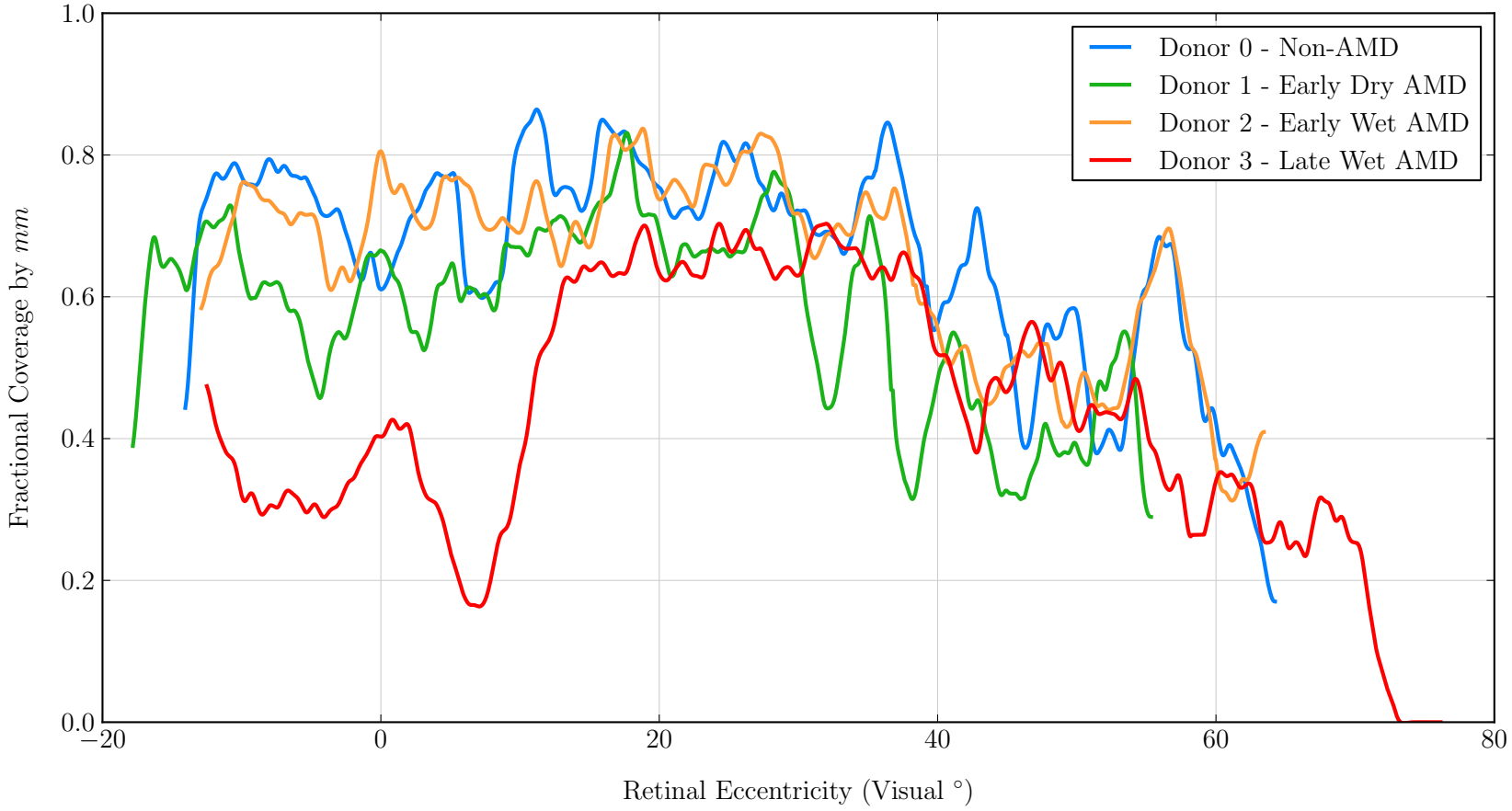

Figure 4.15: Profiles of the horizontal coverage factor of the choriocapillaris as a function of retinal eccentricity. Profiles were generated using a 1mm boxcar and low-pass Butterworth filtered ($n = 2, \lambda = 1mm$).

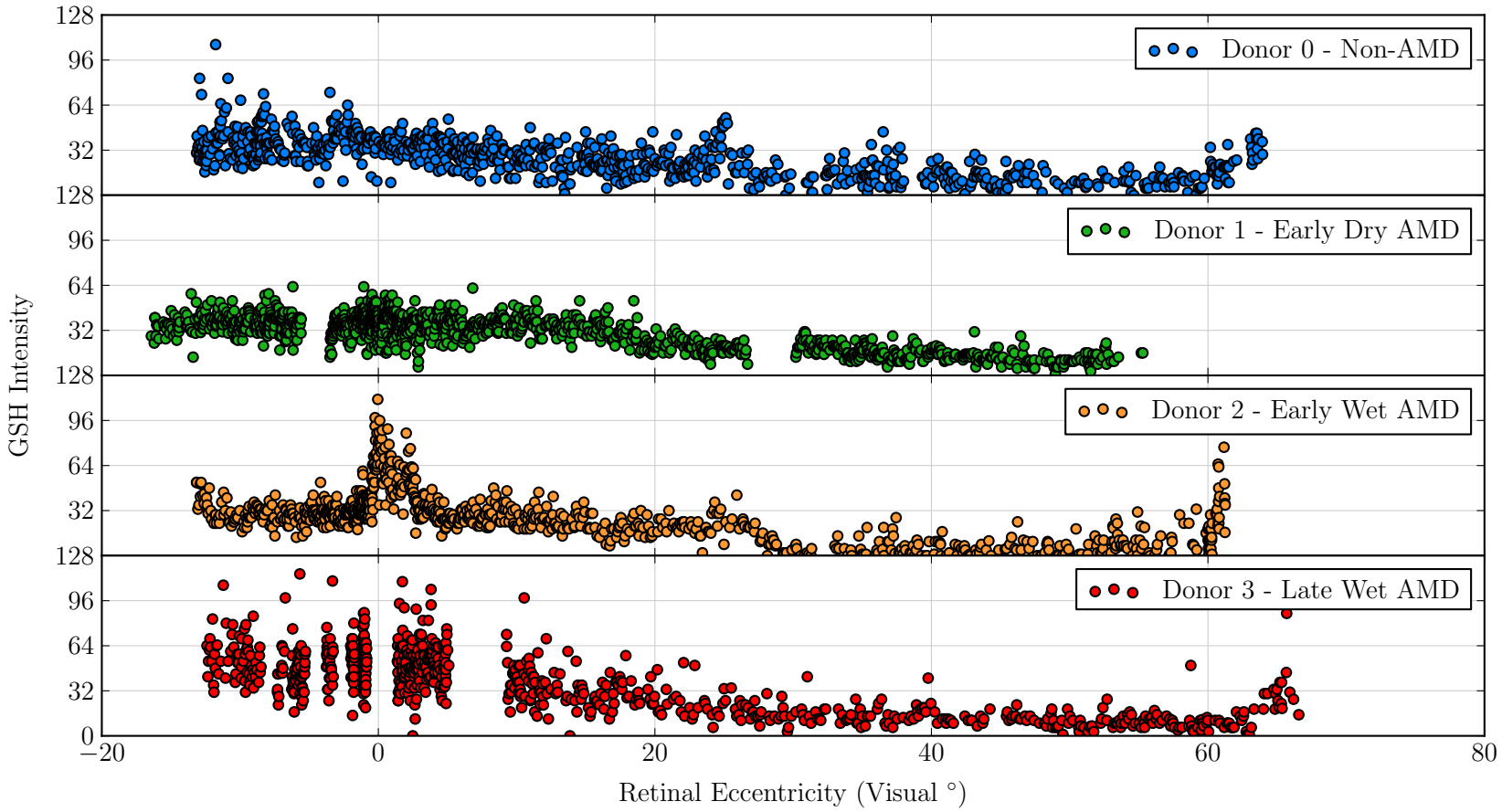

Figure 4.16: Cone inner segment glutathione distributions.

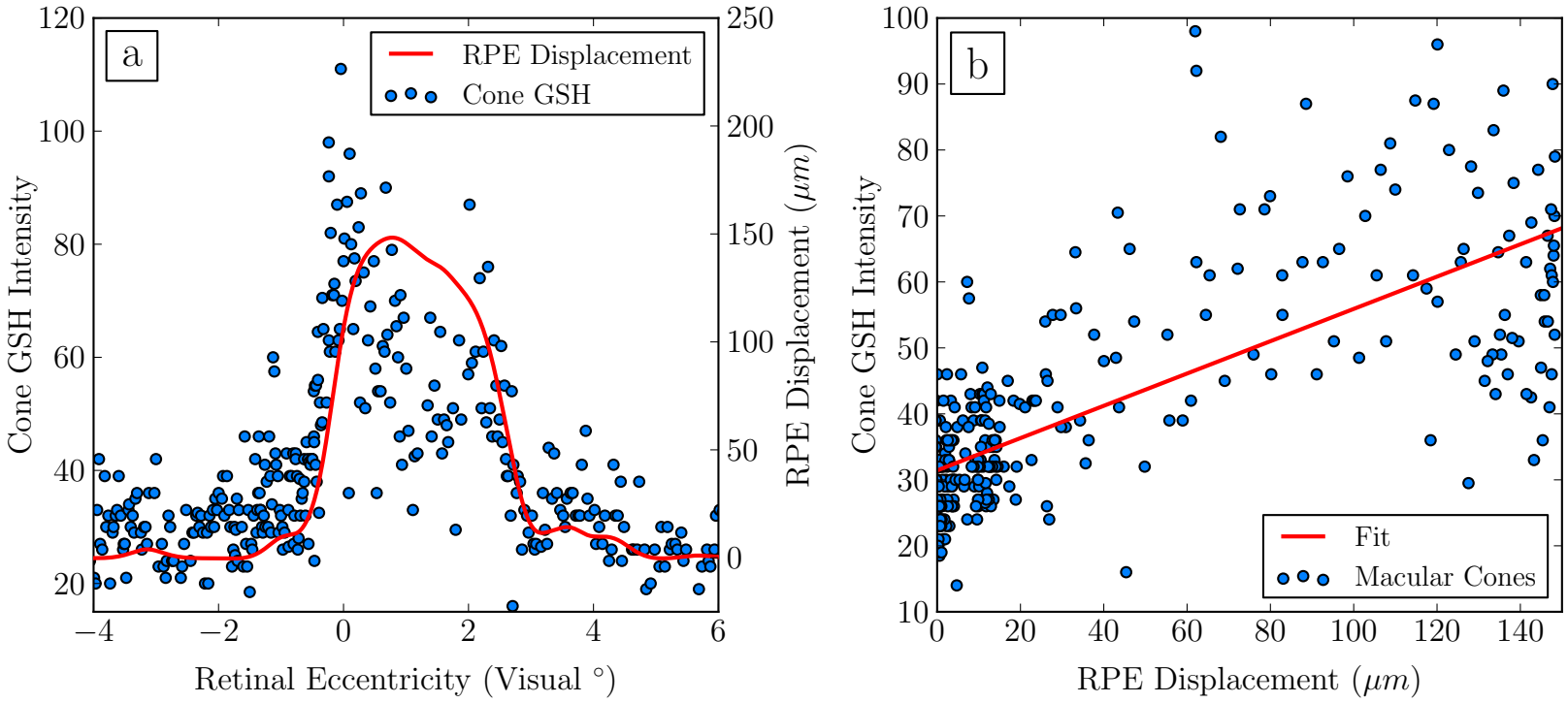

Figure 4.17: Cone glutathione vs RPE displacement in the fovea ($-1° \, to + 3°$) of donor 2.

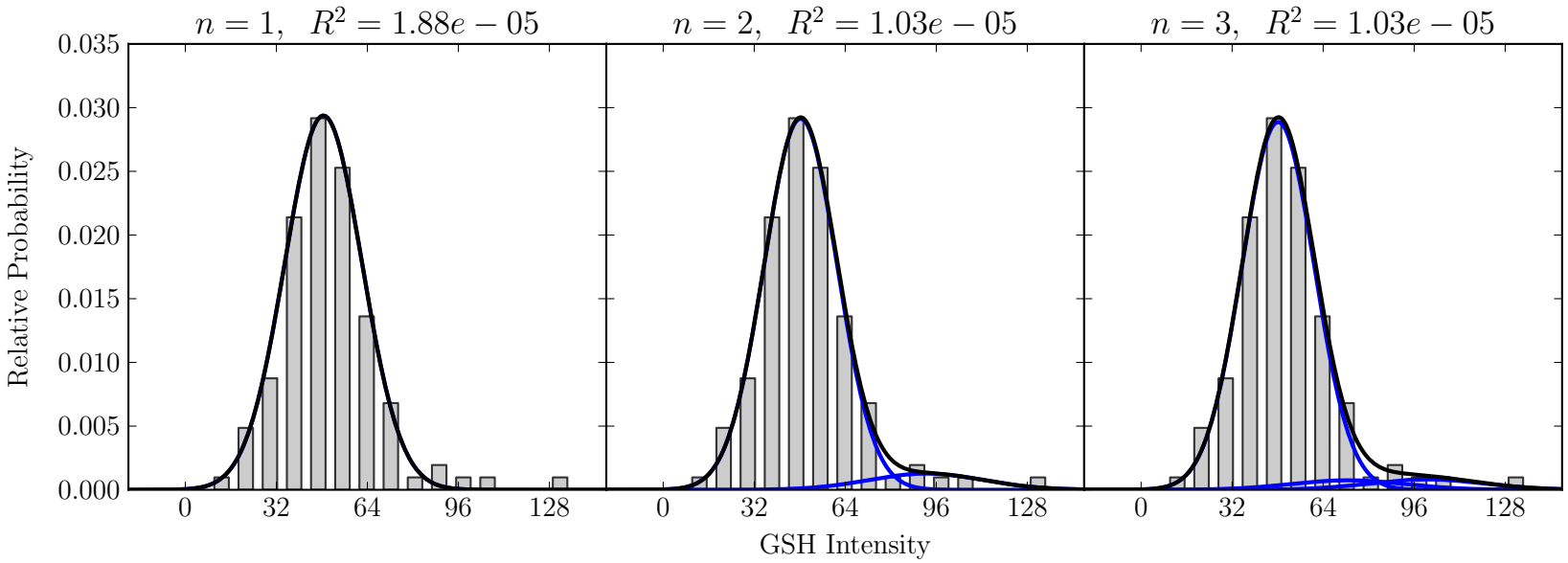

Figure 4.18: Cone glutathione population models for the fovea (-1° *to* $+3^\circ$) of donor 2.

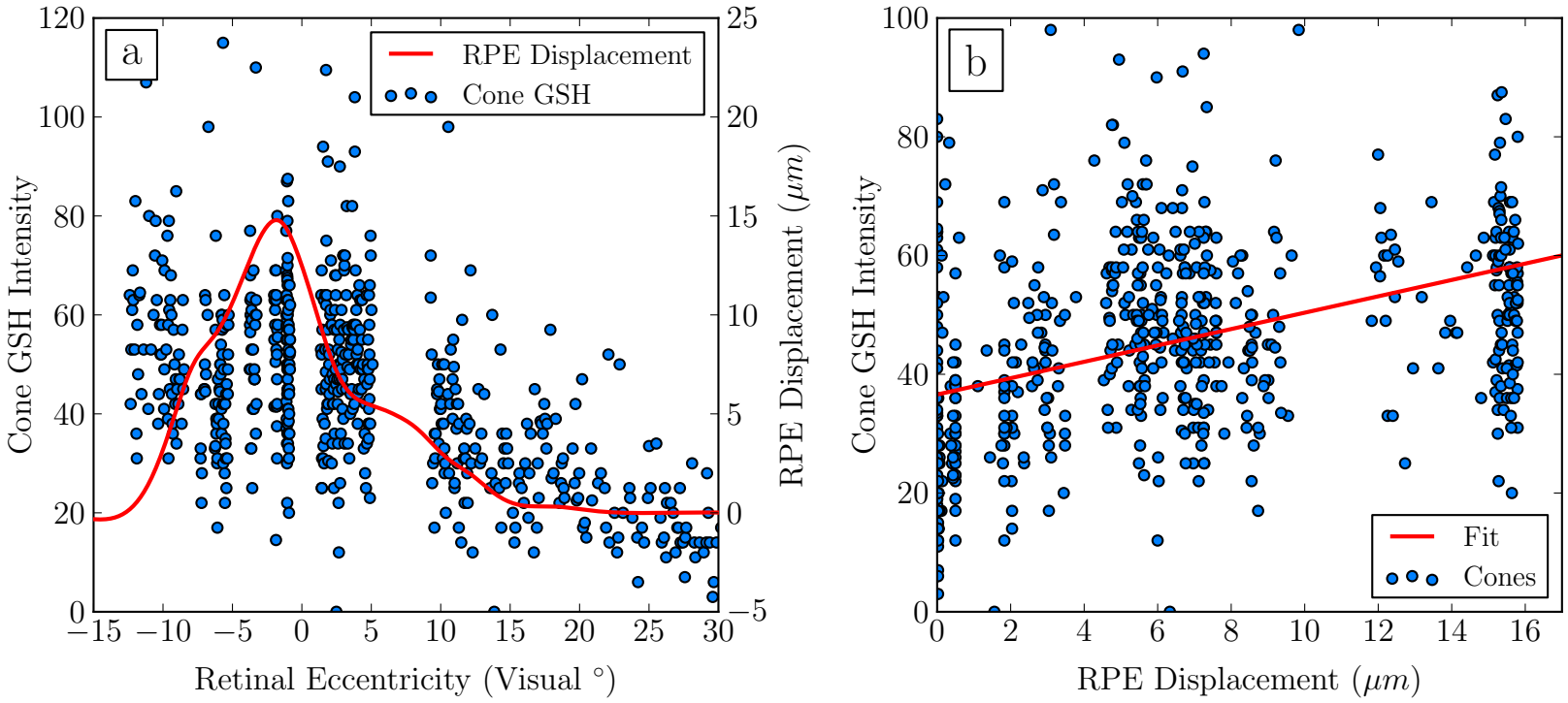

Figure 4.19: Cone glutathione vs RPE displacement in the macula ($-15° \, to + 30°$) of donor 3.

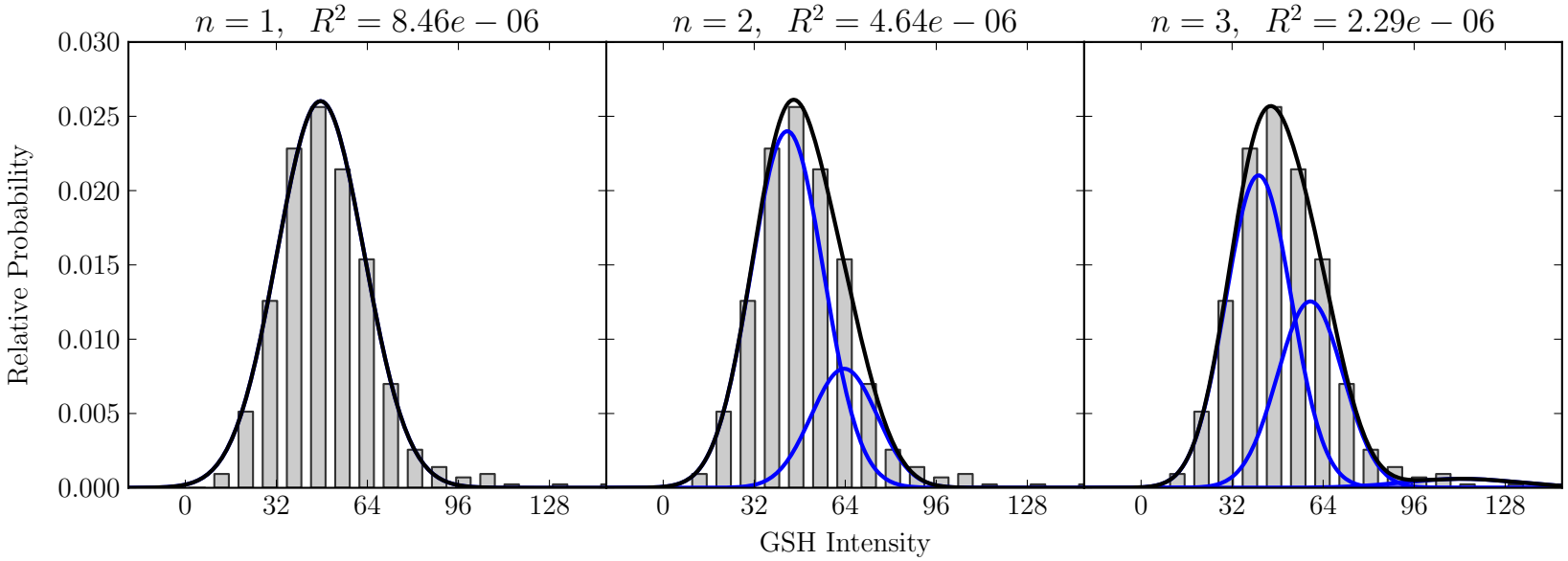

Figure 4.20: Cone glutathione population models for the central retina ($-15° \, to + 15°$) of donor 3.

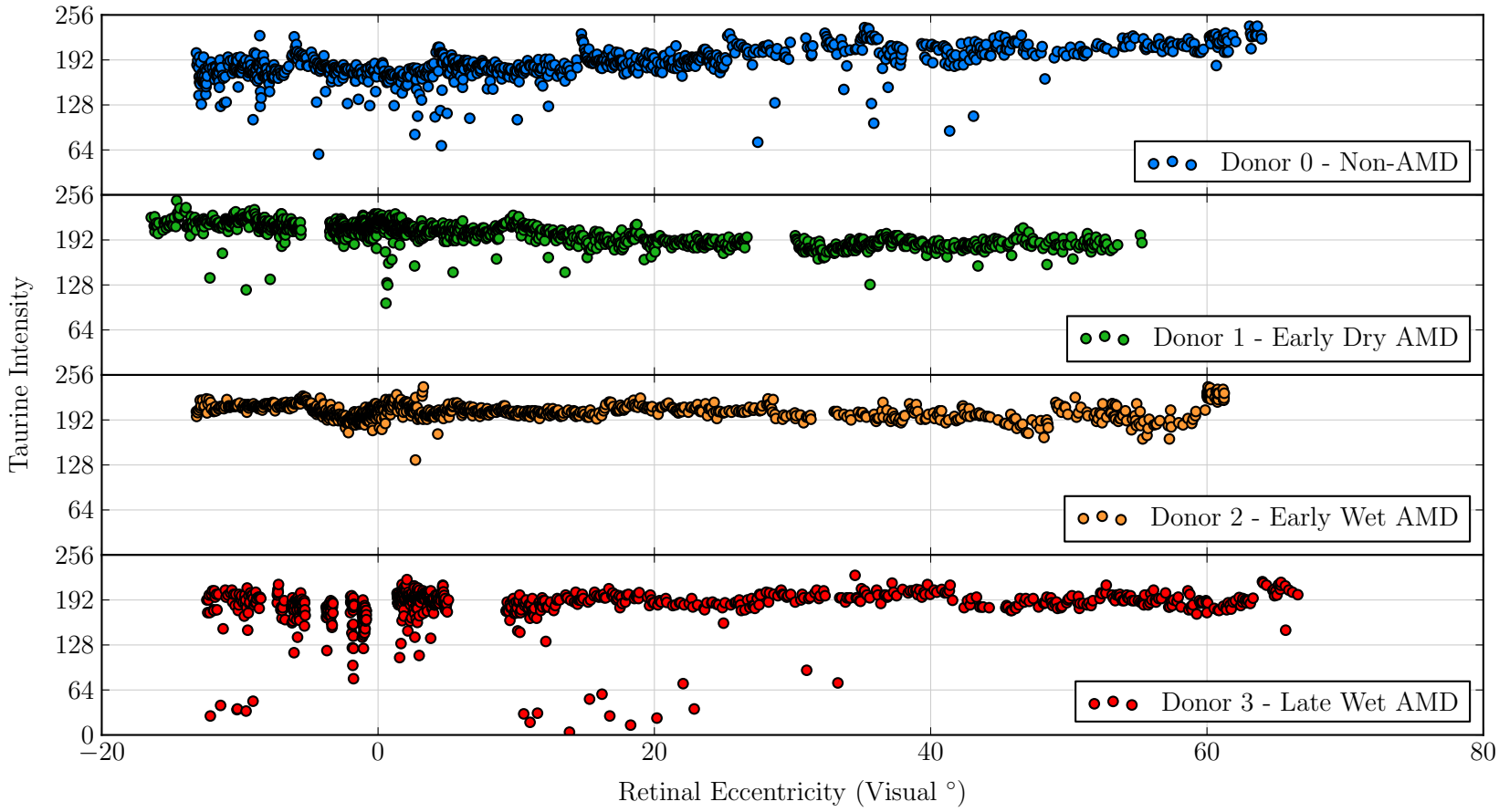

Figure 4.21: Cone inner segment taurine distributions. Profiles were generated using a 1mm boxcar and low-pass Butterworth filtered ($n = 2, \lambda = 1mm$).

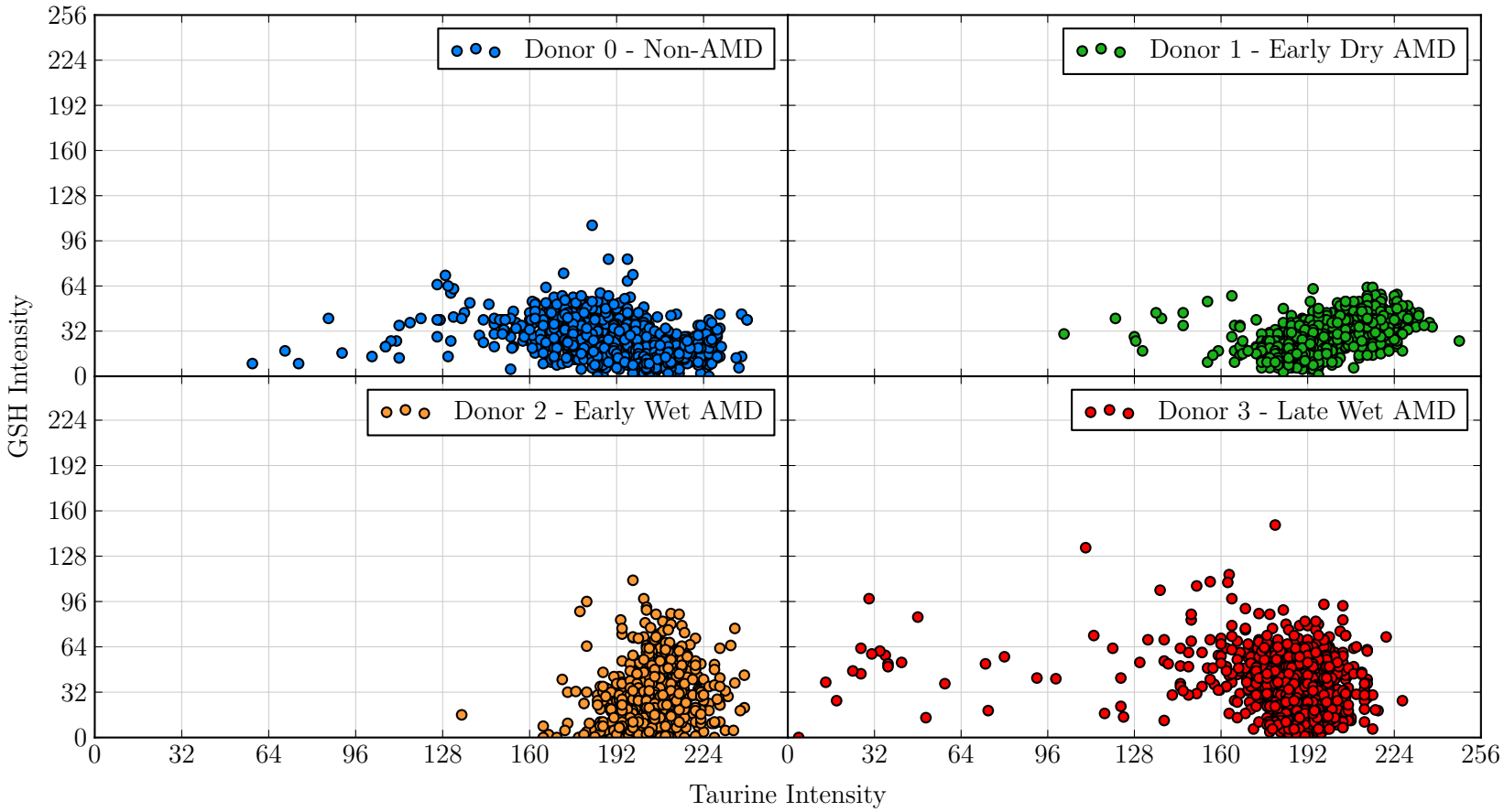

Figure 4.22: Cone glutathione / cone taurine bivariate distributions.

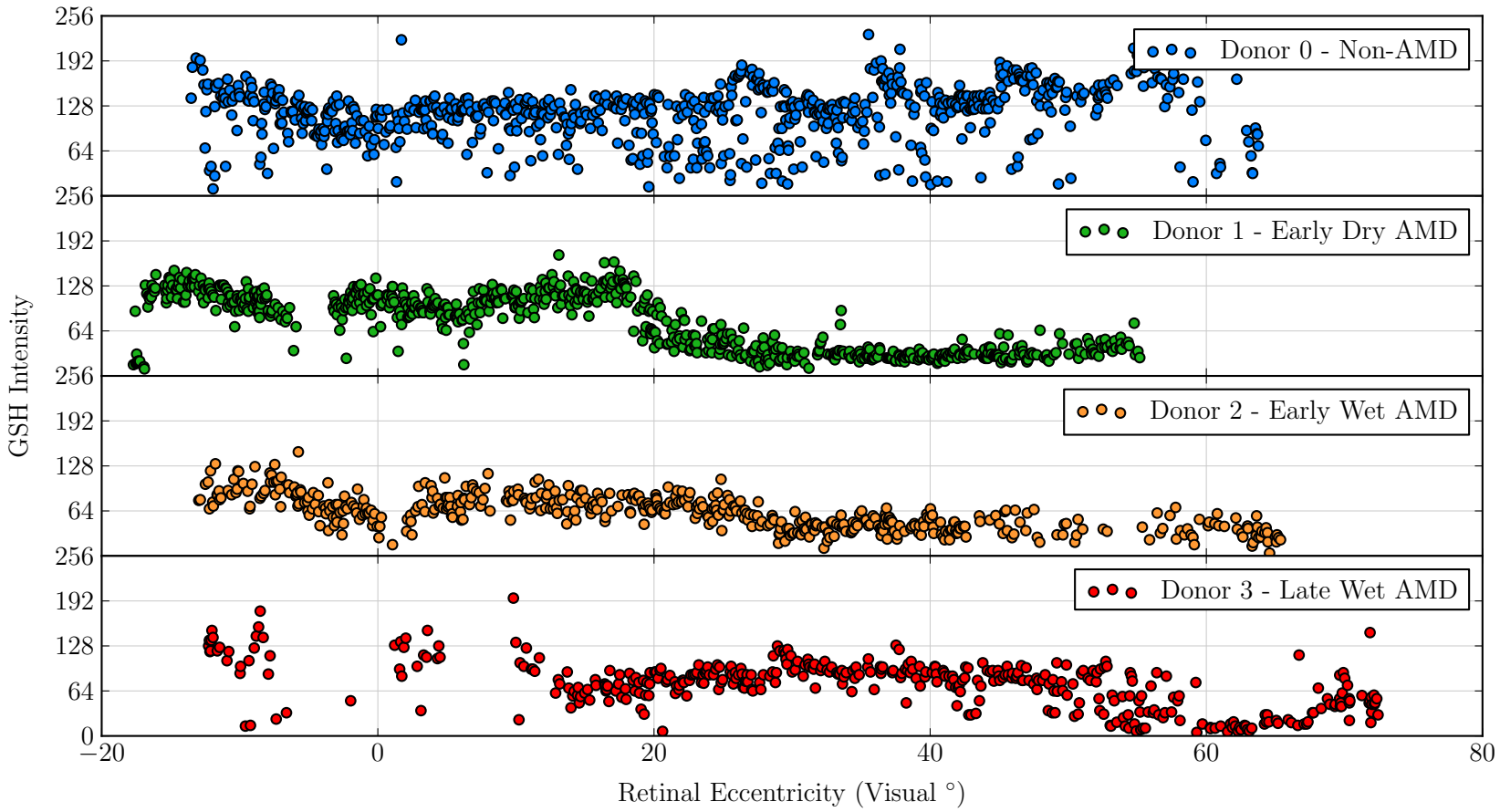

Figure 4.23: RPE nuclear glutathione distributions.

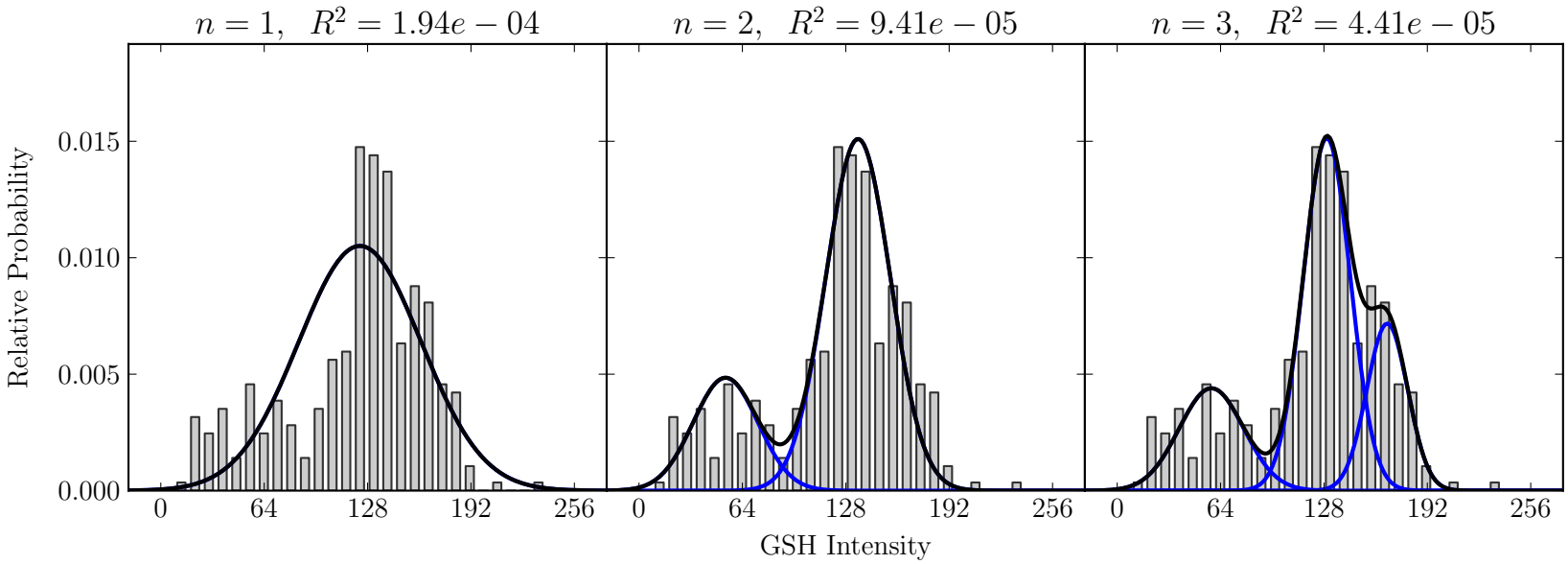

Figure 4.24: RPE glutathione population models for the midperipheral retina ($+20° \, to + 50°$) of donor 0.

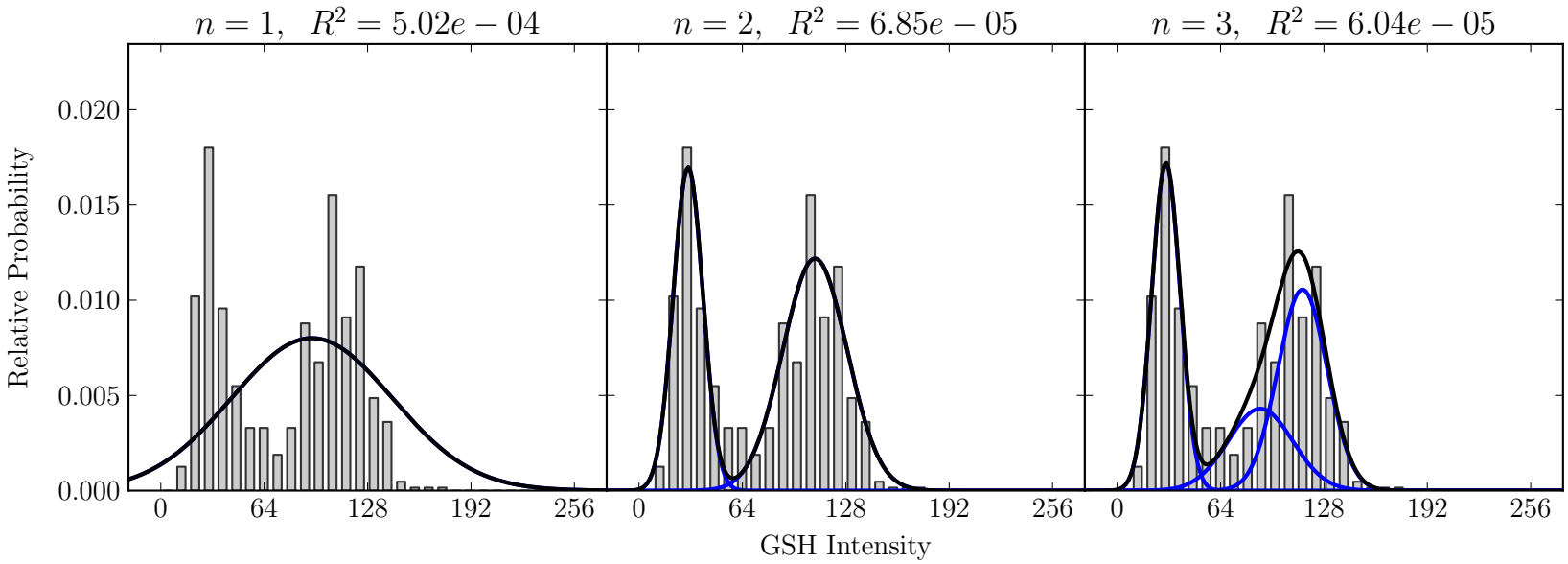

Figure 4.25: RPE glutathione population models for the full retina ($-20° \, to + 60°$) of donor 1.

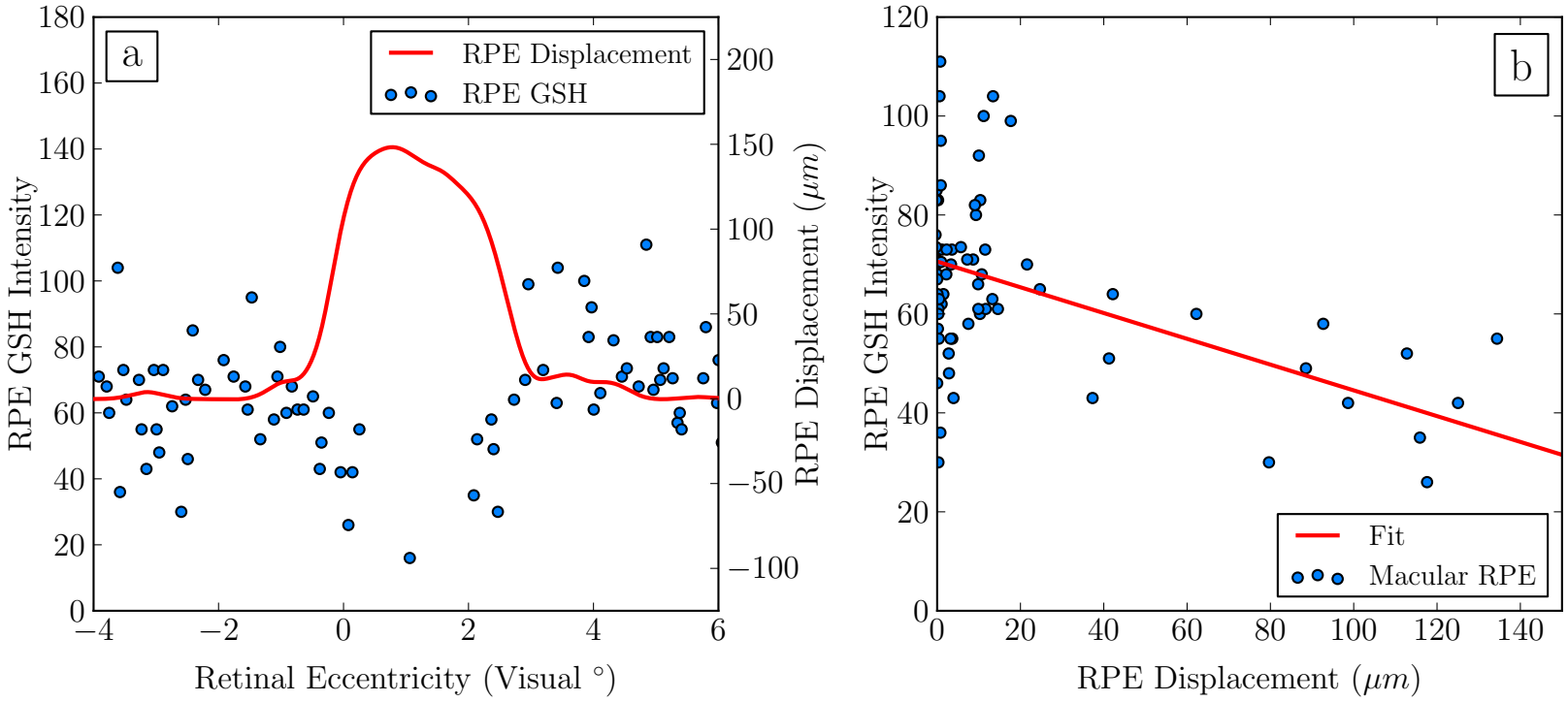

Figure 4.26: RPE glutathione vs RPE displacement in the fovea ($-1° \, to + 3°$) of donor 2.

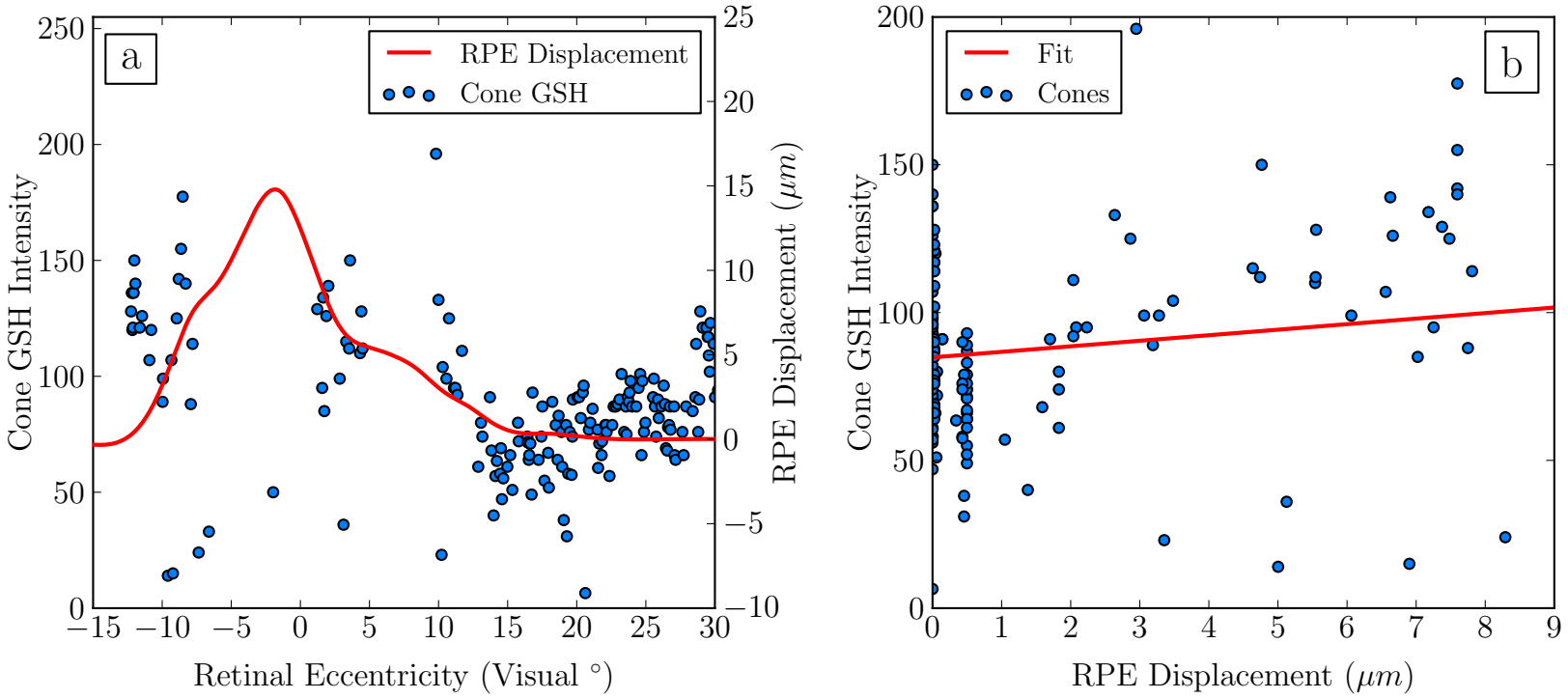

Figure 4.27: RPE glutathione vs RPE displacement in the central retina ($-15°$ *to* $+30°$) of donor 3.

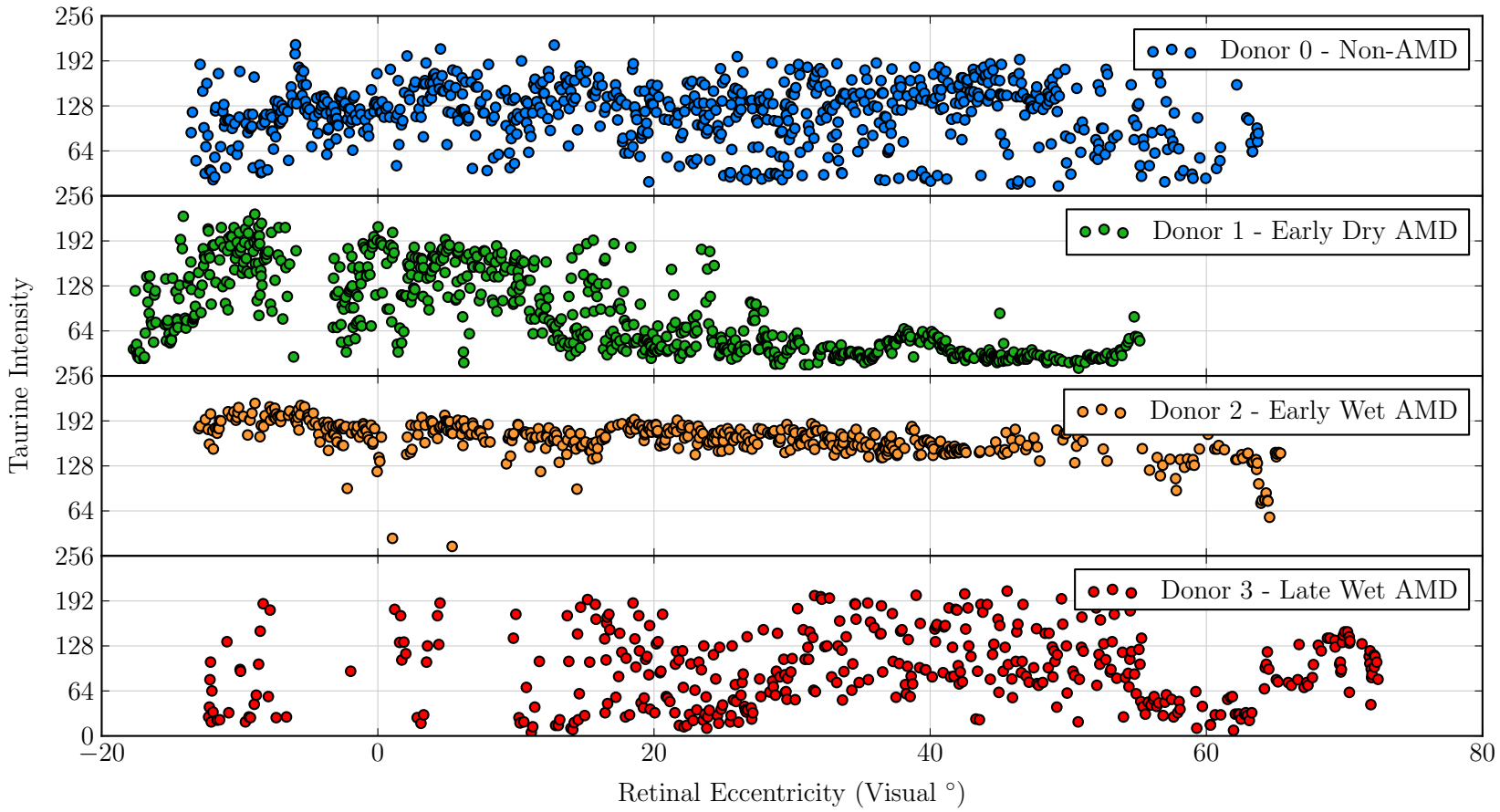

Figure 4.28: RPE nuclear taurine distributions.

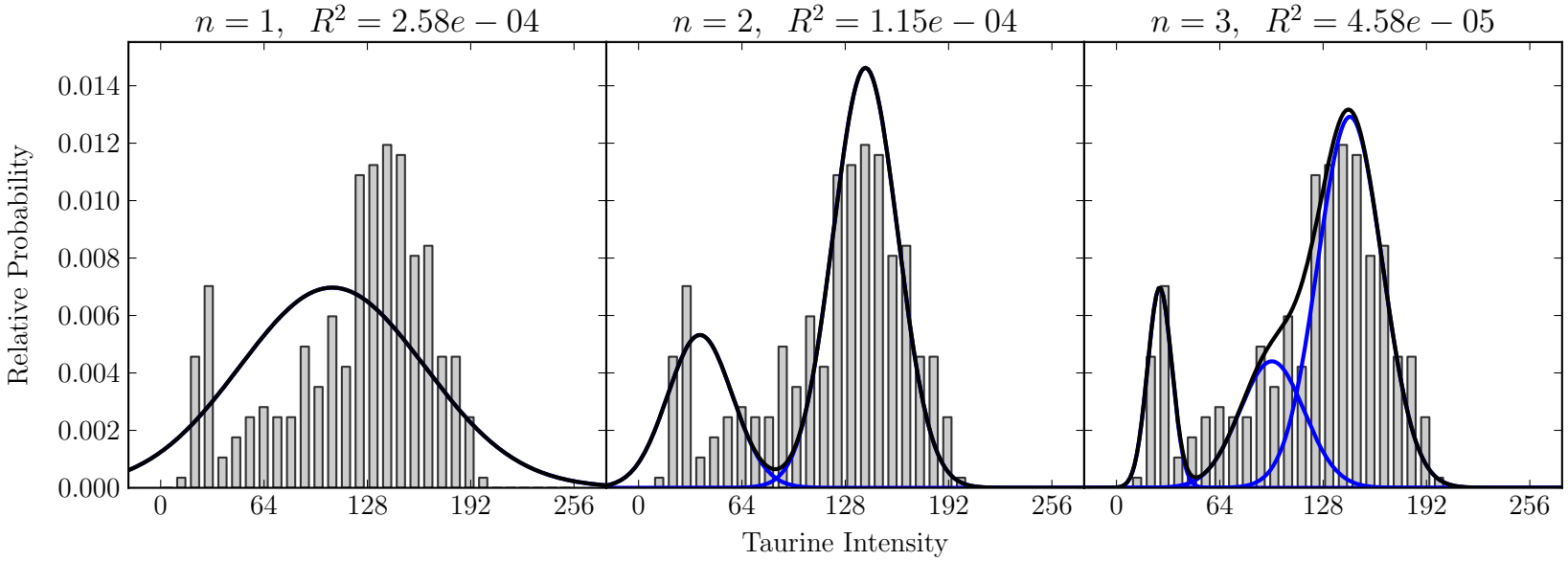

Figure 4.29: RPE taurine population models for the midperipheral retina ($+20° \, to + 50°$) of donor 0.

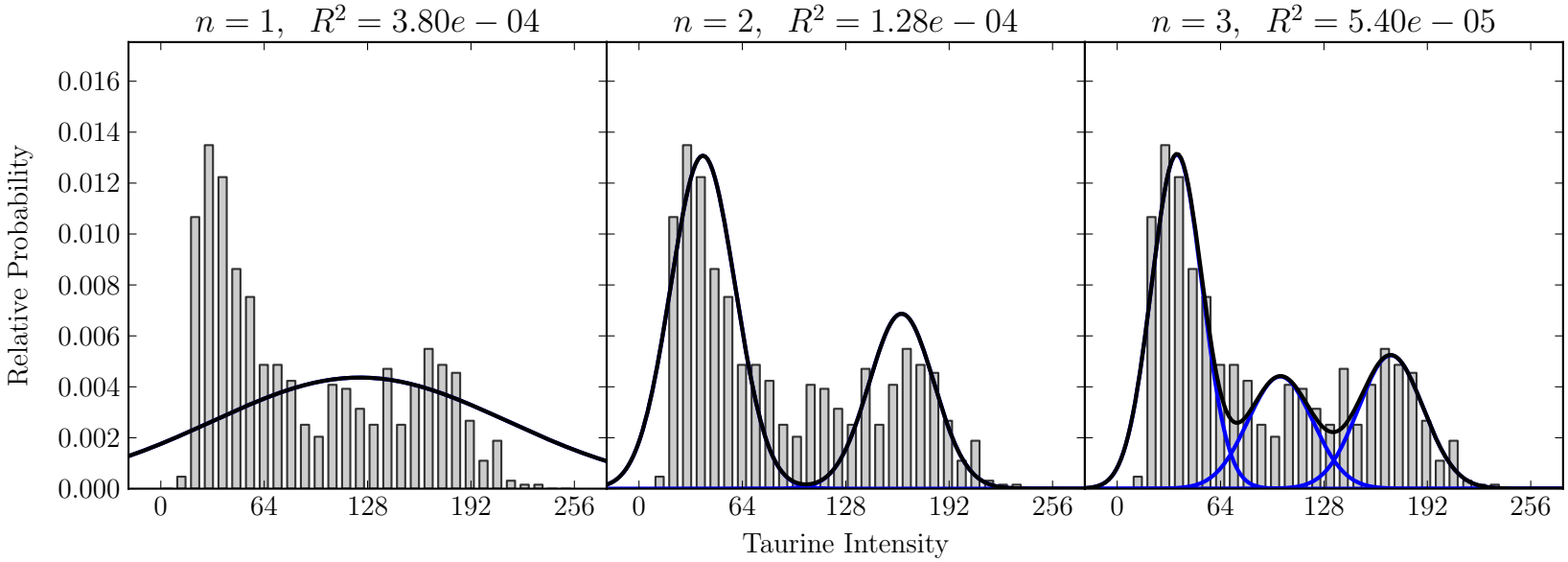

Figure 4.30: RPE taurine population models for the full retina ($-20° \, to + 60°$) of donor 1.

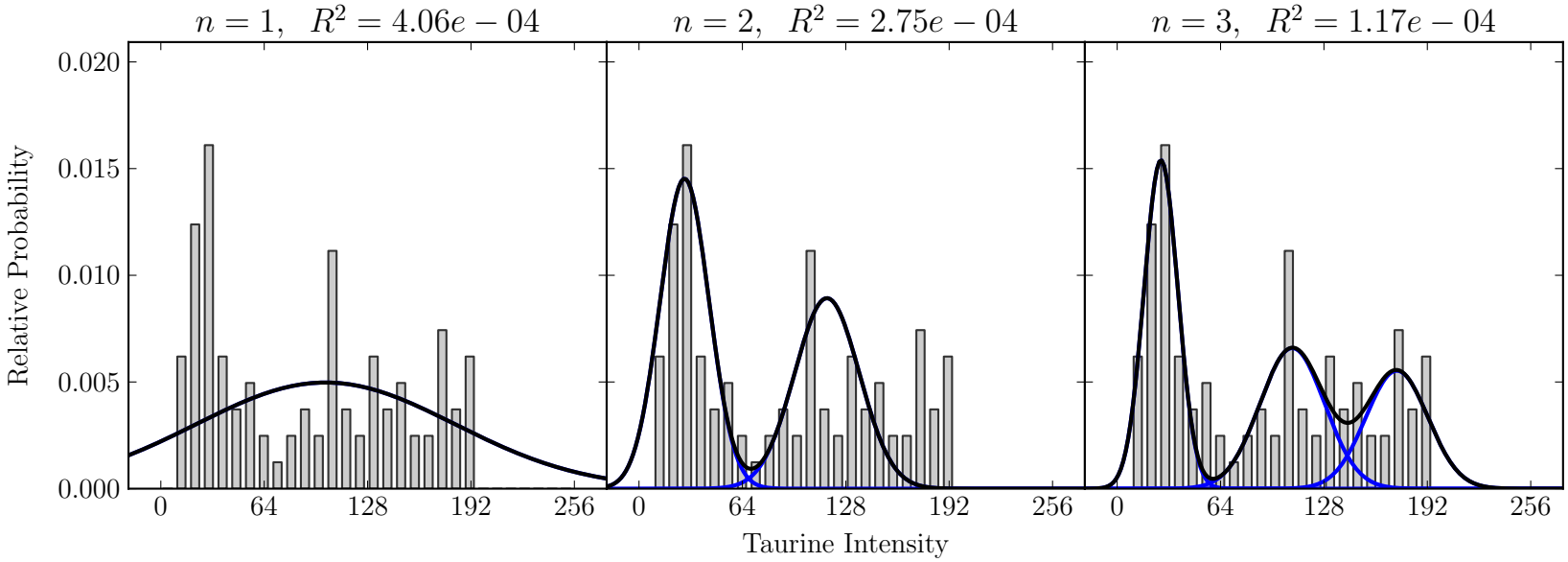

Figure 4.31: RPE taurine population models for the central retina ($-15° \, to + 20°$) of donor 3.

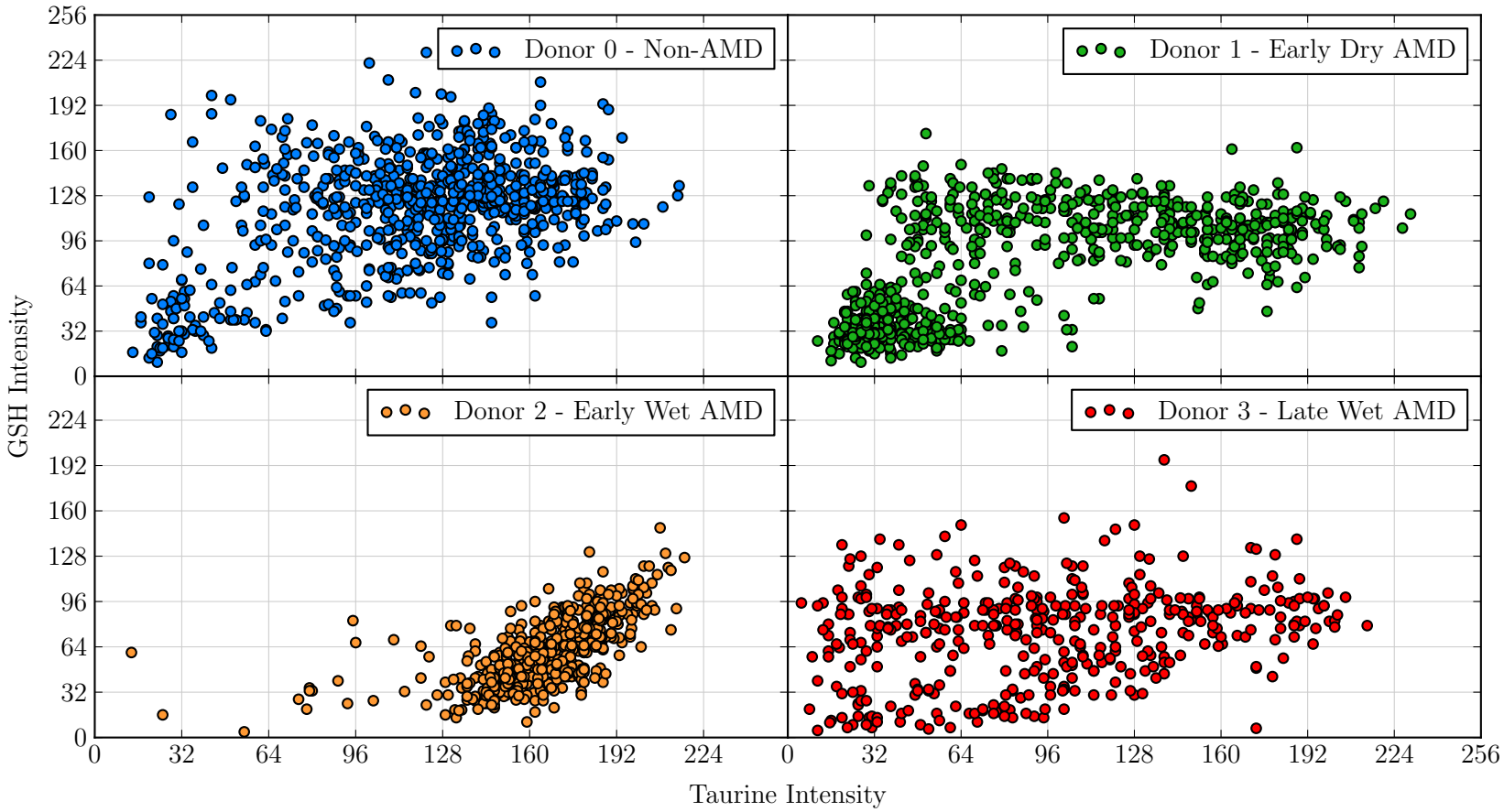

Figure 4.32: RPE glutathione / RPE taurine bivariate distributions.

REFERENCES

Allikmets, R., Singh, N., Shroyer, N. F., Hutchinson, A., Peiffer, A., Li, Y., Lewis, R. A., Leppert, M., Dean, M., and Lupski, J. R. (1997). A photoreceptor cell-specific ATP-binding transporter gene (ABCR) is mutated in recessive Stargardt macular dystrophy. *Nature Genetics*.

Amano, S., Kim, I., and Adamis, A. P. (1998). Advanced glycation end products increase retinal vascular endothelial growth factor expression. *The Journal of Clinical Investigation*.

Anderson, D. H., Radeke, M. J., Gallo, N. B., Chapin, E. A., Johnson, P. T., Curletti, C. R., Hancox, L. S., Hu, J., Ebright, J. N., Malek, G., Hauser, M. A., Rickman, C. B., Bok, D., Hageman, G. S., and Johnson, L. V. (2010). The pivotal role of the complement system in aging and age-related macular degeneration: hypothesis re-visited. *Progress in Retinal and Eye Research*.

Anderson, J. R., Jones, B. W., Yang, J.-H., Shaw, M. V., Watt, C. B., Koshevoy, P., Spaltenstein, J., Jurrus, E., U V, K., Whitaker, R. T., Mastronarde, D., Tasdizen, T., and Marc, R. E. (2009). A computational framework for ultrastructural mapping of neural circuitry. *PLoS Biology*.

Bird, A. C. (1991). Doyne Lecture. Pathogenesis of retinal pigment epithelial detachment in the elderly; the relevance of Bruch's membrane change. *Eye*.

Blaauwgeers, H. G., Holtkamp, G. M., Rutten, H., Witmer, A. N., Koolwijk, P., Partanen, T. A., Alitalo, K., Kroon, M. E., Kijlstra, A., van Hinsbergh, V. W., and Schlingemann, R. O. (1999). Polarized vascular endothelial growth factor secretion by human retinal pigment epithelium and localization of vascular endothelial growth factor receptors on the inner choriocapillaris. Evidence for a trophic paracrine relation. *The American Journal of Pathology*.

Boldyrev, A. A., Johnson, P., Wei, Y., Tan, Y., and Carpenter, D. O. (1999). Carnosine and taurine protect rat cerebellar granular cells from free radical damage. *Neuroscience Letters*.

Boltz, A., Luksch, A., Wimpissinger, B., Maar, N., Weigert, G., Frantal, S., Brannath, W., Garhöfer, G., Ergun, E., Stur, M., and Schmetterer, L. (2010). Choroidal blood flow and progression of age-related macular degeneration in the fellow eye in patients with unilateral choroidal neovascularization. *Investigative Ophthalmology & Visual Science*.

Boulton, M. (2008). Aging of the retinal pigment epithelium. *Visual Transduction and Non-Visual Light Perception*.

Burke, J. M. and Hjelmeland, L. M. (2005). Mosaicism of the retinal pigment epithelium: seeing the small picture. *Molecular Interventions*.

Cai, J., Nelson, K. C., Wu, M., Sternberg, P., and Jones, D. P. (2000). Oxidative damage and protection of the RPE. *Progress in Retinal and Eye Research*.

Chen, J., Fitzke, F., Pauleikhoff, D., and Bird, A. (1992). Functional loss in age-related Bruch's membrane change with choroidal perfusion defect. *Investigative Ophthalmology & Visual Science*.

Chong, N., Keonin, J., Luthert, P., Frennesson, C., Weingeist, D., Wolf, R., Mullins, R., and Hageman, G. (2005). Decreased thickness and integrity of the macular elastic layer of Bruch's membrane correspond to the distribution of lesions associated with age-related macular degeneration. *American Journal of Pathology*.

Ciulla, T., Harris, A., Kagemann, L., and Danis, R. (2002). Choroidal perfusion perturbations in non-neovascular age related macular degeneration. *The British Journal of Ophthalmology*.

Davidson, P. C., Sternberg, P., Jones, D. P., and Reed, R. L. (1994). Synthesis and transport of glutathione by cultured human retinal pigment epithelial cells. *Investigative Ophthalmology & Visual Science*.

de Jong, P. T. V. M. (2006). Age-related macular degeneration. *The New England Journal of Medicine*.

Delcourt, C., Cristol, J.-P., Léger, C. L., Descomps, B., and Papoz, L. (1999). Associations of antioxidant enzymes with cataract and age-related macular degeneration. *Ophthalmology*.

Dorey, C. K., Wu, G., Ebenstein, D., Garsd, A., and Weiter, J. J. (1989). Cell loss in the aging retina. Relationship to lipofuscin accumulation and macular degeneration. *Investigative Ophthalmology & Visual Science*.

Edwards, A., Ritter III, R., Abel, K., Manning, A., Panhuysen, C., and Farrer, L. (2005). Complement factor H polymorphism and age-related macular degeneration. *Science*.

El-Sherbeny, A., Naggar, H., Miyauchi, S., Ola, M. S., Maddox, D. M., Martin, P. M., Ganapathy, V., and Smith, S. B. (2004). Osmoregulation of taurine transporter function and expression in retinal pigment epithelial, ganglion, and müller cells. *Investigative Ophthalmology & Visual Science*.

Eldred, G. E. and Lasky, M. R. (1993). Retinal age pigments generated by self-assembling lysosomotropic detergents. *Nature*.

Feeney-Burns, L., Hilderbrand, E. S., and Eldridge, S. (1984). Aging human RPE: morphometric analysis of macular, equatorial, and peripheral cells. *Investigative Ophthalmology & Visual Science*.

Gao, H. and Hollyfield, J. G. (1992). Aging of the human retina. Differential loss of neurons and retinal pigment epithelial cells. *Investigative Ophthalmology & Visual Science*.

Güven, M., Görgün, E., Ünal, M., Yenerel, M., Batar, B., Küccümen, B., Dincc, U. A., Güven, G. S., Ulus, T., and Yüksel, A. (2011). Glutathione S-transferase M1, GSTT1 and GSTP1 genetic polymorphisms and the risk of age-related macular degeneration. *Ophthalmic Research*.

Guymer, R., Luthert, P., and Bird, A. (1999). Changes in Bruch's membrane and related structures with age. *Progress in Retinal and Eye Research*.

Ha, K.-N., Chen, Y., Cai, J., and Sternberg, P. (2006). Increased glutathione synthesis through an ARE-Nrf2-dependent pathway by zinc in the RPE: implication for protection against oxidative stress. *Investigative Ophthalmology & Visual Science*.

Hageman, G. S., Anderson, D. H., Johnson, L. V., Hancox, L. S., Taiber, A. J., Hardisty, L. I., Hageman, J. L., Stockman, H. A., Borchardt, J. D., Gehrs, K. M., Smith, R. J. H., Silvestri, G., Russell, S. R., Klaver, C. C. W., Barbazetto, I., Chang, S., Yannuzzi, L. A., Barile, G. R., Merriam, J. C., Olsh, A. K., Bergeron, J., Zernant, J., Merriam, J. E., Gold, B., Dean, M., and Allikmets, R. (2005). A common haplotype in the complement regulatory gene factor H (HF1/CFH) predisposes individuals to age-related macular degeneration. *Proceedings of the National Academy of Sciences*.

Haines, J., Hauser, M., Schmidt, S., Scott, W., Olson, L., Gallins, P., Spencer, K., Kwan, S., Noureddine, M., and Gilbert, J. (2005). Complement factor H variant increases the risk of age-related macular degeneration. *Science*.

Handa, J. T., Verzijl, N., Matsunaga, H., Aotaki-Keen, A., Lutty, G. A., te Koppele, J. M., Miyata, T., and Hjelmeland, L. M. (1999). Increase in the advanced glycation end product pentosidine in Bruch's membrane with age. *Investigative Ophthalmology & Visual Science*.

Hayes, K. C., Carey, R. E., and Schmidt, S. Y. (1975). Retinal degeneration associated with taurine deficiency in the cat. *Science*.

Heller-Stilb, B., van Roeyen, C., Rascher, K., Hartwig, H.-G., Huth, A., Seeliger, M. W., Warskulat, U., and Häussinger, D. (2002). Disruption of the taurine transporter gene (taut) leads to retinal degeneration in mice. *The FASEB Journal*.

Howes, K. A., Liu, Y., Dunaief, J. L., Milam, A., Frederick, J. M., Marks, A., and Baehr, W. (2004). Receptor for advanced glycation end products and age-related macular degeneration. *Investigative Ophthalmology & Visual Science*.

Huxtable, R. J. (1992). Physiological actions of taurine. *Physiological Reviews*.

Jones, B. W. and Marc, R. E. (2005). Retinal remodeling during retinal degeneration. *Experimental Eye Research*.

Junyent, F., Utrera, J., Camins, A., Pallàs, M., Romero, R., and Auladell, C. (2009). Synthesis, uptake and release of taurine in astrocytes treated with 8-Br-cAMP. *Neuroscience Letters*.

Kalloniatis, M., Marc, R. E., and Murry, R. F. (1996). Amino acid signatures in the primate retina. *The Journal of Neuroscience*.

Kannan, R., Tang, D., Hu, J., and Bok, D. (2001). Glutathione transport in human retinal pigment epithelial (HRPE) cells: apical localization of sodium-dependent gsh transport. *Experimental Eye Research*.

Keys, S. A. and Zimmerman, W. F. (1999). Antioxidant activity of retinol, glutathione, and taurine in bovine photoreceptor cell membranes. *Experimental Eye Research*.

Kim, I., Ryan, A. M., Rohan, R., Amano, S., Agular, S., Miller, J. W., and Adamis, A. P. (1999). Constitutive expression of VEGF, VEGFR-1, and VEGFR-2 in normal eyes. *Investigative Ophthalmology & Visual Science*.

Klein, R. J., Zeiss, C., Chew, E. Y., Tsai, J.-Y., Sackler, R. S., Haynes, C., Henning, A. K., SanGiovanni, J. P., Mane, S. M., Mayne, S. T., Bracken, M. B., Ferris, F. L., Ott, J., Barnstable, C., and Hoh, J. (2005). Complement factor H polymorphism in age-related macular degeneration. *Science*.

Korte, G. E., Reppucci, V., and Henkind, P. (1984). RPE destruction causes choriocapillary atrophy. *Investigative Ophthalmology & Visual Science*.

Kraft, D. (1997). Algorithm 733: TOMP — Fortran Modules for Optimal Control Calculations. *ACM Transactions on Mathematical Software*.

Lu, S. C., Sun, W. M., Nagineni, C. N., Hooks, J. J., and Kannan, R. (1995). Bidirectional glutathione transport by cultured human retinal pigment epithelial cells. *Investigative Ophthalmology & Visual Science*.

Ma, W., Lee, S. E., Guo, J., Qu, W., Hudson, B. I., Schmidt, A. M., and Barile, G. R. (2007). RAGE ligand upregulation of VEGF secretion in ARPE-19 cells. *Investigative Ophthalmology & Visual Science*.

Marc, R. E. and Jones, B. W. (2002). Molecular phenotyping of retinal ganglion cells. *The Journal of Neuroscience*.

Marc, R. E., Jones, B. W., Anderson, J. R., Kinard, K., Marshak, D. W., Wilson, J. H., Wensel, T., and Lucas, R. J. (2007). Neural reprogramming in retinal degeneration. *Investigative Ophthalmology & Visual Science*.

Marc, R. E., Murry, R. F., and Basinger, S. F. (1995). Pattern recognition of amino acid signatures in retinal neurons. *The Journal of Neuroscience*.

Marc, R. E., Stell, W. K., Bok, D., and LAM, D. M. K. (1978). GABA-ergic pathways in the goldfish retina. *The Journal of Comparative Neurology*.

McLeod, D. S., Grebe, R., Bhutto, I., Merges, C., Baba, T., and Lutty, G. A. (2009). Relationship between RPE and choriocapillaris in age-related macular degeneration. *Investigative Ophthalmology & Visual Science*.

McLeod, D. S., Taomoto, M., Otsuji, T., Green, W. R., Sunness, J. S., and Lutty, G. A. (2002). Quantifying changes in RPE and choroidal vasculature in eyes with age-related macular degeneration. *Investigative Ophthalmology & Visual Science*.

Militante, J. and Lombardini, J. B. (2004). Age-related retinal degeneration in animal models of aging: possible involvement of taurine deficiency and oxidative stress. *Neurochemical Research*.

Muller, J. F. and Marc, R. E. (1990). GABA-ergic and glycinergic pathways in the inner plexiform layer of the goldfish retina. *The Journal of Comparative Neurology*.

Nowak, M., Swietochowska, E., Wielkoszyński, T., Marek, B., Karpe, J., Górski, J., Głogowska-Szelag, J., Kos-Kudła, B., and Ostrowska, Z. (2003). Changes in blood antioxidants and several lipid peroxidation products in women with age-related macular degeneration. *European Journal of Ophthalmology*.

Ogino, N., Matsumura, M., Shirakawa, H., and Tsukahara, I. (1983). Phagocytic activity of cultured retinal pigment epithelial cells from chick embryo: inhibition by melatonin and cyclic AMP, and its reversal by taurine and cyclic GMP. *Ophthalmic Research*.

Pasantes-Morales, H., Ochoa de la Paz, L. D., Sepúlveda, J., and Quesada, O. (1999). Amino acids as osmolytes in the retina. *Neurochemical Research*.

Pauleikhoff, D., Spital, G., and Radermacher, M. (1999). A fluorescein and indocyanine green angiographic study of choriocapillaris in age-related macular disease. *Archives of Ophthalmology*.

Pow, D. V. and Crook, D. K. (1994). Rapid postmortem changes in the cellular localisation of amino acid transmitters in the retina as assessed by immunocytochemistry. *Brain Research*.

Provis, J. M., Penfold, P. L., Cornish, E. E., Sandercoe, T. M., and Madigan, M. C. (2005). Anatomy and development of the macula: specialisation and the vulnerability to macular degeneration. *Clinical & Experimental Optometry*.

Radu, R. A., Mata, N. L., Nusinowitz, S., Liu, X., Sieving, P. A., and Travis, G. H. (2003). Treatment with isotretinoin inhibits lipofuscin accumulation in a mouse model of recessive Stargardt's macular degeneration. *Proceedings of the National Academy of Sciences*.

Ramrattan, R. S., van der Schaft, T. L., Mooy, C. M., de Bruijn, W. C., Mulder, P. G., and de Jong, P. T. (1994). Morphometric analysis of Bruch's membrane, the choriocapillaris, and the choroid in aging. *Investigative Ophthalmology & Visual Science*.

Riederer, P., Sofic, E., Rausch, W. D., Schmidt, B., Reynolds, G. P., Jellinger, K., and Youdim, M. B. (1989). Transition metals, ferritin, glutathione, and ascorbic acid in parkinsonian brains. *Journal of Neurochemistry*.

Samiec, P. S., Drews-Botsch, C., Flagg, E. W., Kurtz, J. C., Sternberg, P., Reed, R. L., and Jones, D. P. (1998). Glutathione in human plasma: decline in association with aging, age-related macular degeneration, and diabetes. *Free Radical Biology & Medicine*.

Schmidt, S. Y., Berson, E. L., and Hayes, K. C. (1976). Retinal degeneration in cats fed casein. I. Taurine deficiency. *Investigative Ophthalmology*.

Schulz, J. B., Lindenau, J., Seyfried, J., and Dichgans, J. (2000). Glutathione, oxidative stress and neurodegeneration. *European Journal of Biochemistry*.

Sparrow, J. R., Zhou, J., Ben-Shabat, S., Vollmer, H., Itagaki, Y., and Nakanishi, K. (2002). Involvement of oxidative mechanisms in blue-light-induced damage to A2E-laden RPE. *Investigative Ophthalmology & Visual Science*.

Spraul, C. W., Lang, G. E., and Grossniklaus, H. E. (1996). Morphometric analysis of the choroid, Bruch's membrane, and retinal pigment epithelium in eyes with age-related macular degeneration. *Investigative Ophthalmology & Visual Science*.

Stargardt, K. (1909). Über familiäre, progressive Degeneration in der Maculagegend des Auges. *Gräfes Arhiv für Ophthalmologie*.

Sternberg, P., Davidson, P. C., Jones, D. P., Hagen, T. M., Reed, R. L., and Drews-Botsch, C. (1993). Protection of retinal pigment epithelium from oxidative injury by glutathione and precursors. *Investigative Ophthalmology & Visual Science*.

Streeten, B. W. (1969). Development of the human retinal pigment epithelium and the posterior segment. *Archives of Ophthalmology*.

Sturman, J. A., Rassin, D. K., Hayes, K. C., and Gaull, G. E. (1978). Taurine deficiency in the kitten: exchange and turnover of [35S] taurine in brain, retina, and other tissues. *The Journal of Nutrition*.

Tomi, M., Terayama, T., Isobe, T., Egami, F., Morito, A., Kurachi, M., Ohtsuki, S., Kang, Y.-S., Terasaki, T., and Hosoya, K.-i. (2007). Function and regulation of taurine transport at the inner blood-retinal barrier. *Microvascular Research*.

Wässle, H. and Boycott, B. B. (1991). Functional architecture of the mammalian retina. *Physiological Reviews*.

Weng, J., Mata, N. L., Azarian, S. M., Tzekov, R. T., Birch, D. G., and Travis, G. H. (1999). Insights into the function of Rim protein in photoreceptors and etiology of Stargardt's disease from the phenotype in abcr knockout mice. *Cell*.

Wing, G. L., Blanchard, G. C., and Weiter, J. J. (1978). The topography and age relationship of lipofuscin concentration in the retinal pigment epithelium. *Investigative Ophthalmology & Visual Science*.

Winkler, B. S., Boulton, M. E., Gottsch, J. D., and Sternberg, P. (1999). Oxidative damage and age-related macular degeneration. *Molecular Vision*.

Zarbin, M. A. (2004). Current concepts in the pathogenesis of age-related macular degeneration. *Archives of Ophthalmology*.

Zhang, H., Fan, J., Li, S., Karan, S., Rohrer, B., Palczewski, K., Frederick, J., Crouch, R., and Baehr, W. (2008). Trafficking of membrane-associated proteins to cone photoreceptor outer segments requires the chromophore 11-cis-retinal. *The Journal of Neuroscience*.